GENERALIZED FINITE ELEMENT METHOD

FOR HELMHOLTZ EQUATION

A Dissertation

by

REALINO HIDAJAT

Submitted to the Office of Graduate Studies of
Texas A&M University
in partial fulfillment of the requirements for the degree of

DOCTOR OF PHILOSOPHY

May 2007

Major Subject: Aerospace Engineering

GENERALIZED FINITE ELEMENT METHOD

FOR HELMHOLTZ EQUATION

A Dissertation

by

REALINO HIDAJAT

Submitted to the Office of Graduate Studies of
Texas A&M University
in partial fulfillment of the requirements for the degree of

DOCTOR OF PHILOSOPHY

Approved by:

Chair of Committee,	Theofanis Strouboulis
Committee Members,	John L. Junkins
	Joseph E. Pasciak
	Yalchin Efendiev
Head of Department,	Helen Reed

May 2007

Major Subject: Aerospace Engineering

ABSTRACT

Generalized Finite Element Method for Helmholtz Equation. (May 2007)

Realino Hidajat, B.S., Parahyangan Catholic University;

M.S., University of Nebraska - Lincoln

Chair of Advisory Committee: Dr. T. Strouboulis

This dissertation presents the Generalized Finite Element Method (GFEM) for the scalar Helmholtz equation, which describes the time harmonic acoustic wave propagation problem. We introduce several handbook functions for the Helmholtz equation, namely the plane-wave, wave-band, and Vekua functions, and we use these handbook functions to enrich the Finite Element space via the Partition of Unity Method to create the GFEM space. The enrichment of the approximation space by these handbook functions reduces the pollution effect due to wave number and we are able to obtain a highly accurate solution with a much smaller number of degrees-of-freedom compared with the classical Finite Element Method. The q-convergence of the handbook functions is investigated, where q is the order of the handbook function, and it is shown that asymptotically the handbook functions exhibit the same rate of exponential convergence. Hence we can conclude that the selection of the handbook functions from an admissible set should be dictated only by the ease of implementation and computational costs.

Another issue addressed in this dissertation is the error coming from the artificial truncation boundary condition, which is necessary to model the Helmholtz problem set in the unbounded domain. We observe that for high q, the most significant component of the error is the one due to the artificial truncation boundary condition. Here we propose a method to assess this error by performing an additional computation on the extended domain using GFEM with high q.

To *Saudah Safrina Sinaga* and *Amelie Indira Hidajat*

ACKNOWLEDGMENTS

First and foremost, I would like to express my sincere gratitude to Dr. Theofanis Strouboulis for his continuous guidance, support and encouragement. His passion for research and tireless effort should be a model for everyone. He taught me to never give up and to always strive for the best in spite of the situation. For this I will forever be grateful.

I would like to thank Dr. J. Junkins, Dr. J. Pasciak, and Dr. Y. Efendiev for serving on my advisory committee. Their comments and suggestions, not only during the preliminary examination and the dissertation defense but especially during my visit to their respective offices, are priceless.

I would like to express my gratitude also to Professor Ivo Babuška for his advice and encouragement during the course of this work. I am grateful to him for the invaluable discussions and sharp insights. I also thank Dr. Andrzej Safjan for introducing me to the rigorous field of computational mechanics and for patiently teaching me all the basic knowledge in this field.

I also give thanks to Dr. Kevin Copps and Dr. Lin Zhang for their support in the development of the GFEM code. They laid the foundation from which I built this work. I thank my colleagues, Dr. Dibyendu Datta, Mr. Delin Wang and Dr. Michael Newman, for their help and support. Thanks also to Dr. Helen Reed and Dr. Walter Haisler for their support and assistance, and to Ms. Karen Knabe for helping me navigate through the mountains of paperwork.

Finally, I want to thank all my family, especially my wife, daughter, parents, and sisters for their moral support.

TABLE OF CONTENTS

LIST OF TABLES

LIST OF FIGURES

FIGURE   Page

CHAPTER I

INTRODUCTION

1.1 Motivation and background

The multiple scattering problem, which is governed by the Helmholtz equation, is of great interest due to its range of applications such as analysis of sonar signature from a group of underwater objects, analysis of shear wave propagation in composites, and electromagnetic wave scattering, to name a few. In this dissertation we will focus on the scattering of acoustic waves which is governed by the scalar Helmholtz equation, and we note that the extension to the elastic wave propagation problem (vector Helmholtz equation), coupled acoustic fluid - elastic solid problems, and Maxwell equation (coupled vector Helmholtz equation) is rather straightforward, although it is evident that the associated issues of high-dimensionality are not implied to be trivial. For an excellent monogram on the Finite Element Method for the acoustic wave propagation problem we refer to Ihlenburg [1].

The analysis of the computational methods to solve the Helmholtz equation has been an intense endeavor and a lot of progress have been made in this field. Some inherent issues that are still actively investigated are:

1. **The effect of the pollution.** The pollution is defined as the difference between the approximate numerical solution and its best approximation, and it is related to the dispersion, where the numerical wave number differs from the original wave number. This pollution restricts the element size of the computational mesh which makes it necessary to use a very fine mesh for problems with large wave number. The analysis of the pollution in the context of h and hp finite element method was

---

This dissertation follows the style of Computer Methods in Applied Mechanics and Engineering.

done by Babuška and Ihlenburg [2, 3]. Deraemaeker, Babuška, and Bouillard [4] presented a general approach for assessing the pollution of various approximations of the Helmholtz equations, and Babuška and Saunter [5] addressed the important question: Is the pollution avoidable by special design of the approximation method in one and higher dimensions?

2. **The effect of the truncation of the domain.** To properly analyze the scattering problem in a finite computational domain, appropriate conditions must be applied at the truncation boundary to simulate the actual physics of the problem; namely that the scattered wave will not be reflected back to the domain. Several methods are available, such as the absorbing boundary conditions [6–9], infinite element methods [10–12], and the perfectly-matched layer [13]. The research in this field is still an ongoing endeavor with the goal of minimizing the spurious waves and reducing some geometric restrictions on the boundary.

3. **The robustness issue**. Several methods have been proposed to alleviate the pollution problem by introducing wave-like functions into the approximation methods. Example of these methods are the Partition of Unity Method of Babuška and CO-workers [14–19] and of Laghrouche, Bettess, and co-workers [20–22], Discontinuous Enrichment Method of Farhat and co-workers [23, 24], Variational Theory of Complex Rays of Ladevèze, Rouch, and Riou [25–27]. The question that have not been addressed satisfactorily by the methods above is the robustness with respect to the integration of the stiffness matrix, the round-off error, and the mesh perturbations. For example, some methods introduce special integration techniques that can work only on the rectangular domains.

Let us start by looking at the scalar Helmholtz problem in 1D (one dimensional) setting: Find $u = u(x)$, such that

$$\begin{cases} -\dfrac{d^2 u}{dx^2}(x) - k^2 u(x) = e^x, & x \in \Omega = (0,1) \\[2mm] u(0) = 0, \\[2mm] \dfrac{du}{dx}(1) - iku(1) = 0 \end{cases} \tag{1.1}$$

where k is the wave number. Here we have homogeneous Dirichlet boundary condition on the left node and the Sommerfeld radiation boundary condition on the right node. Note that for one-dimensional case, the Sommerfeld radiation boundary condition is exact; there is no spurious wave reflected from the boundary as in the higher-dimensional case. In this Model Problem we highlight in this dissertation only the capability of the GFEM in solving the Helmholtz problem with very high wave number and leave out the issue of the truncation boundary condition.

Figure 1.1 reports the H^1 seminorm of the approximate solutions $u_h(x)$ of the 1D Model Problem (1.1):

$$\frac{\sqrt{\int_0^1 |e_h'(x)|^2}}{\sqrt{\int_0^1 |u_{\mathrm{EX}}'(x)|^2}} \times 100\% \tag{1.2}$$

for various k, where $u_{\mathrm{EX}}(x)$ is the exact solution of (1.1) and $e_h(x) = u_{\mathrm{EX}}(x) - u_h(x)$ is the error in the Finite Element/GFEM solution. Here the solutions $u_h(x)$ are obtained by using the Finite Element Method with $p = 1, .., 4$ and by using the GFEM with $p = 1$ and the handbook functions:

$$\left\{ \sin\left(k(x - x_i)\right), \ \cos\left(k(x - x_i)\right) \right\} \tag{1.3}$$

where x_i is the coordinate of node i. The benefit of introducing trigonometric functions (1.3) into the approximation space is obvious from the results plotted in Figure 1.1. We
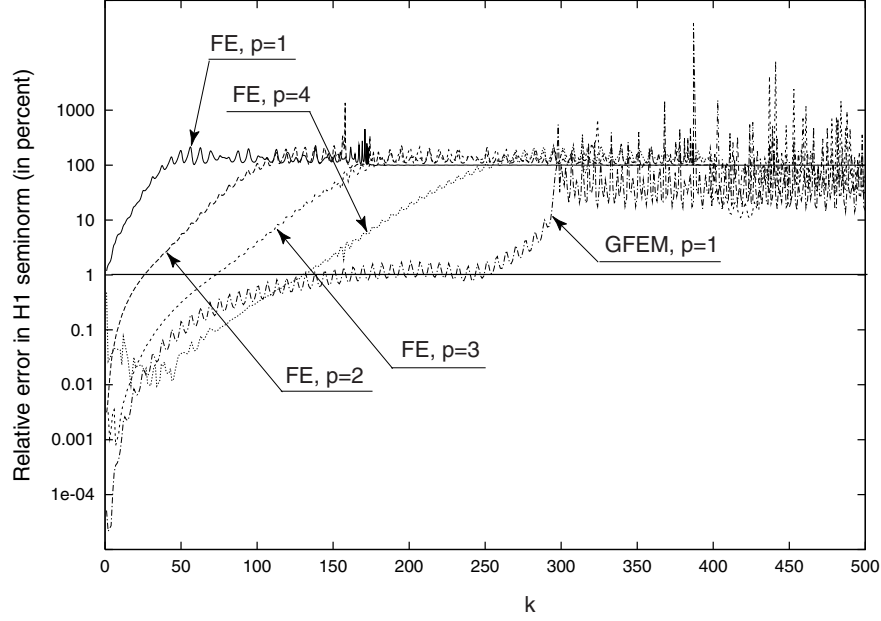
Figure 1.1. Relative error in H^1-seminorm for the solution of (1.1) using 50 uniform elements computed using Finite Element Method with $p = 1, 2, 3, 4$ and the GFEM with $p = 1$.

can see that we are able to get the solution with relative error $\approx 1\%$ up to $k \approx 250$, while the for the Finite Element Method, using $p = 4$ the same relative error can be obtained only until $k \approx 150$.

Now let us look at the pollution effect. Figures 1.2 and 1.3 show the convergence in H^1-seminorm computed using Finite Element with $p = 2$, GFEM with $p = 1$, their best approximation for $k = 50$ and $k = 100$ respectively. From both figures we can see that the pollution, which is the difference between the Finite Element/GFEM graph and its best approximation graph, disappears as the element size is reduced. Moreover, the pollution in GFEM is much less that the pollution in Finite Element for the same number of elements, and by comparing Figures 1.2 and 1.3 we can see how the pollution is worse for higher wave number k.

The idea of enriching the approximation space can be traced back to the work on the Partition of Unity Method of Babuška, Caloz, and Osborn [14], and Babuška and Melenk
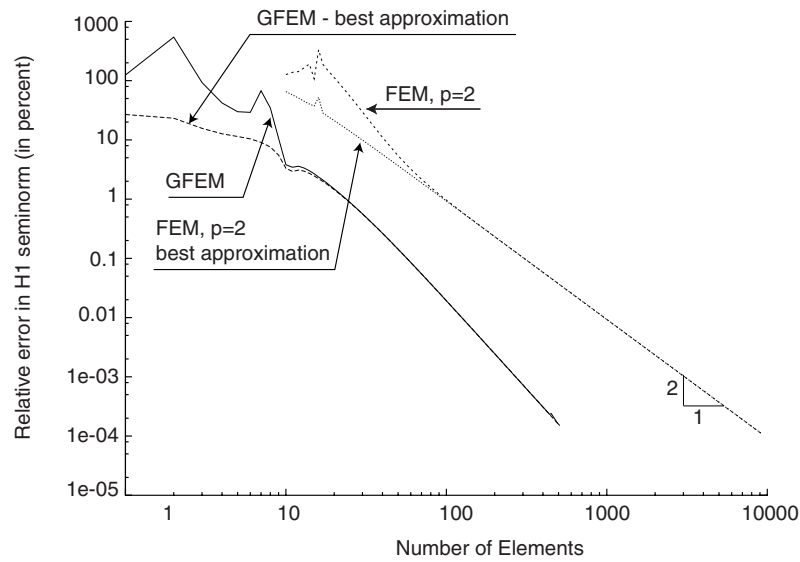
Figure 1.2. Relative error in H^1-seminorm for the solution of (1.1) versus the number of elements for $k = 50$ computed using Finite Element with $p = 2$, GFEM with $p = 1$, and their best approximation.
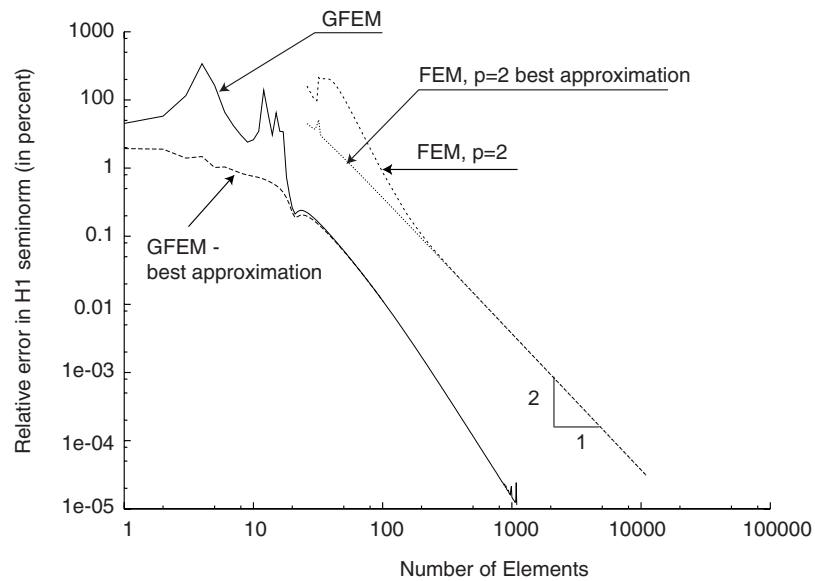
Figure 1.3. Relative error in H^1-seminorm for the solution of (1.1) versus the number of elements for $k = 100$ computed using Finite Element with $p = 2$, GFEM with $p = 1$, and their best approximation.

(see Melenk's M.Sc. and Ph.D. theses [15, 16] and in the papers stemming from these theses [17–19]). Let us also note that Oden and Duarte were the first to employ the Partition of Unity Method in a meshless setting in the context of the *hp*-cloud method [28, 29]. The Generalized Finite Element Method, which is an extension of the Partition of Unity Method, was first proposed in the works of Strouboulis, Copps, and Babuška [30–33], and also Strouboulis, Zhang, and Babuška [34–36] for solving coercive elliptic problems (e.g. the Laplace equation, the equation of heat conduction, etc) in problems with complex domains using enrichment by handbook functions. The mathematical aspects of the Generalized Finite Element Methods, including the method proposed here, were addressed in the work of Babuška, Banerjee, and Osborn [37–39] where many more references can be found. Let us also mention the work on the eXtended Finite Element Method (XFEM) by Belytschko and co-workers [40, 41] which has similar ingredients, and also the work by Duarte and co-workers [42].

The utilization of wave-related functions to enrich the approximation space for solving the Helmholtz equation was introduced in the Ph.D. thesis of Melenk [16], where the theoretical aspects of the Partition of Unity method for the Helmholtz are addressed. Other important works that utilized the plane-wave functions were contributed by Laghrouche, Bettess and co-workers [20–22], by Ortiz [43], and by Astley and Gamallo [44]. The three-dimensional version of the method was addressed by Perrey-Debain, Laghrouche, et. al. in [45]. Let us also mention the related works by Farhat and co-workers [23, 24] on the Discontinuous Enrichment Method (DEM) which also employs enrichment by plane-wave functions using a formulation based on the Discontinuous Galerkin with Lagrange Multipliers, and also the work of Ladevèze, Rouch, and Riou [25–27] on the variational theory of complex rays (VTCR) which also uses enrichments of the approximation by local solutions of the wave equation.

We note that all the proposed method that utilized wave-like solution mentioned above

are capable of reducing the pollution effect. This can be concluded from their ability to obtain accurate solution (e.g. solutions with error 1% or better in relative value of the H^1-seminorm of the error) while using meshes with mesh size h of one or several wavelengths $\lambda = 2\pi/k$. The major difference among the methods are the formulation to include the special or handbook functions and the variation of the wave solution employed. We also note that the main issue dominating all the method above is the integration of the stiffness matrix. The introduction of wave-like solution, especially the ones with high-wave number k, requires the integration of the highly-oscillatory functions for the stiffness matrices. Some semi-analytical integration methods are available, e.g. [22, 46, 47], but they impose geometrical limit on the domain of interest. The Generalized Finite Element Method, on the other hand, has an adaptive integration scheme that is more robust and is capable of doing integrations on complex domains [30, 32].

1.2 Research objectives

We can summarize the goal of this research as follows:

1. To provide a highly-accurate computational method for the Helmholtz equation with high wave number k on the domain with complex geometries. The flexibility of the Generalized Finite Element Method to include any functions into the approximation space enables us to analyze the various Helmholtz handbook functions, and we will look at their q-convergence properties.

2. To analyze the pollution and its relation with h, p, and q parameters of the Generalized Finite Element.

3. To show the robustness of the method with respect to mesh types, mesh perturbations, quadrature error and round-off error.

4. To provide the analysis of the error from the artifical truncation boundary condition, and integrating it with the analysis of interior approximation for Helmholtz equation.

5. To propose a posteriori error estimate for both the interior approximation and the error coming from artificial truncation boundary condition.

1.3   Outline of the dissertation

Following this Introduction, we will give a review of the Generalized Finite Element Method in Chapter II. Here we will also analyze the GFEM for Helmholtz equation using plane-wave functions and show its robustness with respect to mesh perturbations, quadrature error, and round-off error. We continue by presenting the wave-band functions in Chapter III and comparing its performance with the plane-wave functions in the Partition of Unity settings on the rectangular domain. For this setting, a semi-analytical integration method for the computation of the stiffness matrix is available and thus we are able to analyze the high-order Gauss Legendre integration performance used in the general GFEM setting.

In Chapter IV we will use the GFEM for the analysis of the multiple scattering problem. Here we will introduce the Vekua handbook function and compare the performance of the three handbook functions. The analysis of the error coming from the artificial truncation boundary condition will be done in Chapter V, where we will also give a method to assess that error. We will close this dissertation by giving the summary, discuss the open problems and suggest the directions of future research in Chapter VI.

CHAPTER II

GENERALIZED FINITE ELEMENT METHOD USING PLANE-WAVE HANDBOOK FUNCTION[*]

2.1 Review of the Generalized FEM

The Generalized Finite Element Method (GFEM) is a direct extension of the standard finite element method, which makes it possible to get accurate solution of the problems defined in complex domains. The GFEM is based on the Partition of Unity Method (PUM) which was developed by Babuška and Melenk [15–18] and Duarte and Oden [48]. The design and implementation of GFEM was studied by Strouboulis, Copps, and Babuška [30–32]. For the history of GFEM aspects, such as PUM, adaptive integration, etc, see the references in [31].

Definition 1 (Partition of Unity)

Let $d \in \mathbb{N}$, $\Omega \subset \mathbb{R}^d$ be an open set, $\{\Omega_i^h\}_{i=1}^{N(h)}$, $h > 0$, be a family of coverings of Ω satisfying an overlapping condition:

$$\exists M \in \mathbb{N}, \quad \forall h > 0, \quad \forall x \in \Omega, \quad \text{card}\{i | x \in \Omega_i^h\} \leq M. \tag{2.1}$$

Let $\{\phi_i^h\}_{i=1}^{N(h)} \subset W^{1,\infty}(\mathbb{R}^d)$ be a family of partitions of unity subordinate to the coverings $\{\Omega_i^h\}_{i=1}^{N(h)}$ satisfying

$$\text{supp}\phi_i^h \subset \text{closure}(\Omega_i^h); \qquad \sum_{i=1}^{N(h)} \phi_i^h \equiv 1, \text{on} \quad \Omega, \tag{2.2}$$

$$\|\phi_i^h\|_{L^\infty(\Omega)} \leq C_\infty; \qquad \|\nabla \phi_i^h\|_{L^\infty(\Omega)} \leq \frac{C_G}{\text{diam}(\Omega_i^h)}, \tag{2.3}$$

---

[*]This chapter is reprinted with permission from "The generalized finite element method for Helmholtz equation: Theory, computation, and open problems" by T. Strouboulis, I. Babuška and R. Hidajat, Comp. Meth. Appl. Mech. Engrg. 195 (2006) 4711-4731 © 2006 Elsevier B.V.

for some C_∞, $C_G > 0$ independent of h.

Let $V_i^{h,p} \subset H^1(\Omega \bigcap \Omega_i^h)$ be a two parameter family of functions spaces, and define $V^{h,p}$

as

$$V^{h,p} = \left\{ v = \sum_{i=1}^{N(h)} \phi_i^h v_i^{h,p} \Big| v_i^{h,p} \in V_i^{h,p} \right\} \subset H^1(\Omega). \tag{2.4}$$

Then we have:

Theorem 1 (Approximation property of the Partition of Unity)

Let Ω, $\{\Omega_i^h\}$, $\{\phi_i^h\}$, and $\{V_i^{h,p}\}$ be given as above. Let $u \in H^k(\Omega)$, $k \leq 1$, and suppose

that for fixed h, p, the function u can be approximated locally by functions in $V_i^{h,p}$, i.e., for

each i, there is $v_i^{h,p} \in V_i^{h,p}$ such that

$$\|u - v_i^{h,p}\|_{L^2(\Omega \bigcap \Omega_i^h)} \leq \epsilon_1(i,h,p)\|u\|_{H^k(\Omega \bigcap \Omega_i^h)}, \tag{2.5}$$

$$\|\nabla(u - v_i^{h,p})\|_{L^2(\Omega \bigcap \Omega_i^h)} \leq \epsilon_2(i,h,p)\|u\|_{H^k(\Omega \bigcap \Omega_i^h)}. \tag{2.6}$$

Then there is $v^{h,p} \in V^{h,p}$ such that

$$\|u - v^{h,p}\|_{L^2(\Omega)} \leq M C_\infty \max_{i=1,\ldots,N(h)} \epsilon_1(i,h,p)\|u\|_{H^k(\Omega)}, \tag{2.7}$$

$$\|\nabla(u - v^{h,p})\|_{L^2(\Omega)} \leq \sqrt{2}M \max_i \left(C_G \frac{\epsilon_1(i,h,p)}{\text{diam}(\Omega \bigcap \Omega_i^h)} + C_\infty \epsilon_2(i,h,p) \right) \|u\|_{H^k(\Omega)}. \tag{2.8}$$

where C_∞, C_G are the constants in Definition 1.

The Partition of Unity of Babuška and Melenk seeks the solution of the following discrete

problem:

Find $u_{\text{PUM}} \in S_h^q$ such that:

$$\mathcal{B}(u_{\text{PUM}}, v) = \mathcal{L}(v) \qquad \forall\, v \in S_h^q \tag{2.9}$$

where $\mathcal{B}(\cdot,\cdot),\mathcal{L}(\cdot)$ are the bilinear and linear forms obtained from the standard variational formulation, and S_h^q is the Partition of Unity space determined by the mesh Δ_h, and the degree q of the special or handbook functions employed at each mesh vertex, namely:

$$S_h^q = \left\{ v \middle| v = \sum_{i=1}^{\text{nnodes}} \phi_i^h \left(\sum_{j=1}^{q} a_j^{(i)} W_j^{(i)} \right) \right\} \tag{2.10}$$

Here $\{\phi_i^h\}_{i=1}^{\text{nnodes}}$ is the Partition of Unity functions, and $\left\{ W_j^{(i)} \right\}_{j=1}^{q}$ are the *special* or *handbook* function employed in the i-th vertex, and we define:

$$V_i^{h,p} = \left\{ v_i^{h,p} \middle| v_i^{h,p} = \sum_{j=1}^{q} a_j^{(i)} W_j^{(i)} \right\} \tag{2.11}$$

as the local approximation space.

This idea is extended to the Generalized Finite Element Method, where the approximation space consists of the Finite Element space and the Partition of Unity space described above. Here the discrete problem is:

Find $u_{\text{GFEM}} \in S_{h,p}^q$ such that:

$$\mathcal{B}(u_{\text{GFEM}}, v) = \mathcal{L}(v) \qquad \forall\ v \in S_{h,p}^q \tag{2.12}$$

where $S_{h,p}^q$ is the Generalized Finite Element space determined by the mesh Δ_h, the degree p of the finite element basis on Δ_h, and the degree q of the special or handbook functions employed at each mesh vertex, namely:

$$S_{h,p}^{k,q} = \left\{ v \middle| v = \sum_{k=1}^{\text{nfem}} b_k N_k + \sum_{i=1}^{\text{nnodes}} \phi_i^h \left(\sum_{j=1}^{q} a_j^{(i)} W_j^{(i)} \right) \right\} \tag{2.13}$$

where N_k denote the standard finite element basis function defined over the mesh Δ_h.

2.2 Generalized FEM formulation for Helmholtz equation

In this section we outline the basic results for the Helmholtz problem with Robin boundary conditions in a finite domain. For more details and proofs the reader should consult Chapter 8 in the Ph.D. dissertation of Melenk [16].
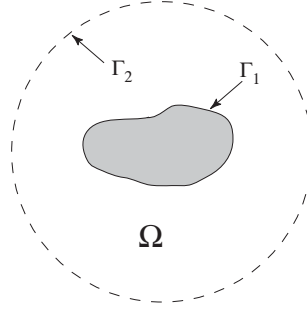
Figure 2.1. Example of a domain Ω with interior boundary Γ_1, and outer boundary Γ_2.

Definition 2 (Helmholtz model problem)

Let $\Omega \subset \mathbb{R}^2$, be a bounded domain, with boundary $\partial\Omega = \Gamma_1 \cup \Gamma_2$, $\Gamma_1 \cap \Gamma_2 = \emptyset$, as shown in Figure 2.1. We will be interested in the solution u, of the boundary-value problem:

$$-\Delta u - k^2 u = f \qquad \text{in } \Omega \tag{2.14a}$$

$$\frac{\partial u}{\partial n} = g_1 \qquad \text{on } \Gamma_1 \tag{2.14b}$$

$$\frac{\partial u}{\partial n} - iku = g_2 \qquad \text{on } \Gamma_2 \tag{2.14c}$$

Although all the facts mentioned below hold also for $\Omega \subset \mathbb{R}^n$, for simplicity and practical issues related with the numerical implementations we are focusing on the two dimensional case, $\Omega \subset \mathbb{R}^2$.

Definition 3 (Weak formulation of Helmholtz problem)

Find $u \in H^1(\Omega)$ such that:

$$\mathcal{B}(u, v) = \mathcal{L}(v) \qquad \forall\, v \in H^1(\Omega) \tag{2.15a}$$

where:

$$\mathcal{B}(u, v) = \int_\Omega \nabla u \nabla \bar{v}\, d\Omega - k^2 \int_\Omega u\, \bar{v}\, d\Omega + ik \oint_{\Gamma_2} u\, \bar{v}\, ds \tag{2.15b}$$

$$\mathcal{L}(v) = \int_\Omega f \, \bar{v} \, d\Omega + \sum_{i=1}^{2} \oint_{\Gamma_i} g_i \, \bar{v} \, ds, \qquad (2.15c)$$

where $H^1(\Omega)$ is the space of functions with square-integrable derivatives over Ω.

Let:

$$|||u||| \stackrel{\text{def}}{=} \sqrt{\|\nabla u\|_{L^2(\Omega)}^2 + k^2 \|u\|_{L^2(\Omega)}^2} \qquad (2.16)$$

We have:

Theorem 2 (Existence and Uniqueness)

Let $f \in H^{-1}(\Omega)$, $g_i \in H^{-1/2}(\Gamma_i)$, $i = 1, 2$. Then, there exists a unique solution of the Helmholtz problem which satisfies:

$$|||u||| \leq \mathcal{C}(\Omega, k) \left(\|f\|_{H^{-1}(\Omega)} + \sum_{i=1}^{2} \|g_i\|_{H^{-1/2}(\Gamma_i)} \right) \qquad (2.17)$$

Here $\mathcal{C}(\Omega, k)$ indicates the dependence of $\mathcal{C}$ on the domain Ω and the wave-number k.

Proof. It is sufficient to consider the case with $\Gamma_1 = \emptyset$. Uniqueness (resp. existence) follows if we can show that:

$$\int_\Omega \nabla u \cdot \nabla \bar{v} \, d\Omega - k^2 \int_\Omega u \, \bar{v} \, d\Omega \pm ik \oint_{\Gamma_2} u \, \bar{v} \, d\Gamma = 0 \qquad (2.18)$$

with plus (resp. minus) sign in front of the boundary term implies that $u = 0$. Choosing $v = u$ and considering the imaginary part it follows that $u = 0$ on Γ_2. Thus, $u \in H_0^1(\Omega)$, and we have

$$\int_\Omega \nabla u \cdot \nabla \bar{v} \, d\Omega - k^2 \int_\Omega u \, \bar{v} \, d\Omega = 0 \qquad \forall \, v \in H^1(\Omega) \qquad (2.19)$$

which means that u satisfies the Helmholtz equation with $f = 0$, and homogeneous boundary conditions on $\partial\Omega$, from which it follows (see p. 117 in Melenk [16]) that u is identically equal to zero. For the proof of (2.17) see pp. 118-121 in Melenk [16]. $\square$

Remark 1: In the case that Ω is convex, $\mathcal{C}$ does not depend on k.

In what follows we will assume that Ω is an annulus and we will let $f = 0$.

Let Δ_h be a uniform mesh of squares of size h covering the domain Ω, as is, e.g., shown in Figure 2.2(a). Let $\phi_i^{\Delta_h}, i = 1, ..., \text{nnodes}$, be the classical piecewise bilinear "hat" functions associated with the nodes located at the vertices of the squares, and let

$$\omega_i^{\Delta_h} \overset{\text{def}}{=} \text{supp } \phi_i^{\Delta_h} = \left\{ x \in \Omega \mid \phi_i^{\Delta_h}(x) > 0 \right\} \tag{2.20}$$

be the support of $\phi_i^{\Delta_h}$ which consists of the four squares which share the node. Then $\{\phi_i^{\Delta_h}\}_{i=1}^{\text{nnodes}}$ is a Lipschitz partition of unity subordinate to the cover $\{\omega_i^{\Delta_h}\}_{i=1}^{\text{nnodes}}$ satisfying:

$$\sum_{i=i}^{\text{nnodes}} \phi_i^{\Delta_h} \equiv 1 \text{ on } \Omega, \qquad \|\phi_i^{\Delta_h}\|_{L^\infty(\mathbb{R}^2)} \leq 1, \qquad \|\nabla\phi_i^{\Delta_h}\|_{L^\infty(\mathbb{R}^2)} \leq \frac{C}{h} \tag{2.21}$$
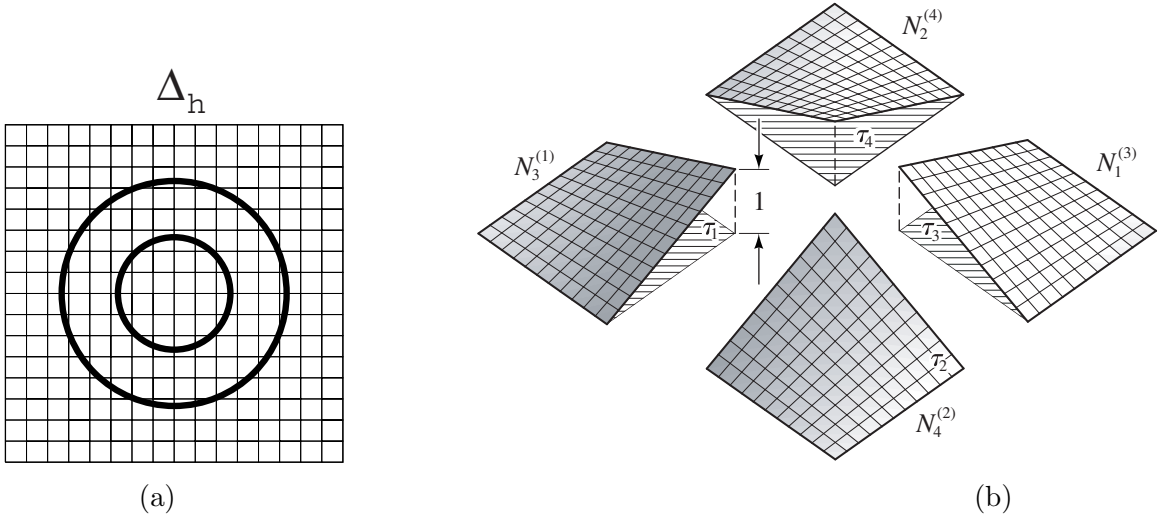
Figure 2.2. (a) Example of a Cartesian mesh Δ_h used in the formulation of the Generalized Finite Element Method over an annular domain Ω. (b) A typical exploded view of the hat function $\phi_i^{\Delta h}$ over its support.

We will construct the space of Generalized Finite Element solutions by combining the following discrete spaces of functions on the mesh Δ_h:

a) The standard bi-p (tensor product) finite element space:

$$S^p_{\Delta_h} = \left\{ v \in C^0(\Omega) \;\middle|\; v|_\tau \bullet \mathbf{F}_\tau \in \tilde{Q}^p \right\} \tag{2.22}$$

where $\tilde{Q}^p$ is the space of bi-p (tensor product) polynomial functions of degree p defined over $\hat{\tau}$ (see p. 97 in Szabó and Babuška [49]), and $\mathbf{F}_\tau : \hat{\tau} = (-1, 1)^2 \longmapsto 1$, is the affine transformation

$$x = \mathbf{F}_\tau(\hat{x}) = x^\tau_{\text{mid}} + \frac{h}{2}\hat{x} \tag{2.23}$$

mapping $\hat{\tau} = (-1, 1)^2$ into the square τ of size h, centered at x^τ_{mid}.

b) The partition of unity space:

$$W^{k;q}_{\Delta_h} = \left\{ v = \sum_{i=1}^{\text{nnodes}} \phi_i^{\Delta_h}\, v_i \;\middle|\; v_i \in W^{k;q}_{\text{loc}}(\omega_i^{\Delta_h}) \right\} \tag{2.24}$$

where

$$W^{k;q}_{\text{loc}} = \text{span}\left\{ w_k = \exp\left(ik\left(x\cos\frac{2\pi n}{q} + y\sin\frac{2\pi n}{q} \right) \right), n = 0, ..., q-1 \right\} \tag{2.25}$$

is the local space of linear combinations of plane waves traveling in the directions $\left(\cos\frac{2\pi n}{q}, \sin\frac{2\pi n}{q} \right)$, $n = 0, ..., q-1$. Figure 2.3 depicts the employed wave directions for $q = 1, 3, 5, 7, 9$, and 11, in a typical patch $\omega_i^{\Delta h}$.

Definition 4 (Generalized Finite Element solution)

Find

$$u^{p,q}_h = \sum_{k=1}^{\text{nfem}} b_k N_k + \sum_{i=1}^{\text{nnodes}} \phi_i^{\Delta h} \left(\sum_{j=1}^{q} a_j^{(i)} W_j^{(i)} \right) \in S^{k;q}_{h,p} \tag{2.26}$$
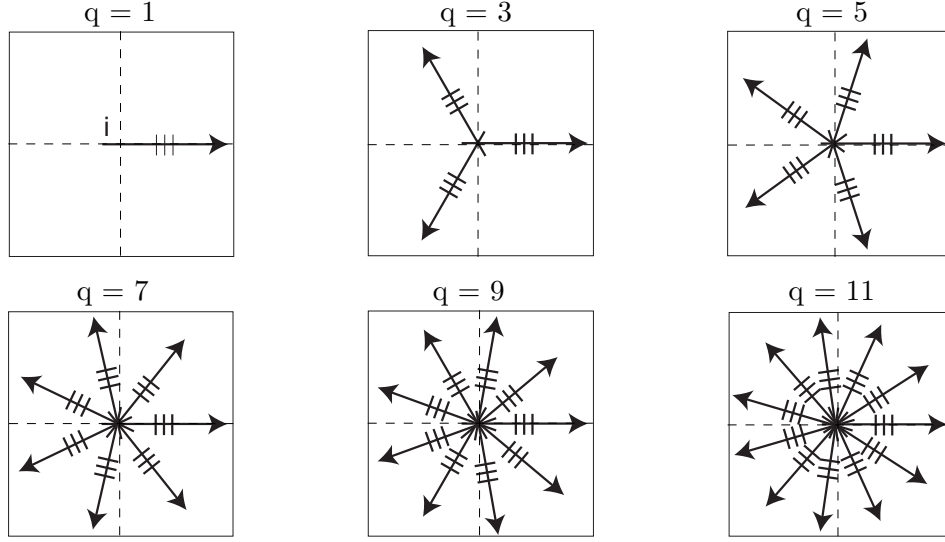
Figure 2.3. Examples of the employed wave directions in a typical patch $\omega_i^{\Delta h}$.

such that

$$\mathcal{B}(u_h^{p,q}, v) = \mathcal{L}(v) \quad \forall v \in S_{h,p}^{k;q} \tag{2.27}$$

where N_k denotes a standard FE bi-p basis functions on Δ_h, nfem is the total number of degrees of freedom for the bi-p FE basis functions, and $W_j^{(i)}, j = 1, ..., q$ are the employed plane-wave functions in the patch $\omega_i^{\Delta h}$.

The stability and quasi-optimality of the Generalized FEM is established from the following results which were formulated and proven in Melenk [16].

Theorem 3 (Stability and Quasi-optimality)

Let Ω be a star-shaped domain with smooth boundary, and let S be discrete approximation spaces satisfying

$$\inf_{\chi \in S} \left(||v - \chi||_{L^2(\Omega)} + h||\nabla(v - \chi)||_{L^2(\Omega)} \right) \leq \mathcal{C}(\Omega) \, h^2 \left(|v|_{H^2(\Omega)} + (1+k)|||v||| \right) \tag{2.28}$$

for all $v \in H^2(\Omega)$, with $\mathcal{C}$ independent of v and h. Then there exist $\mathcal{C}_1, \mathcal{C}_2, \mathcal{C}_3 > 0$, depending only on Ω, such that under the assumption:

$$(1 + k^2)h < \mathcal{C}_1 \tag{2.29}$$

we have

$$\inf_{u \in S} \sup_{v \in S} \frac{\Re \mathcal{B}(u,v)}{|||u||| \; |||v|||} \geq \frac{\mathcal{C}_2}{1+k} \tag{2.30}$$

and

$$|||u - u_h^{p,q}||| \leq \mathcal{C}_3 \inf_{\chi \in S} |||u - \chi||| \tag{2.31}$$

Proof. See pp. 122-123 in Melenk [16]. □

We also have:

Lemma 1 (Approximation Property of Generalized FEM space)

The Generalized Finite Element Space

$$S_{h,p}^{k;q} \stackrel{\text{def}}{=} S_{\Delta_h}^p \oplus W_{\Delta_h}^{k;q} \tag{2.32}$$

satisfies (2.28).

Proof. The proof follows from p. 138 in Melenk [16]. □

It follows that Theorem 3 is applicable in the Generalized FEM.

Remark 2: At present, we cannot say a-priori what is sufficiently small h, and what is the value of $\mathcal{C}_3$.

Remark 3: The constant $\mathcal{C}_3$ in (2.31) is related to the pollution due to the wave number, which is directly related to the numerical dispersion. The main effect is that the wave number of the Galerkin solution is different from the wave number of the exact solution. The pollution in the solution $u_h^{p,q}$ of the Helmholtz equation can be measured by dividing its error $|||u - u_h^{p,q}|||$ by the corresponding error in the best approximation $\inf_{\chi \in S_{h,p}^{k;q}} |||u - \chi|||$. The deviation of this ratio from one measures the pollution with respect to the $||| \cdot |||$ norm.

Similarly, the pollution can be measured in other norms, e.g. the $\| \cdot \|_{L^2}$ norm, etc., and also in any output $\mathcal{F}(u)$ of interest.

Remark 4: In the one-dimensional case and for finite element approximation using polynomial shape functions of degree p, Babuška and Ihlenburg [50, 51] have proven that

$$\frac{||\nabla(u - u_h^{p,0})||_{L^2(\Omega)}}{\inf\limits_{\chi \in S_{h,p}} ||\nabla(u - \chi)||_{L^2(\Omega)}} \approx \mathcal{C}_1 + \mathcal{C}_2 k \left(\frac{kh}{p} \right)^p \tag{2.33}$$

where we let $S_{h,p} = S_{h,p}^{k;0}$. The term $\mathcal{C}_2 k \left(\frac{kh}{p} \right)^p$ reflects the pollution due to the wave number. To understand its effect let

$$h = \frac{p}{k} \left(\frac{\text{tol}}{\mathcal{C}_1} \right)^{\frac{1}{p}} \tag{2.34}$$

where tol is a desired error tolerance. Then for the error in the best approximation we have

$$\inf\limits_{\chi \in S_{h,p}} ||\nabla(u - \chi)||_{L^2(\Omega)} \approx \text{tol} \tag{2.35}$$

for any k, while for the same choices of h and p, for the error in the Galerkin solution to the Helmholtz problem $u_h^{p,0}$, we have

$$||\nabla(u - u_h^{p,0})||_{L^2(\Omega)} \approx \text{tol} \left(1 + \frac{\mathcal{C}_2}{\mathcal{C}_1} k \right) \tag{2.36}$$

which diverges to infinity linearly with k.

Equation (2.31) relates the error in the Generalized FEM, $|||u - u_h^{p,q}|||$, with the error in the best approximation $\inf\limits_{\chi \in S_{h,p}^{k;q}} |||u - \chi|||$. Various statements can be made about the convergence of the error in best approximation depending on the regularity of the solution.

In this paper we will address only the case of analytic solutions for which we have:

Theorem 4 (h and p and q convergence)

Let the solution u of the Helmholtz problem (2.15) be analytic on $\bar{\Omega} = \Omega \cup \partial\Omega$. Then,

    1. For fixed h we have:

$$\inf_{\chi \in S_{h,p}^{k;q}} |||u - \chi||| \leq \mathcal{C}(h) \; e^{-(\alpha q + \beta p)} \tag{2.37}$$

    where α, β also depend on h.

    2. For fixed p and q we have:

$$\inf_{\chi \in S_{h,p}^{k;q}} |||u - \chi||| \leq \mathcal{C}(p,q) \; h^{-p} \tag{2.38}$$

The main results needed for the proof are given in sections 8.4.-8.6. of Melenk [16].

Remark 5: When $(1 + k^2)h$ is sufficiently small, Theorem 4 also characterizes $|||u - u_h^{p,q}|||$, the error in the Generalized FEM solution $u_h^{p,q}$. When this assumption does not hold, the error in $u_h^{p,q}$ can be rather large, e.g. the relative error $|||u - u_h^{p,q}|||/|||u|||$, can be 100% or larger.

Remark 6: Following a similar approach as in [4, 5], it is also possible to characterize the dependence of the pollution on p and q in a similar form as in (2.33).

The aim of the computation is to obtain reliable information for outputs of interest. For example, we may be interested in small error measured in the H^1-seminorm $\|\nabla(u - u_h^{p,q})\|_{L^2(\Omega)}$, or in small error in the pressure at a point $|u(\bar{x}) - u_h^{p,q}(\bar{x})|$, the value of an integral of the pressure, or in general $\mathcal{F}(u) - \mathcal{F}(u_{\Delta h}^{p,q})$, where $\mathcal{F}$ is an output functional.

The implementation consists of the following stages:

1. Forming the discrete GFEM (Generalized FEM) equations:

$$\mathbf{KU} = \mathbf{F} \qquad (2.39)$$

In practice, the coefficients in $\mathbf{K}$ and $\mathbf{F}$ are replaced by approximate values evaluated by numerical quadrature, and hence we must address the effect of the error in the numerical integrations. More precisely, let $u_{h,*}^{p,q}$ be the discrete GFEM solution obtained using the perturbed system $\mathbf{K}^*\mathbf{U}^* = \mathbf{F}^*$, where $\mathbf{K}^*, \mathbf{F}^*$ are, respectively, the perturbed stiffness matrix and load vector obtained using numerical quadrature. Then, using the triangle inequality we have:

$$\left| |||u - u_h^{p,q}||| - |||u_h^{p,q} - u_{h,*}^{p,q}||| \right| \leq |||u - u_{h,*}^{p,q}||| \leq |||u - u_h^{p,q}||| + |||u_h^{p,q} - u_{h,*}^{p,q}||| \quad (2.40)$$

The term $|||u_h^{p,q} - u_{h,*}^{p,q}|||$ measures the effect of the numerical integration errors, and can affect the convergence of the method.

2. Solving the discrete GFEM equations by a linear equation solver. We employ Gauss elimination with partial pivoting, and hence we must also address the effect of the roundoff error.

3. A posteriori analysis of the error in an output $\mathcal{F}(u_h^{p,q})$. Here we will use a rather straightforward extrapolation approach to estimate the error in any output of interest, by employing:

$$\frac{\mathcal{F}(u) - \mathcal{F}(u_h^{p,q})}{\mathcal{F}(u)} \approx \frac{\mathcal{F}(u_h^{p,q+s}) - \mathcal{F}(u_h^{p,q})}{\mathcal{F}(u_h^{p,q+s})} \qquad (2.41)$$

Using sufficiently high s we can obtain a reliable estimator for any computed output $\mathcal{F}(u_h^{p,q})$.

2.3 *p*- and *q*-convergence of the Generalized FEM using plane-wave basis functions

In what follows we will present and analyze the computational GFEM results obtained by solving the problem of a scattering of a plane wave by a rigid circular cylinder, which is depicted in Figure 2.4, using the (h, p, q)-version of the Generalized FEM. Employing cylindrical coordinates (r, θ), the boundary value problem for the scattered pressure $u(r, \theta)$ reads:

$$\nabla^2 u + k^2 u = 0, \qquad r > a \tag{2.42a}$$

$$\frac{\partial u}{\partial r} = -\frac{\partial}{\partial r}(u_{\text{inc}}), \qquad r = a \tag{2.42b}$$

$$\lim_{r \to \infty} \sqrt{r} \left(\frac{\partial u}{\partial r} - iku \right) = 0 \tag{2.42c}$$

where:

$$u_{\text{inc}}(r, \theta) = P_0 \, e^{ikr \cos \theta} \tag{2.43}$$

is the pressure field for the incident plane wave. Using separation of variables (see, e.g., p. 412 in Jones [52]) we obtain the scattered field in the form:

$$u(r, \theta) = -P_0 \sum_{n=0}^{\infty} \epsilon_n i^n \frac{J'_n(ka) H_n(kr)}{H'_n(ka)} \cos(n\theta) \tag{2.44}$$

where $\epsilon_0 = 1, \epsilon_n = 2, n \neq 0$, $H_n(z)$ is the cylindrical Hankel function of the first kind, and $J_n(z)$ is the cylindrical Bessel function of the first kind. Using

$$g_1 = -\frac{\partial}{\partial n}(u_{\text{inc}}) \qquad \text{on } \Gamma_1 = \Gamma_s \tag{2.45}$$

in the Neumann boundary condition (2.14b), and

$$g_2 = \frac{\partial u}{\partial n} - iku \qquad \text{on } \Gamma_2 \tag{2.46}$$

in Robin boundary condition (2.14c), we have completed the definition of our model example

in the finite annular domain Ω bounded by Γ_1 and Γ_2.
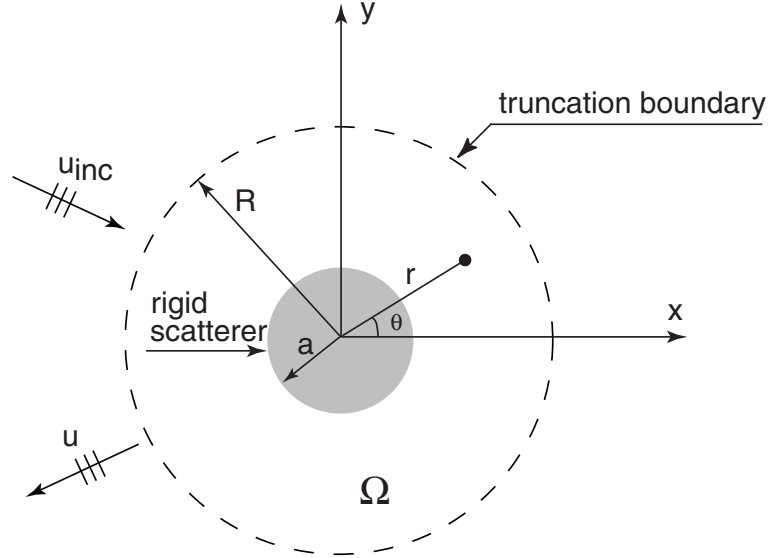
Figure 2.4. Notations used in the definition of the model example of scattering of a plane wave by a rigid circular scatterer.

In our computations we employed the following data:

- Radius of scatterer, $a = 1$

- Amplitude of incident wave, $P_0 = 1$

- Radius of truncation boundary $R = 2$

- Wave number, $k = 20$.

and we plot the countours of the real and imaginary parts of the scattered field using the

data above on Figure 2.5.

In all the computations below the convergence of the Generalized FEM solution $u_h^{p,q}$,

will be obtained by increasing p and q on the Cartesian meshes shown in Figure 2.6.

In all the results below, unless explicitly stated, the error due to evaluation of $\mathbf{K}$ and

$\mathbf{F}$ by numerical integration is negligible. Here we employed the 40×40 Gauss-Legendre

REAL PART OF THE SCATTERED WAVE
Min = -.117E+01 ; Max = 0.117E+01

-0.75 -0.50 -0.25   0.00   0.25   0.50   0.75

IMAGINARY PART OF THE SCATTERED WAVE
Min = -.115E+01 ; Max = 0.115E+01

-0.75 -0.50 -0.25   0.00   0.25   0.50   0.75
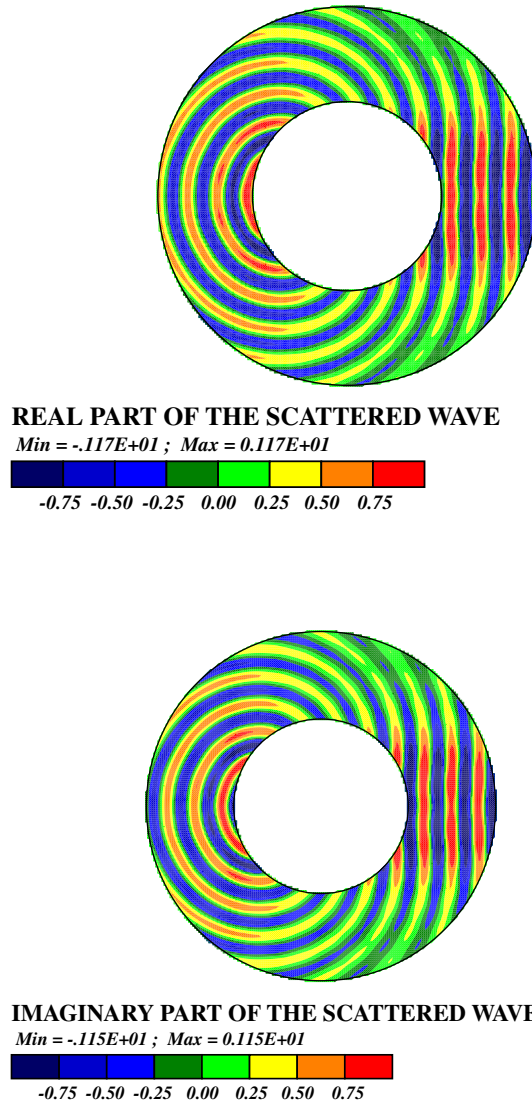
Figure 2.5. Contours of the real and imaginary parts of the scattered field of the rigid scattering model example for $k = 20$.

integration rule in the squares not intersecting the boundary, while in the squares which intersect the boundary we employed the 13 × 13 Gauss-Legendre rule in the subelements obtained after subdividing the elements uniformly 9 times and using blending function transformation in the subelements adjacent to the boundary. To compute the load vector and stiffness matrix contributions of the boundary terms we used, piecewise, the 40 point Gauss-Legendre integration rule. These choices practically eliminate the numerical
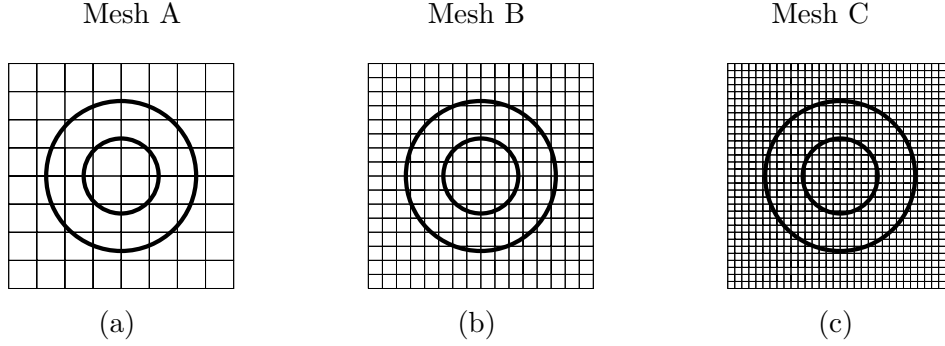
Figure 2.6. The Cartesian meshes used in the computations: (a) Mesh A, $h = 0.75$ (b) Mesh B, $h = 0.375$ (c) Mesh C, $h = 0.1875$.

integration error for $ka = 20$, and for the range of accuracy sought in the computations.

Table 2.1. The values of the percent relative error in the GFEM solution: $\|\nabla(u - u_h^{p,0})\|_{L^2(\Omega)}/$ $\|\nabla u\|_{L^2(\Omega)} \times 100\%$ (first line), the best approximation: $\|\nabla(u - \mathcal{A}_h^{p,q,*}u)\|_{L^2(\Omega)}/\|\nabla u\|_{L^2(\Omega)} \times 100\%$ (second line), and their ratio $\|\nabla(u - u_h^{p,0})\|_{L^2(\Omega)}/\|\nabla(u - \mathcal{A}_h^{p,q,*}u)\|_{L^2(\Omega)}$ (third line in parenthesis).

	$p = 1$	$p = 2$	$p = 3$	$p = 4$	$p = 5$
Mesh A	99.9008	101.8291	128.9875	117.2884	103.2724
$h = 0.75$	99.1295	96.8871	89.3488	74.9621	56.8233
	(1.0078)	(1.0510)	(1.4437)	(1.5647)	(1.8174)
Mesh B	127.2886	160.2546	120.5563	46.4416	12.6999
$h = 0.375$	96.2143	83.4217	54.4879	27.0861	10.6751
	(1.3230)	(1.9210)	(2.2126)	(1.7146)	(1.1897)
Mesh C	185.3955	109.1867	14.8250	2.7381	0.5046
$h = 0.1875$	81.0208	36.7081	11.4461	2.6833	0.5047
	(2.2883)	(2.9746)	(1.2952)	(1.0204)	(0.9980)

In Table 2.1 we report the percent relative error $\|\nabla(u - u_h^{p,0})\|_{L^2(\Omega)}/\|\nabla u\|_{L^2(\Omega)} \times 100\%$, the corresponding percent relative error in the best approximation $\|\nabla(u - \mathcal{A}_h^{p,q,*}u)\|_{L^2(\Omega)}/$ $\|\nabla u\|_{L^2(\Omega)} \times 100\%$, where $\mathcal{A}_h^{p,q,*}u$ denotes the best approximation of u which was computed using numerical integration and is defined below, and the value of their ratio $\|\nabla(u - u_h^{p,0})\|_{L^2(\Omega)}/\|\nabla(u - \mathcal{A}_h^{p,q,*}u)\|_{L^2(\Omega)}$ which measures the pollution, for Mesh A, B, and C, and for $p = 1, ..., 5$. We will say that the pollution in the H^1-seminorm of the error is negligible

if:

$$\frac{\|\nabla(u - u_h^{p,0})\|_{L^2(\Omega)}}{\|\nabla(u - \mathcal{A}_h^{p,q,*}u)\|_{L^2(\Omega)}} - 1 < \epsilon \tag{2.47}$$

for sufficiently small $\epsilon > 0$. In the results below we see that when the error is small, the ratio $\|\nabla(u - u_h^p)\|_{L^2(\Omega)}/\|\nabla(u - \mathcal{A}_h^{p,q,*}u)\|_{L^2(\Omega)}$ may be below one. This is due to the errors in the employed numerical integrations of the right-hand side of the discrete problem for $\mathcal{A}_h^{p,q,*}u$, and this only happens for rather small error and when the pollution is negligible.

Remark 7: Let us also note that for rectangular elements it is also possible to evaluate all integrals analytically following Bettess et. al [22, 46]. Nevertheless this may not be the case for elements intersecting the boundary where we need to employ numerical integration.

Let us now elaborate on the computation of the best approximation $\mathcal{A}_h^{p,q,*}u$. Let $\mathcal{A}_h^{p,q}u$ be the best approximation of u in the H^1-seminorm defined by the discrete variational problem:

Definition 5 (Best Approximation)

Find $\mathcal{A}_h^{p,q}u \in S_{h,p}^{k;q}$ such that:

$$\int_\Omega \nabla\left(\mathcal{A}_h^{p,q}u\right) \cdot \nabla\bar{v} \, d\Omega = \int_\Omega \nabla u \cdot \nabla\bar{v} \, d\Omega \qquad \forall \, v \in S_{h,p}^{k;q} \tag{2.48}$$

where u is given by (2.44).

This leads to the system of linear equations

$$\mathbf{K}^{\mathrm{BA}} \, \mathbf{U}^{\mathrm{BA}} = \mathbf{F}^{\mathrm{BA}} \tag{2.49}$$

where $\mathbf{K}^{\mathrm{BA}}$ consists of the Laplacian part of $\mathbf{K}$ used in the discrete system of Helmholtz GFEM equations. The right hand side $\mathbf{F}^{\mathrm{BA}}$ is not computed when setting up the discrete Helmholtz GFEM equations, and its evaluation requires the numerical integration of integrals of the type

$$\int_\Omega \nabla u \cdot \nabla N_k \, d\Omega, \qquad \int_\Omega \nabla u \cdot \nabla\left(\phi_i^{\Delta_h} W_j^{(i)}\right) \, d\Omega \tag{2.50}$$

respectively, for the FE degrees of freedom, and the plane-wave degrees of freedom in each patch $\omega_i^{\Delta h}$. These numerical integration errors for the employed numerical quadrature in the evaluation of these terms are not negligible and are responsible for the paradoxical behavior of the H^1-seminorm of the error in the Helmholtz GFEM solution $u_h^{p,q}$ being smaller that the corresponding value of the H^1-seminorm of the error in the best approximation $\mathcal{A}_h^{p,q,*}u$, when the relative error is very small, when $u_h^{p,q}$ and $\mathcal{A}_h^{p,q}u$ should be practically identical. For this reason we employed the star in $\mathcal{A}_h^{p,q,*}u$ to underline the effect of numerical integration.

In Theorem 3 above we have stated that for sufficiently small $(1 + k^2)h$, the Helmholtz GFEM solution $u_h^{p,q}$ converges like the best approximation $\mathcal{A}_h^{p,q}u$, namely there exists a $\mathcal{C}$ such that

$$\|\nabla(u - u_h^{p,q})\|_{L^2(\Omega)} \leq \mathcal{C}\|\nabla(u - \mathcal{A}_h^{p,q}u)\|_{L^2(\Omega)} \tag{2.51}$$

Nevertheless, the present theory does not indicate what is sufficiently small $(1 + k^2)h$. We will now give some results which indicate when $(1 + k^2)h$ is sufficiently small in the setting of our model example.

In Table 2.1 we give the values of the percent relative error in the GFEM solution: $\|\nabla(u - u_h^{p,0})\|_{L^2(\Omega)}/\|\nabla u\|_{L^2(\Omega)} \times 100\%$, the best approximation: $\|\nabla(u - \mathcal{A}_h^{p,q,*}u)\|_{L^2(\Omega)}/$ $\|\nabla u\|_{L^2(\Omega)} \times 100\%$, and their ratio $\|\nabla(u - u_h^{p,0})\|_{L^2(\Omega)}/\|\nabla(u - \mathcal{A}_h^{p,q,*}u)\|_{L^2(\Omega)}$ for Mesh A, B, and C, for $p = 1, ..., 5$, and $q = 0$. We can see that in the preasymptotic range, when $(1 + k^2)h$ is not sufficiently small, the error can grow with decreasing h and increasing p; for example the error $\|\nabla(u - u_h^{p,0})\|_{L^2(\Omega)}$ grows when h is halved from Mesh A to Mesh B for $p = 1, 2$, and for Mesh A, as p is increased from $p = 1$ to $p = 3$, and for Mesh B for $p = 1$ to $p = 2$. On the other hand, the error in the best approximation $\|\nabla(u - \mathcal{A}_h^{p,q,*}u)\|_{L^2(\Omega)}$ decreases monotonically when h is halved and p is increased.

From Table 2.1 it is clearly visible that the pollution effect is smaller for higher order elements, which is in complete agreement with the analysis of Ihlenburg and Babuška [50].

It is clear that the generic statement "for $(1 + k^2)h$ sufficiently small" is not precise enough and more work is needed for coming up with more precise assumptions.

Let us now consider the case of fixed h where the convergence is obtained by increasing p and q. Table 2.2 gives the percent relative error in the GFEM solution $\|\nabla(u - u_h^{p,q})\|_{L^2(\Omega)}/$ $\|\nabla u\|_{L^2(\Omega)} \times 100\%$ for $p = 1, ..., 5$, and $q = 1, ..., 17$, the corresponding percent relative error in the best approximation $\|\nabla(u - \mathcal{A}_h^{p,q,*}u)\|_{L^2(\Omega)}/\|\nabla u\|_{L^2(\Omega)} \times 100\%$ and the value of their ratio $\|\nabla(u - u_h^{p,q})\|_{L^2(\Omega)}/\|\nabla(u - \mathcal{A}_h^{p,q,*}u)\|_{L^2(\Omega)}$ for Mesh A.
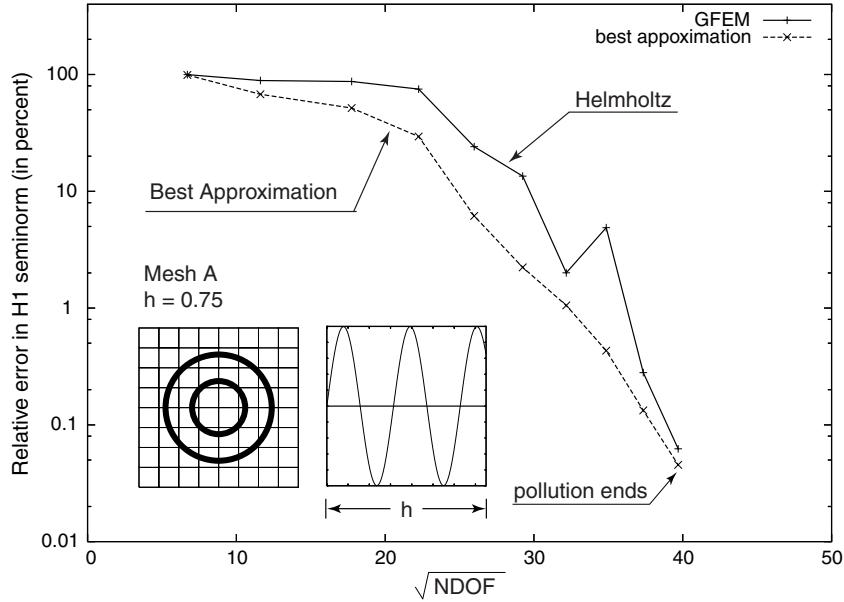
Figure 2.7. q-convergence of the GFEM and best approximation for Mesh A, for $p = 1$.

Note that in Mesh A for $p = 1$ (resp. $p = 2$) the pollution is significant up to $q = 17$ (resp. $q = 11$) and is responsible for the non-monotonic convergence of the GFEM solution. This is because h of Mesh A is not "sufficiently small". However for $p \geq 3$, the same h is sufficiently small and the asymptotic characteristics are achieved for $q \geq 9$ for $p = 3$ and $q \geq 7$ for $p = 4, 5$, and the error in the GFEM Helmholtz solution $u_h^{p,q}$ is very close to the error in the best approximation $\mathcal{A}_h^{p,q}u$. This is visible in Figures 2.7 and 2.8 where we give the convergence of the relative error in the GFEM best approximation and the relative

Table 2.2. The values of the percent relative error in the GFEM solution: $\|\nabla(u - u_h^{p,q})\|_{L^2(\Omega)}/$ $\|\nabla u\|_{L^2(\Omega)} \times 100\%$ (first line), the best approximation: $\|\nabla(u - \mathcal{A}_h^{p,q,*}u)\|_{L^2(\Omega)}/\|\nabla u\|_{L^2(\Omega)} \times 100\%$ (second line), and their ratio: $\|\nabla(u - u_h^{p,q})\|_{L^2(\Omega)}/\|\nabla(u - \mathcal{A}_h^{p,q,*}u)\|_{L^2(\Omega)}$ (third line in parenthesis) for Mesh A.

q	$p = 1$	$p = 2$	$p = 3$	$p = 4$	$p = 5$
	88.8956	92.7851	86.4943	96.5746	71.1913
1	67.7462	65.8201	59.6792	50.0543	38.6725
	(1.3122)	(1.4097)	(1.4493)	(1.9294)	(1.8409)
	87.1527	87.7538	88.3337	80.0862	53.7899
3	51.6927	49.9326	45.1638	37.5849	27.3563
	(1.6860)	(1.7574)	(1.9558)	(2.1308)	(1.9663)
	75.0909	73.6314	72.0024	45.3358	24.6598
5	29.4483	28.5353	26.0802	21.0737	13.6805
	(2.5500)	(2.5804)	(2.7608)	(2.1513)	(1.8026)
	24.0910	22.1618	73.2851	4.4048	2.6819
7	6.1581	5.8758	4.8816	3.6280	2.4309
	(3.9121)	(3.7717)	(15.0120)	(1.2141)	(1.1033)
	13.4984	3.8457	1.9349	1.4073	0.9041
9	2.2310	2.0874	1.7118	1.3216	0.8691
	(6.0502)	(1.8423)	(1.1303)	(1.0648)	(1.0403)
	2.0035	6.0432	0.8395	0.5113	0.3122
11	1.0542	0.9945	0.7800	0.4934	0.3020
	(1.9005)	(6.0766)	(1.0763)	(1.0363)	(1.0338)
	4.8809	0.4536	0.3410	0.2211	0.1409
13	0.4320	0.3936	0.3213	0.2137	0.1376
	(11.2980)	(1.1524)	(1.0613)	(1.0346)	(1.0240)
	0.2800	0.1334	0.1020	0.0758	0.0466
15	0.1329	0.1226	0.0981	0.0740	0.0460
	(2.1068)	(1.0881)	(1.0398)	(1.0243)	(1.0130)
	0.0624	0.0506	0.0359	0.0267	0.0171
17	0.0454	0.0431	0.0351	0.0264	0.0176
	(1.3744)	(1.1740)	(1.0228)	(1.0114)	(0.9716)

error in the Helmholtz GFEM solution versus q for $p = 1$ and $p = 5$. We can clearly see that what h is sufficiently small depends on the employed p.
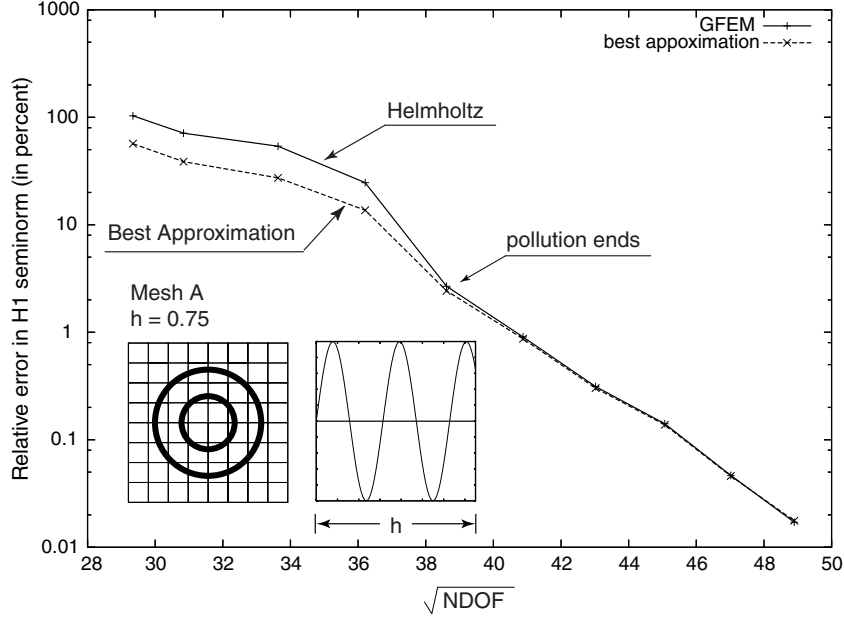
Figure 2.8. q-convergence of the GFEM and best approximation for Mesh A, for $p = 5$.

Figure 2.9 gives the q convergence of the GFEM best approximation and the GFEM Helmholtz solution for Mesh A for $p = 1, ..., 5$ and $q = 0, 1, ..., 17$. Here we employed the square root of the total number of degrees of freedom $\sqrt{NDOF}$ in the horizontal axis. We note that we practically have exponential convergence with

$$\|\nabla(u - u_{\Delta h}^{p,q})\| \approx \mathcal{C} \ e^{-\gamma\sqrt{NDOF}} \tag{2.52}$$

with $\gamma \approx 0.5$. This follows from Theorem 3 and 4 which state that, for sufficiently small h, we have exponential convergence with q. Note that $\sqrt{NDOF}$ is proportional with q.

In Table 2.3 we give the percent relative error in the GFEM solution: $\|\nabla(u-u_h^{p,q})\|_{L^2(\Omega)}/$ $\|\nabla u\|_{L^2(\Omega)} \times 100\%$, the best approximation: $\|\nabla(u - \mathcal{A}_h^{p,q,*}u)\|_{L^2(\Omega)}/\|\nabla u\|_{L^2(\Omega)} \times 100\%$, and their ratio: $\|\nabla(u - u_h^{p,q})\|_{L^2(\Omega)}/\|\nabla(u - \mathcal{A}_h^{p,q,*}u)\|_{L^2(\Omega)}$ for Mesh B, where we obtained the convergence by increasing p and q. We note here that the pollution is much smaller compared with the similar p and q on Mesh A. Note also that for $p = 4, 5$, and $q = 11, 13$, the best approximation $\mathcal{A}_h^{p,q,*}u$ is polluted by the error in the numerical integration of its

Table 2.3. The values of the percent relative error in the GFEM solution: $\|\nabla(u - u_h^{p,q})\|_{L^2(\Omega)}/$ $\|\nabla u\|_{L^2(\Omega)} \times 100\%$ (first line), the best approximation: $\|\nabla(u - \mathcal{A}_h^{p,q,*}u)\|_{L^2(\Omega)}/\|\nabla u\|_{L^2(\Omega)} \times 100\%$ (second line), and their ratio: $\|\nabla(u - u_h^{p,q})\|_{L^2(\Omega)}/\|\nabla(u - \mathcal{A}_h^{p,q,*}u)\|_{L^2(\Omega)}$ (third line in parenthesis) for Mesh B.

q	$p = 1$	$p = 2$	$p = 3$	$p = 4$	$p = 5$
	96.8689	88.0763	67.5157	24.3475	6.2752
1	60.7625	50.2974	29.9357	13.8615	5.1855
	(1.5942)	(1.7511)	(2.2554)	(1.7565)	(1.2101)
	64.3227	44.7225	22.5949	7.5591	2.2876
3	22.7306	19.4872	12.2103	5.5327	2.0518
	(2.8298)	(2.2950)	(1.8505)	(1.3663)	(1.1149)
	4.3863	3.0911	1.7218	0.7393	0.2498
5	3.4416	2.8093	1.6559	0.7305	0.2524
	(1.2745)	(1.1003)	(1.0398)	(1.0120)	(0.9897)
	0.8669	0.6043	0.3044	0.1129	0.0416
7	0.8270	0.5916	0.3018	0.1124	0.0421
	(1.0482)	(1.0215)	(1.0086)	(1.0044)	(0.9881)
	0.1394	0.1048	0.0625	0.0227	0.0087
9	0.1381	0.1041	0.0622	0.0230	0.0094
	(1.0094)	(1.0067)	(1.0048)	(0.9870)	(0.9255)
	0.0215	0.0174	0.0108	0.0019	0.0019
11	0.0214	0.0174	0.0108	0.0053	0.0049
	(1.0047)	(1.0000)	(1.0000)	(0.3585)	(0.3878)
	0.0032	0.0029	0.0019	0.0009	0.0004
13	0.0033	0.0030	0.0024	0.0043	0.0144
	(0.9697)	(0.9667)	(0.7917)	(0.2093)	(0.0278)

right hand side and we are getting the paradoxical behavior that we mentioned earlier. This happens well after the pollution has ended and when we practically have $u_h^{p,q} \approx \mathcal{A}_h^{p,q}u$. This can be clearly seen in Figure 2.10.

In Figure 2.11 we show the q-convergence for $p = 1, ..., 5$ on Mesh C. The results here are practically exact for $q = 7$ and $q = 9$. Comparing Figures 2.10 and 2.11 we see the dependence of the exponential rate of convergence γ on h.
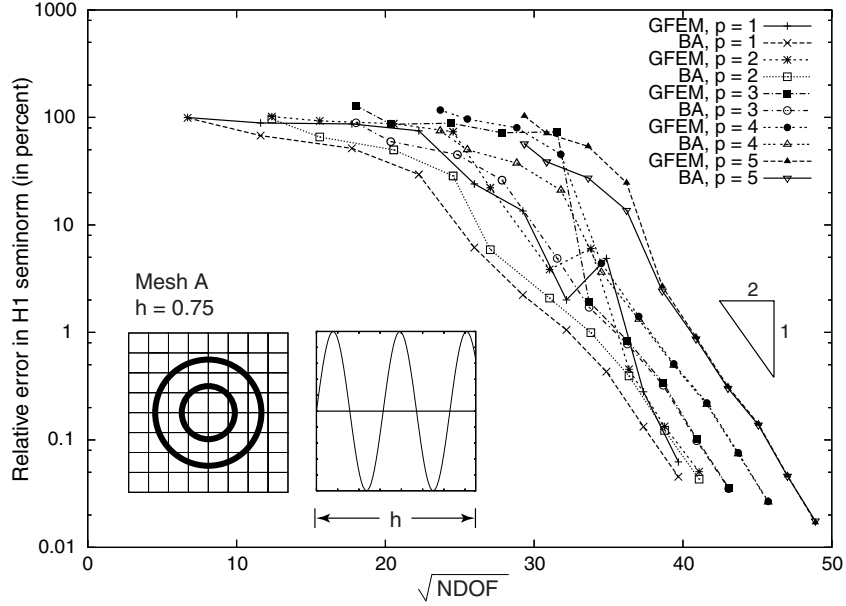
Figure 2.9. q-convergence of the GFEM solution $u_h^{p,q}$ versus the corresponding convergence of the best approximation $\mathcal{A}_h^{p,q,*}u$ for Mesh A, for $p = 1, ..., 5$ and $q = 0, 1, ..., 17$. Note the dependence of the pre-asymptotic range on p.

From the above results we see that the most effective way to employ the Generalized FEM for the Helmholtz is to use a coarse mesh, with $h = \alpha\lambda = \alpha 2\pi/k$, with $\alpha \in (1, 2.5)$ e.g. about 1 or 2 wave length per element, to fix $p = 2$ or 3, and to obtain convergence by increasing q. This is analogous with the p-convergence employed by the commercial code StressCheck and other p-version codes.

Above we answered what is sufficiently small h in the setting of our model example. Now, comparing Tables 2.2 and 2.3 we also see the effect of the numerical integration on the convergence of the best approximation with h.

From Theorems 3 and 4, we expect that for sufficiently small h, we get exponential convergence with p and q, namely

$$\|\nabla(u - u_h^{p,q})\|_{L^2(\Omega)} \approx \mathcal{C}e^{-(\alpha q + \beta p)} \tag{2.53}$$

with $\mathcal{C}, \alpha$, and β depend on h. Let us now analyze the computed results and address the
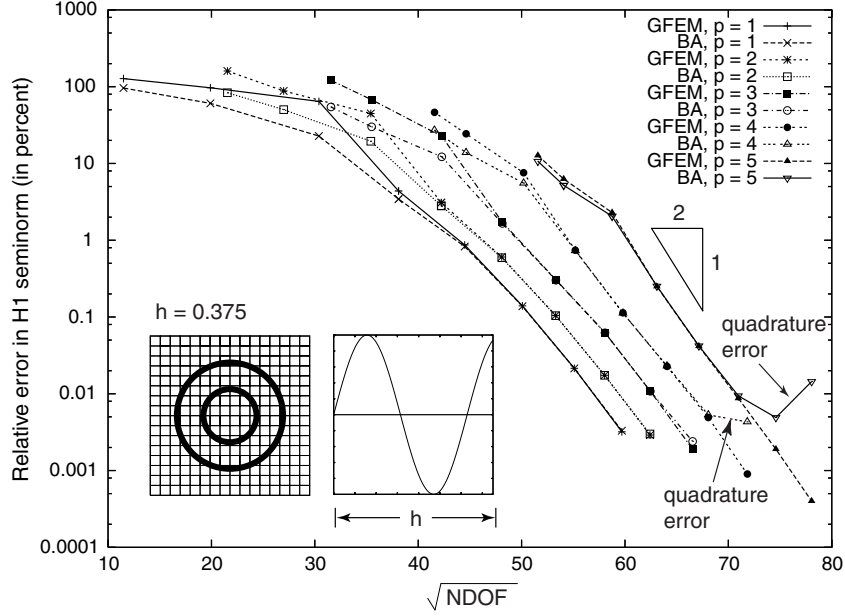
Figure 2.10. q-convergence of the GFEM solution $u_h^{p,q}$ versus the corresponding convergence of the best approximation $\mathcal{A}_h^{p,q,*}u$ for Mesh B, for $p = 1, ..., 5$ and $q = 0, 1, ..., 13$. Note the paradoxical behavior of the best approximation which is due to numerical integration error in the right-hand side of the discrete equations.

exponential rates of the GFEM in our model example. Figures 2.12, 2.13, and 2.14 graph the convergence of the relative error versus q for Mesh A, B, and C, respectively. As expected, for sufficiently small h, we get a linear relationship with p and q, namely

$$\log\left(\frac{\|\nabla(u - u_h^{p,q})\|_{L^2(\Omega)}}{\|\nabla u\|_{L^2(\Omega)}}\right) \approx \log\left(\frac{\mathcal{C}}{\|\nabla u\|_{L^2(\Omega)}}\right) - (\alpha q + \beta p) \tag{2.54}$$

In Figure 2.12 we see oscillations which indicate pre-asymptotic behavior, while most of the results in Mesh B for $q \geq 5$, and Mesh C for $q \geq 3$ are in the asymptotic range. Comparing asymptotic range in these Figures it is clear that the rate of exponential convergence increases as h is refined, for example for Mesh A we have $\alpha \approx 0.5$, for Mesh B $\alpha \approx 0.75$, and for Mesh C $\alpha \approx 1$. The improvement in the exponential rates α as h is decreased can be explained by noting that, as the mesh is refined, the solution becomes smoother locally with respect to the mesh.
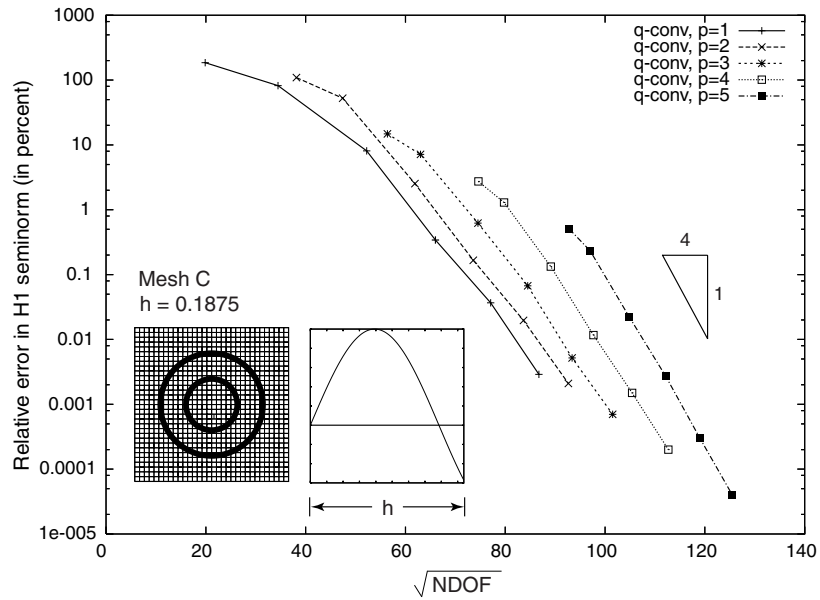
Figure 2.11. q-convergence of the GFEM solution $u_h^{p,q}$ for Mesh C, for $p = 1, ..., 5$, and $q = 0, 1, ..., 9$. Comparing this Figure with Figure 2.10 we see the dependence of the exponential rate of convergence γ with h.
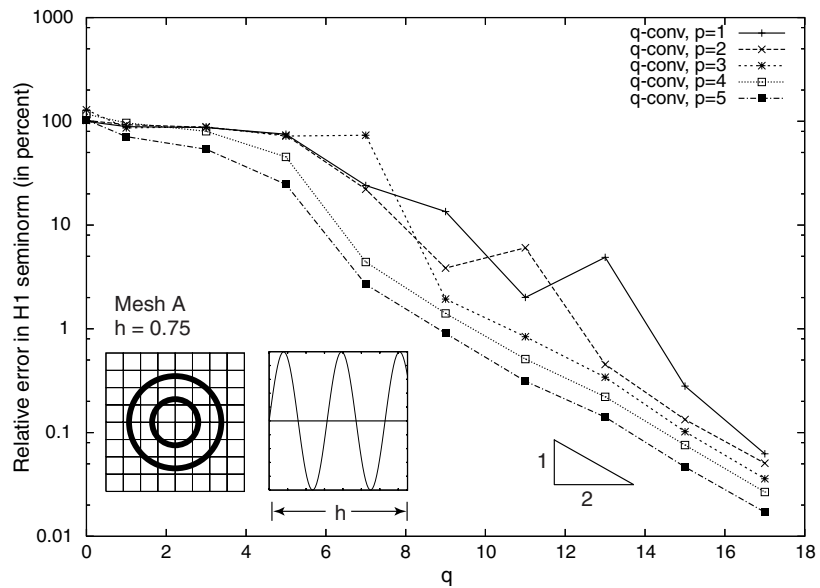
Figure 2.12. q-convergence of the relative error of the GFEM solution $u_h^{p,q}$ for Mesh A versus q, for $p = 1, ..., 5$.
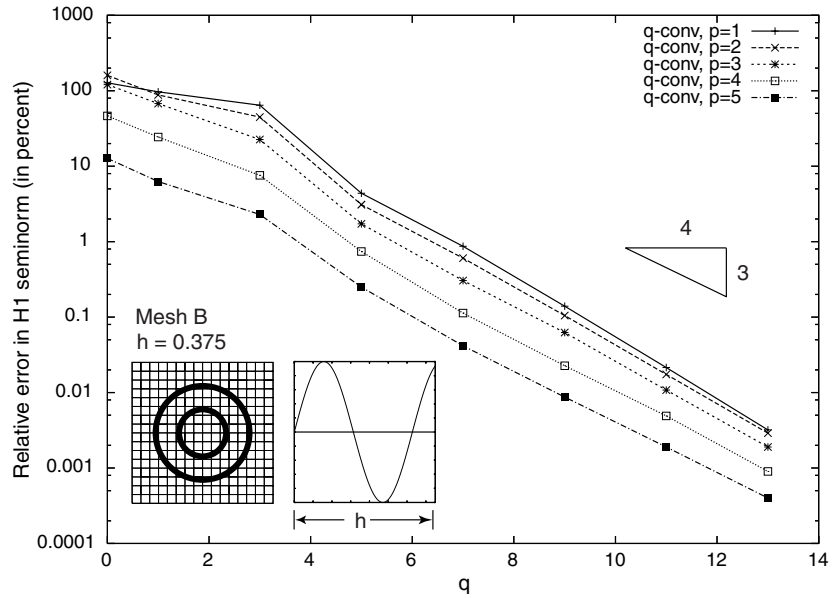
Figure 2.13. q-convergence of the relative error of the GFEM solution $u_h^{p,q}$ for Mesh B versus q, for $p = 1, ..., 5$.
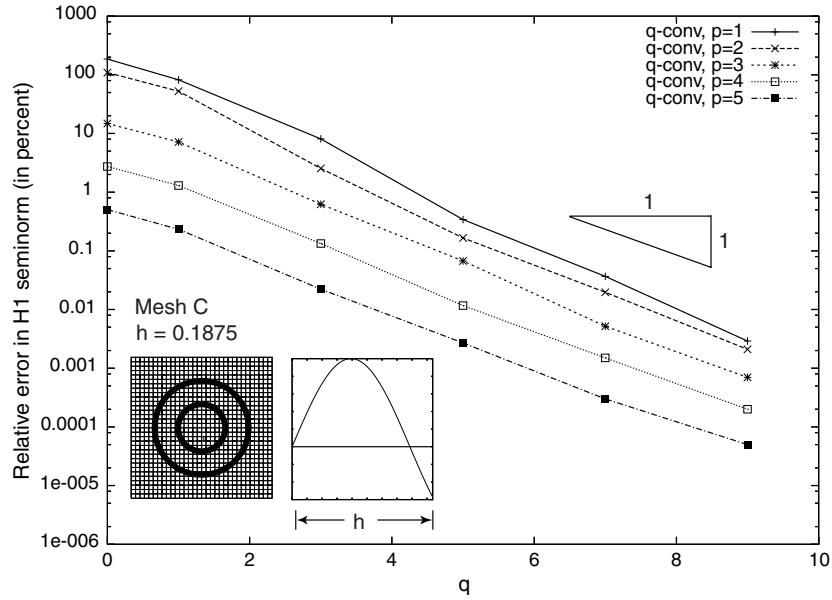
Figure 2.14. q-convergence of the relative error of the GFEM solution $u_h^{p,q}$ for Mesh C versus q, for $p = 1, ..., 5$.

Let us once more underline that here we are mainly interested in the exponential convergence with q, and we use p to limit the extent of the pre-asymptotic range.

2.4   A posteriori estimation using extrapolation

As we have seen above, a main open problem in the solution of the Helmholtz equation by the p-version of the Generalized FEM is when the pollution ends, or equivalently what is sufficiently small h. Although at this moment we cannot answer this question theoretically, we may detect the end of the pollution in a simple a posteriori way. Further, having detected the end of the pollution, in the asymptotic range we can employ extrapolation to obtain reliable error estimators.

Let us give an example of how we can detect the end of the pollution and how we can use q-extrapolation for estimating the error in a computed quantity of interest $\mathcal{F}(u_h^{p,q})$ by extrapolation. Let us underline that before applying any extrapolation we need to make sure that the values employed in the approximation are in the asymptotic range. This can be determined by employing a graph of the value of the computed output $\mathcal{F}(u_h^{p,q})$ versus q or equivalently versus $\sqrt{NDOF}$. Let us, for example, employ the H^1-seminorm of the solution as the quantity of interest, namely $\mathcal{F}(u) = \|\nabla u\|_{L^2(\Omega)}$.

In Figure 2.15 (resp. Figure 2.16) we plotted $\mathcal{F}(u_h^{p,q}) = \|\nabla u_h^{p,q}\|_{L^2(\Omega)}$ versus $\sqrt{NDOF}$ for $p = 1, ..., 5$, and $q = 0, 1, ...17$, for Mesh A (resp. $q = 0, 1, ..., 13$ for Mesh B). From both Figures it is rather easy to detect the end of the pollution and the extent of the asymptotic range for which we expect the extrapolation to give good results. We can now employ the simple extrapolation proposed in (2.41) above to obtain the estimator

$$\mathcal{E}_{\|\nabla u_h^{p,q}\|_{L^2(\Omega)}}^s = \frac{\|\nabla u_h^{p,q+s}\|_{L^2(\Omega)} - \|\nabla u_h^{p,q}\|_{L^2(\Omega)}}{\|\nabla u_h^{p,q+s}\|_{L^2(\Omega)}} \tag{2.55}$$

for the relative error in $\|\nabla u_h^{p,q}\|_{L^2(\Omega)}$. We see that by employing $q = 11, s = 6$ for Mesh A (as reported in Table 2.4), and $q = 7, s = 6$ for Mesh B (as reported in Table 2.5), we

get effectivities between 0.67 and 1.67. It is also possible to employ a more sophisticated extrapolation to extract higher order accuracy, as, e.g. in p. 69 of Babuška and Szabó [49].

Table 2.4. Exact and estimated relative error and its effectivity index for the relative error in $\|\nabla u_h^{p,11}\|_{L^2(\Omega)}$, computed on Mesh A.

p	$\dfrac{\|\nabla u\|_{L^2(\Omega)} - \|\nabla u_h^{p,11}\|_{L^2(\Omega)}}{\|\nabla u\|_{L^2(\Omega)}}$	$\dfrac{\|\nabla u_h^{p,17}\|_{L^2(\Omega)} - \|\nabla u_h^{p,11}\|_{L^2(\Omega)}}{\|\nabla u_h^{p,17}\|_{L^2(\Omega)}}$	θ
1	0.0386 %	0.0379 %	0.9819
2	0.1753 %	0.1748 %	0.9971
3	0.0105 %	0.0105 %	1.0000
4	0.0009 %	0.0006 %	0.6667
5	0.0008 %	0.0010 %	1.2500
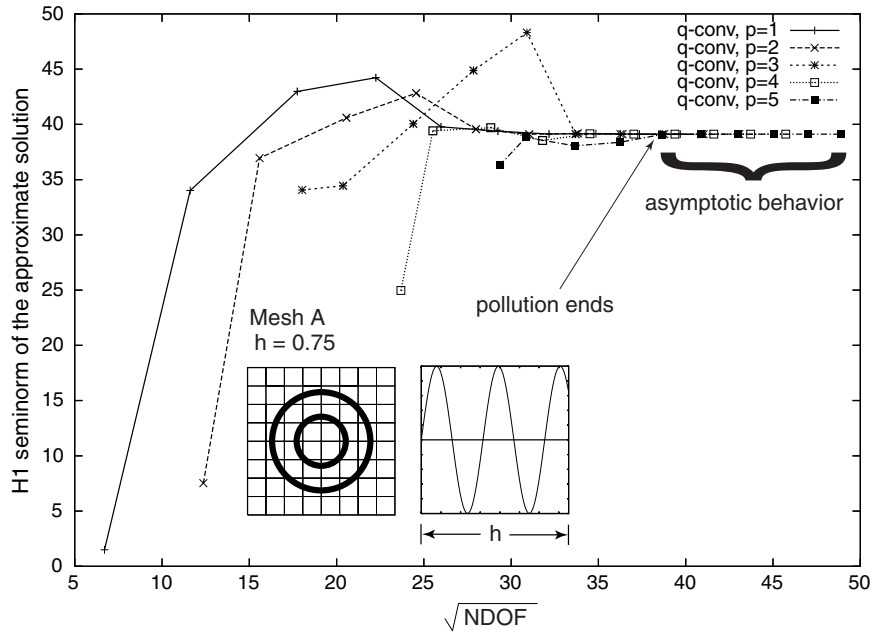
Figure 2.15. Graph of the output $\mathcal{F}(u_h^{p,q}) = \|\nabla u_h^{p,q}\|_{L^2(\Omega)}$ versus $\sqrt{NDOF}$ for Mesh A. From this graph we can detect where the pollution has practically ended and the asymptotic range for which we can employ the extrapolation with good results.

Let us underline that this q-extrapolation approach can be used for the a posteriori estimation of the error in any quantity of interest and does not require any extra coding.

Table 2.5. Exact and estimated relative error and its effectivity index for the relative error in $\|\nabla u_h^{p,7}\|_{L^2(\Omega)}$, computed on Mesh B.

p	$\dfrac{\|\nabla u\|_{L^2(\Omega)} - \|\nabla u_h^{p,7}\|_{L^2(\Omega)}}{\|\nabla u\|_{L^2(\Omega)}}$	$\dfrac{\|\nabla u_h^{p,13}\|_{L^2(\Omega)} - \|\nabla u_h^{p,7}\|_{L^2(\Omega)}}{\|\nabla u_h^{p,13}\|_{L^2(\Omega)}}$	θ
1	0.0085 %	0.0084 %	0.9882
2	0.0057 %	0.0056 %	0.9825
3	0.0005 %	0.0008 %	1.6000
4	0.0001 %	0.0001 %	1.0000
5	0.00003%	0.00005 %	1.6667
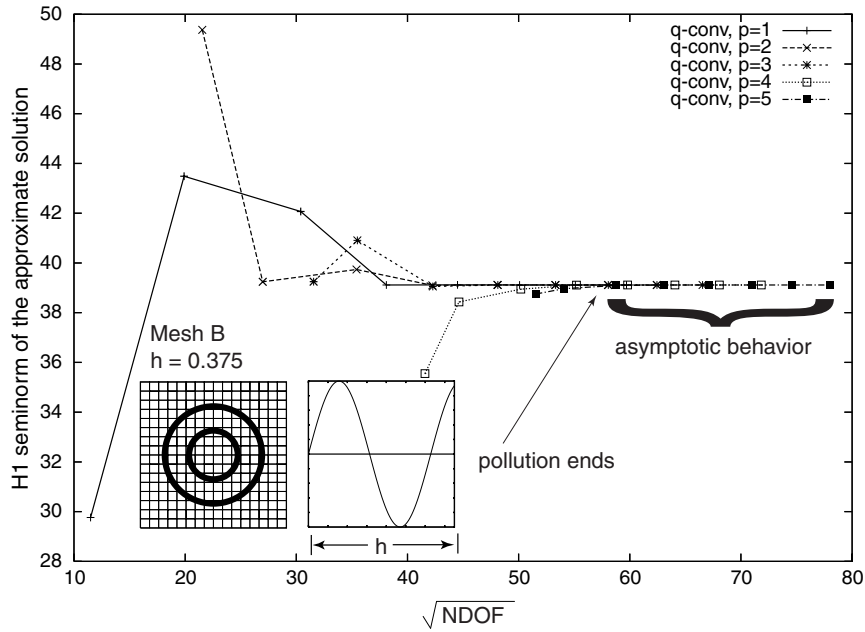
Figure 2.16. Graph of the output $\mathcal{F}(u_h^{p,q}) = \|\nabla u_h^{p,q}\|_{L^2(\Omega)}$ versus $\sqrt{NDOF}$ for Mesh B.

Comparing the results of our a posteriori approach for detecting the end of the pollution and for estimating the error, we see that we get a robust method with respect to the mesh size h. We see that the character of the graphs and the effectivity indices are practically the same for both meshes.

2.5   The effects of perturbation of the mesh

Theoretically, perturbation of the mesh could influence both the approximability and stability of the method, through the constant $\mathcal{C}$ in Theorem 4. To get the idea how much this influence can be we employed a couple of sample computations.
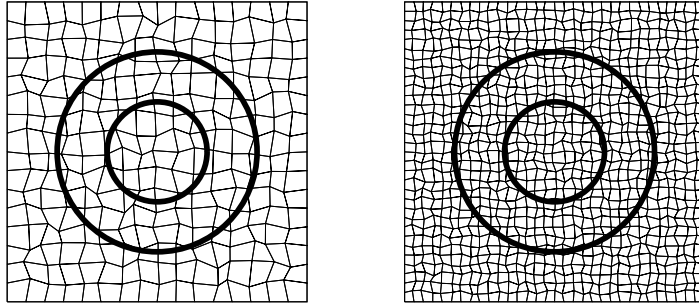
Figure 2.17. Perturbed Mesh B and Mesh C.
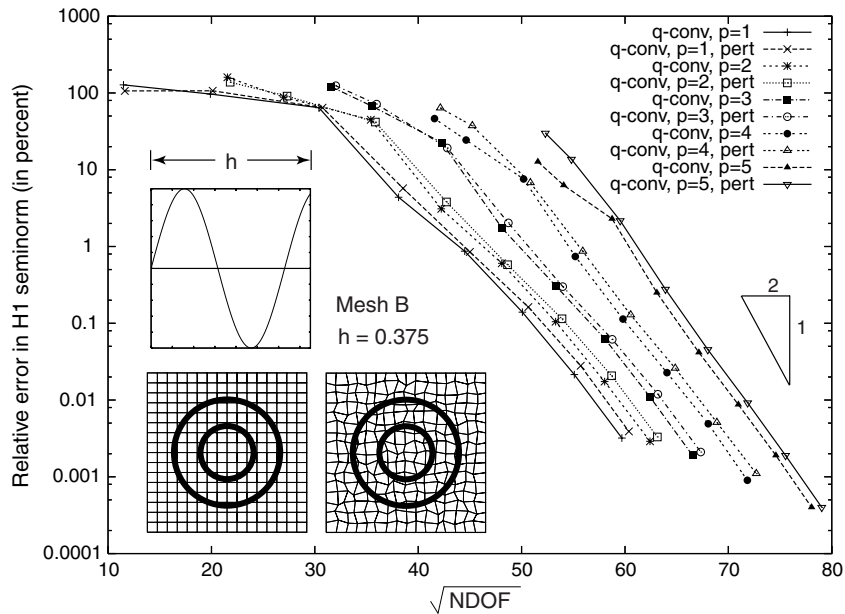
Figure 2.18. Convergence curves for perturbed and unperturbed Mesh B.

To check the sensitivity of the GFEM solution of the Helmholtz problem $u_h^{p,q}$ with respect to perturbations of the mesh, we employed the perturbed Mesh B and Mesh C
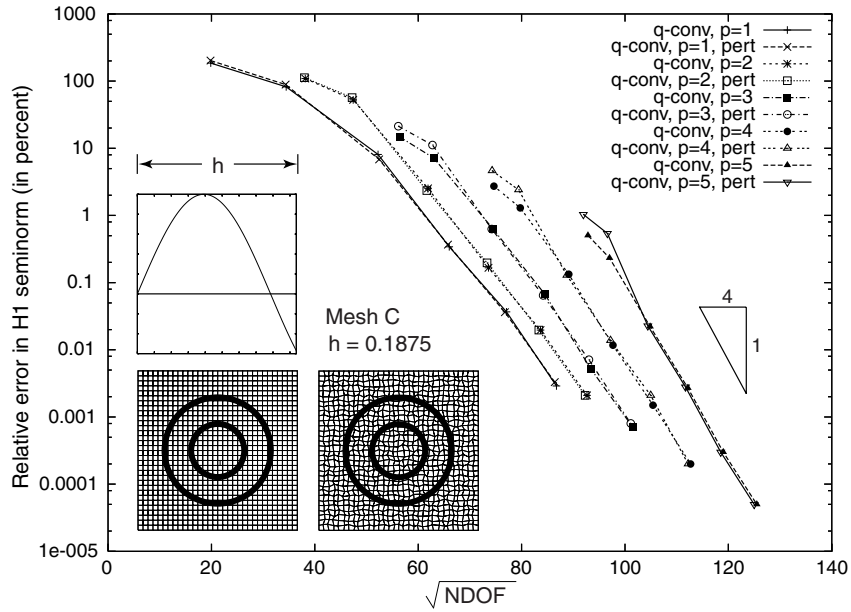
Figure 2.19. Convergence curves for perturbed and unperturbed Mesh C.

shown in Figure 2.17, and in Figures 2.18 and 2.19 we compare the convergence of the relative error for the unperturbed and perturbed meshes. From these graphs it is clear that the convergence of the GFEM solution is not sensitive with respect to perturbations of the nodes of the mesh.

2.6 The effects of roundoff error

The theoretical performance of the method was established under the assumption that there is neither roundoff nor quadrature error. Next we wanted to get an idea of how much the roundoff error can influence the results.

To study the effect of the roundoff error in the convergence of the Generalized FEM solution $u_h^{p,q}$, we employed as our model example, the Helmholtz equation on the unit

square $\Omega = (0,1) \times (0,1)$ with Robin boundary conditions:

$$-\Delta u + k^2 u = 0 \qquad \text{in } \Omega \tag{2.56a}$$

$$\frac{\partial u}{\partial n} + iku = g \qquad \text{on } \partial\Omega \tag{2.56b}$$

where we chose g such that the exact solution is the plane wave

$$u(x,y) = e^{ik(x\cos\theta + y\sin\theta)}, \qquad \theta = \frac{\pi}{16} \tag{2.57}$$

For this example there already exist results by Melenk [16] for $p = 0$, $q = 1, ..., 19$ on uniform N $\times$ N meshes of squares for N =1, 2, 4, and 8.

Tables 2.6 - 2.9 compare the results for the relative error $\|\nabla(u - u_h^{p,q})\|_{L^2(\Omega)}/\|\nabla u\|_{L^2(\Omega)}$ computed using $p = 1$ and $q = 1, 3, ..., 19$, on the 2×2 mesh for $k = 1, 2, 4, 8, 16, 32$, and 64, using Double Precision in the Windows machine (Table 2.6), the Linux machine (Table 2.7), and the results computed using Quadruple Precision in the Unix machine (Table 2.9). The results by Melenk are available in his Ph.D. thesis and is reproduced in Table 2.8. Similar results using 4 $\times$ 4 are given in Tables 2.10 - 2.13.

Table 2.6. Convergence using 2×2 mesh, using Double Precision in Windows machine. The results below the horizontal lines are polluted by the roundoff in Double Precision.

q	k=1.0	k=2.0	k=4.0	k=8.0	k=16.0	k=32.0	k=64.0
1	0.551E-02	0.112E-01	0.236E-01	0.557E-01	0.168E+00	0.614E+00	0.106E+01
3	0.729E-06	0.226E-04	0.625E-03	0.906E-02	0.149E+00	0.618E+00	0.106E+01
5	0.189E-06	0.214E-07	0.689E-06	0.214E-03	0.311E-01	0.730E+00	0.106E+01
7	0.223E-06	0.547E-07	0.138E-07	0.969E-06	0.176E-02	0.283E+00	0.107E+01
9	0.997E-07	0.130E-06	0.184E-07	0.111E-07	0.295E-04	0.874E-01	0.120E+01
11	0.265E-06	0.646E-07	0.108E-06	0.424E-07	0.102E-06	0.985E-02	0.107E+01
13	0.104E-05	0.828E-07	0.105E-06	0.297E-06	0.630E-08	0.177E-03	0.201E+00
15	0.426E-06	0.165E-06	0.654E-07	0.605E-07	0.323E-07	0.698E-06	0.384E-02
17	0.798E-06	0.123E-06	0.168E-06	0.106E-06	0.324E-07	0.843E-08	0.559E-02
19	0.225E-06	0.130E-06	0.120E-06	0.367E-07	0.194E-06	0.709E-08	0.790E-02

Table 2.7. Convergence using 2×2 mesh, using Double Precision in Linux machine.

q	k=1.0	k=2.0	k=4.0	k=8.0	k=16.0	k=32.0	k=64.0
1	0.551E-02	0.112E-01	0.236E-01	0.557E-01	0.168E+00	0.614E+00	0.106E+01
3	0.729E-06	0.226E-04	0.625E-03	0.906E-02	0.149E+00	0.618E+00	0.106E+01
5	0.860E-07	0.201E-07	0.689E-06	0.214E-03	0.311E-01	0.730E+00	0.106E+01
7	0.219E-06	0.589E-07	0.852E-07	0.969E-06	0.176E-02	0.283E+00	0.107E+01
9	0.266E-06	0.552E-07	0.742E-07	0.271E-07	0.295E-04	0.874E-01	0.120E+01
11	0.243E-06	0.124E-06	0.308E-06	0.717E-07	0.102E-06	0.985E-02	0.107E+01
13	0.411E-06	0.121E-06	0.224E-06	0.120E-06	0.702E-08	0.177E-03	0.201E+00
15	0.122E-06	0.785E-07	0.852E-07	0.108E-06	0.256E-07	0.698E-06	0.384E-02
17	0.302E-06	0.203E-06	0.132E-06	0.186E-06	0.741E-07	0.843E-08	0.559E-02
19	0.356E-06	0.668E-07	0.114E-06	0.592E-07	0.476E-07	0.556E-08	0.790E-02

Table 2.8. Convergence using 2×2 mesh, results from Babuška and Melenk

q	k=1.0	k=2.0	k=4.0	k=8.0	k=16.0	k=32.0	k=64.0
1	0.551E-02	0.112E-01	0.236E-01	0.557E-01	0.168E+00	0.614E+00	0.106E+01
3	0.729E-06	0.226E-04	0.625E-03	0.906E-02	0.149E+00	0.618E+00	0.106E+01
5	0.188E-05	0.832E-07	0.689E-06	0.214E-03	0.311E-01	0.730E+00	0.106E+01
7	0.213E-06	0.420E-07	0.140E-07	0.969E-06	0.176E-02	0.283E+00	0.107E+01
9	0.211E-06	0.110E-06	0.281E-07	0.128E-07	0.295E-04	0.874E-01	0.120E+01
11	0.347E-06	0.668E-07	0.470E-07	0.501E-07	0.101E-06	0.985E-02	0.107E+01
13	0.164E-06	0.250E-06	0.191E-06	0.237E-07	0.132E-07	0.177E-03	0.201E+00
15	0.806E-06	0.121E-06	0.115E-05	0.152E-06	0.761E-07	0.698E-06	0.384E-02
17	0.731E-06	0.373E-06	0.980E-07	0.460E-07	0.330E-07	0.843E-08	0.559E-02
19	0.156E-06	0.782E-07	0.995E-06	0.134E-05	0.668E-06	0.158E-01	0.790E-02

Table 2.9. Convergence using 2×2 mesh, using Quadruple Precision in Unix machine.

q	k=1.0	k=2.0	k=4.0	k=8.0	k=16.0	k=32.0	k=64.0
1	0.551E-02	0.112E-01	0.236E-01	0.557E-01	0.168E+00	0.614E+00	0.106E+01
3	0.729E-06	0.226E-04	0.625E-03	0.906E-02	0.149E+00	0.618E+00	0.106E+01
5	0.290E-11	0.146E-08	0.689E-06	0.214E-03	0.311E-01	0.730E+00	0.106E+01
7	0.396E-15	0.161E-13	0.132E-09	0.969E-06	0.176E-02	0.283E+00	0.107E+01
9	0.834E-15	0.255E-15	0.497E-14	0.520E-09	0.295E-04	0.874E-01	0.120E+01
11	0.293E-14	0.219E-14	0.291E-15	0.979E-13	0.102E-06	0.985E-02	0.107E+01
13	0.172E-13	0.945E-15	0.241E-15	0.260E-16	0.908E-10	0.177E-03	0.201E+00
15	0.632E-14	0.502E-15	0.717E-15	0.230E-15	0.821E-14	0.698E-06	0.384E-02
17	0.146E-14	0.396E-15	0.234E-15	0.191E-15	0.468E-17	0.843E-08	0.559E-02
19	0.962E-15	0.376E-15	0.620E-15	0.218E-15	0.196E-15	0.338E-09	0.790E-02

Table 2.10. Convergence using 4×4 mesh, using Double Precision in Windows machine. The results below the horizontal lines are polluted by the roundoff in Double Precision.

q	k=1.0	k=2.0	k=4.0	k=8.0	k=16.0	k=32.0	k=64.0
1	0.275E-02	0.552E-02	0.112E-01	0.236E-01	0.565E-01	0.182E+00	0.691E+00
3	0.919E-07	0.242E-05	0.734E-04	0.181E-02	0.177E-01	0.567E+00	0.704E+00
5	0.986E-07	0.856E-07	0.559E-07	0.198E-04	0.237E-02	0.693E-01	0.732E+00
7	0.151E-06	0.580E-06	0.862E-07	0.259E-07	0.562E-04	0.379E-01	0.823E+00
9	0.298E-06	0.724E-06	0.392E-06	0.571E-07	0.649E-06	0.834E-03	0.164E+00
11	0.165E-06	0.311E-06	0.134E-06	0.178E-06	0.844E-08	0.791E-04	0.417E-01
13	0.321E-06	0.837E-06	0.257E-06	0.130E-06	0.421E-07	0.143E-05	0.464E-02
15	0.357E-05	0.863E-06	0.564E-06	0.185E-06	0.228E-06	0.338E-08	0.137E-03
17	0.167E-06	0.387E-06	0.164E-06	0.199E-06	0.596E-06	0.464E-07	0.217E-04
19	0.172E-06	0.919E-06	0.435E-06	0.239E-06	0.117E-06	0.177E-06	0.175E-04

Table 2.11. Convergence using 4 × 4 mesh, using Double Precision in Linux machine.

q	k=1.0	k=2.0	k=4.0	k=8.0	k=16.0	k=32.0	k=64.0
1	0.275E-02	0.552E-02	0.112E-01	0.236E-01	0.565E-01	0.182E+00	0.691E+00
3	0.919E-07	0.242E-05	0.735E-04	0.181E-02	0.177E-01	0.567E+00	0.704E+00
5	0.986E-07	0.584E-07	0.559E-07	0.198E-04	0.237E-02	0.692E-01	0.732E+00
7	0.907E-07	0.460E-06	0.243E-06	0.259E-07	0.562E-04	0.379E-01	0.823E+00
9	0.488E-06	0.484E-06	0.116E-06	0.120E-06	0.649E-06	0.834E-03	0.164E+00
11	0.662E-06	0.581E-06	0.213E-06	0.116E-06	0.266E-07	0.791E-04	0.417E-01
13	0.124E-06	0.651E-06	0.240E-05	0.132E-06	0.144E-06	0.143E-05	0.464E-02
15	0.191E-06	0.710E-06	0.205E-06	0.228E-06	0.132E-06	0.348E-08	0.137E-03
17	0.619E-06	0.454E-06	0.164E-06	0.308E-06	0.165E-06	0.592E-07	0.217E-04
19	0.358E-06	0.383E-06	0.455E-06	0.386E-06	0.126E-06	0.777E-07	0.175E-04

Table 2.12. Convergence using 4 × 4 mesh, results from Babuška and Melenk

q	k=1.0	k=2.0	k=4.0	k=8.0	k=16.0	k=32.0	k=64.0
1	0.275E-02	0.552E-02	0.112E-01	0.236E-01	0.565E-01	0.182E+00	0.691E+00
3	0.781E-07	0.242E-05	0.735E-04	0.181E-02	0.177E-01	0.567E+00	0.704E+00
5	0.530E-07	0.488E-06	0.559E-07	0.198E-04	0.237E-02	0.692E-01	0.732E+00
7	0.121E-06	0.393E-06	0.105E-06	0.259E-07	0.562E-04	0.379E-01	0.823E+00
9	0.520E-06	0.718E-06	0.308E-06	0.583E-07	0.649E-06	0.834E-03	0.164E+00
11	0.733E-06	0.755E-06	0.246E-06	0.567E-06	0.178E-07	0.791E-04	0.417E-01
13	0.294E-06	0.103E-05	0.282E-06	0.365E-06	0.647E-07	0.143E-05	0.464E-02
15	0.355E-06	0.929E-06	0.591E-06	0.164E-06	0.119E-06	0.350E-08	0.137E-03
17	0.535E-06	0.109E-05	0.162E-06	0.735E-06	0.269E-06	0.185E-06	0.217E-04
19	0.917E-06	0.718E-06	0.402E-06	0.180E-06	0.125E-06	0.572E-07	0.175E-04

Table 2.13. Convergence using 4×4 mesh, using Quadruple Precision in Unix machine.

q	k=1.0	k=2.0	k=4.0	k=8.0	k=16.0	k=32.0	k=64.0
1	0.275E-02	0.552E-02	0.112E-01	0.236E-01	0.565E-01	0.182E+00	0.691E+00
3	0.767E-07	0.242E-05	0.735E-04	0.181E-02	0.177E-01	0.567E+00	0.704E+00
5	0.232E-12	0.117E-09	0.559E-07	0.198E-04	0.237E-02	0.692E-01	0.732E+00
7	0.234E-15	0.597E-15	0.451E-11	0.258E-07	0.562E-04	0.379E-01	0.823E+00
9	0.391E-15	0.166E-14	0.973E-16	0.110E-10	0.649E-06	0.834E-03	0.164E+00
11	0.301E-14	0.302E-14	0.306E-15	0.163E-14	0.154E-08	0.791E-04	0.417E-01
13	0.669E-14	0.355E-15	0.462E-15	0.191E-15	0.832E-12	0.143E-05	0.464E-02
15	0.199E-14	0.827E-15	0.259E-14	0.311E-15	0.788E-16	0.322E-08	0.137E-03
17	0.125E-14	0.120E-14	0.128E-14	0.114E-14	0.739E-16	0.467E-10	0.217E-04
19	0.605E-14	0.830E-14	0.719E-15	0.127E-14	0.140E-15	0.183E-11	0.175E-04

Figures 2.20, 2.21, 2.22, and 2.23 give the convergence graphs for $k = 1, 16, 32$, and 64. Note that for low k the convergence is limited by the machine precision. This is because the employed wave functions are linearly dependent at the limit of zero wave number $k = 0$. Note also that as the wave number k is increased there is small difference due to the machine precision. For example, for $k = 64$, all results practically coincide and the accuracy of the approximation is limited not by the roundoff but by the numerical integration error. Nevertheless, for exact integration, the exponential convergence can always be maintained to smaller relative error by quadruple precision. Similarly, if we had the capability to employ octuple precision we could maintain the exponential convergence to even higher accuracy. All double precision computations (Linux, Windows, Melenk) give practically identical results until the roundoff error becomes significant.

Let us, once more, underline that the difference in the computed results are due to the roundoff effect in the employed direct solver. It is also interesting to note that the various double precision computation give different results, the difference becomes visible when we reach the limit of accuracy below the horizontal line in the columns.

Remark 8: Let us also note that the conditioning of the Partition of Unity Method using
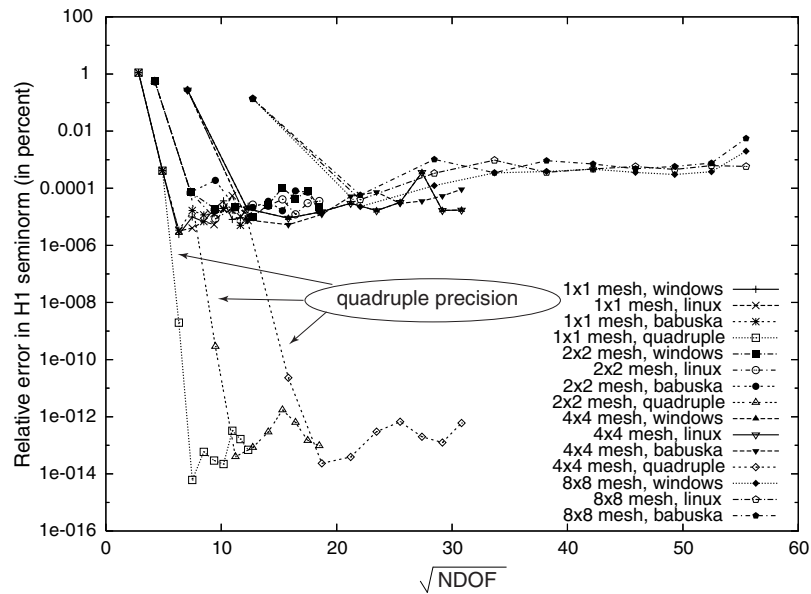
Figure 2.20. Comparison of results of Babuška, Windows machine, Linux machine, and Quadruple Precision for $k = 1$. Here we label only the graphs computed using quadruple precision.
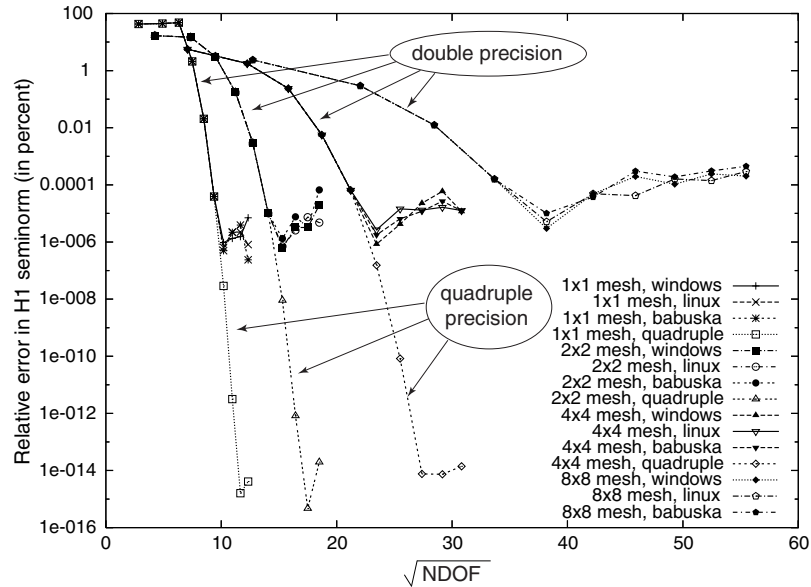
Figure 2.21. Comparison of results of Babuška, Windows machine, Linux machine, and Quadruple Precision for $k = 16$.
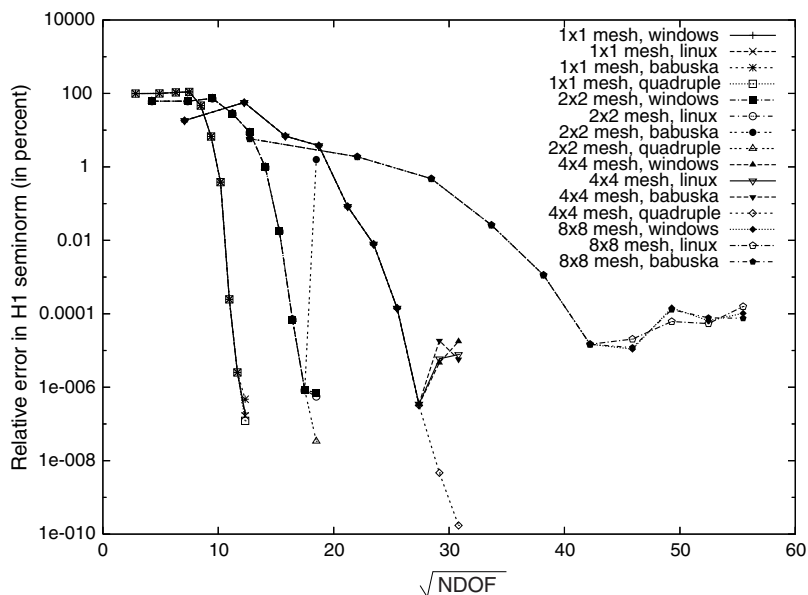
Figure 2.22. Comparison of results of Babuška, Windows machine, Linux machine, and Quadruple Precision for $k = 32$. Note that there is practically only small difference between the results computed in double and quadruple precision.

systems of plane waves has been addressed in the paper by Laghrouche, Bettess, and Astley, where it was concluded that "it is possible to determine 'safe' regions in the $q - k$ domain for which the condition number stays within acceptable limits on an element by element basis ..". For more details see [53].

Remark 9: We have shown the exponential q-convergence of the GFEM for meshes of squares. Similar results can be obtained for other mesh types. Let us, for example, consider the GFEM solution of the rigid scattering model problem. using the meshes shown in Figure 2.24. We see from Figure 2.25 that the robust q-exponential convergence characteristics of the method are realized on all three meshes. Let us also recall that we perturbed the GFEM-III mesh and the perturbations had no effect on the convergence. We expect this robust behavior to the perturbations of the nodes for the other meshes as well.
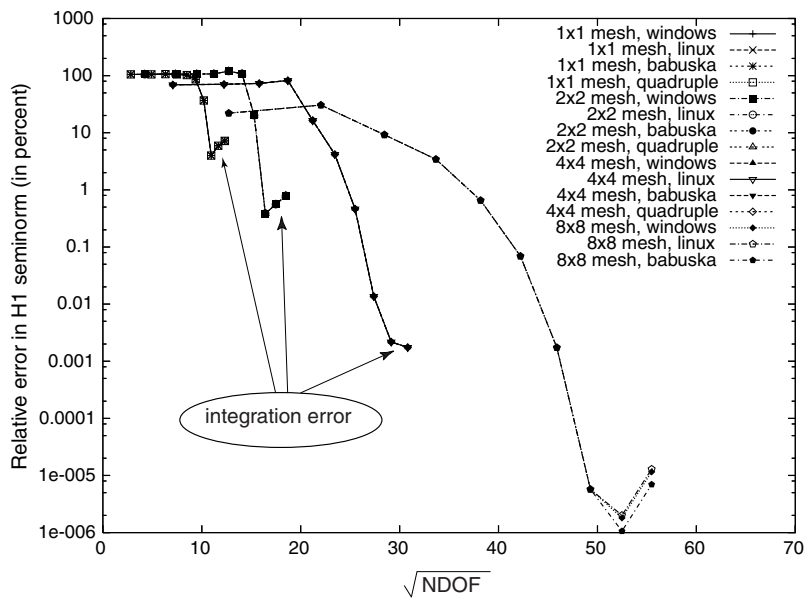
Figure 2.23. Comparison of results of Babuška, Windows machine, Linux machine, and Quadruple Precision for $k = 64$. Note that the results for the computation in double and quadruple precision practically coincides.
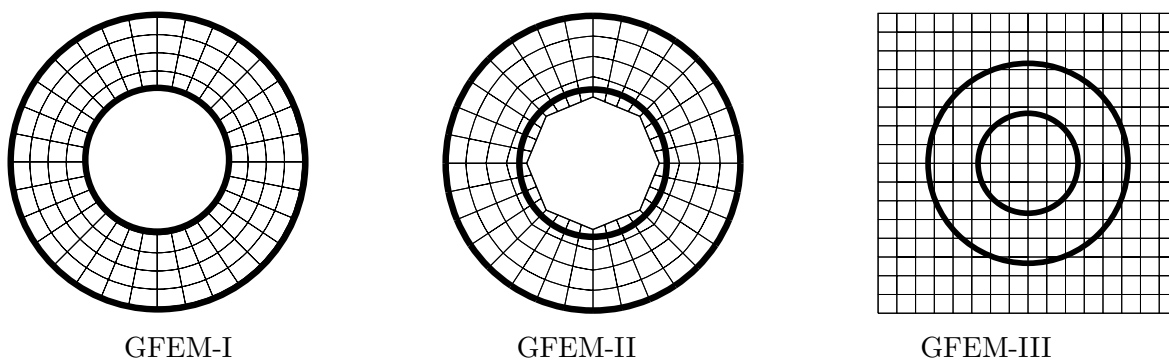
Figure 2.24. Example of various GFEM meshes. The bold lines indicate the boundary of the domain.
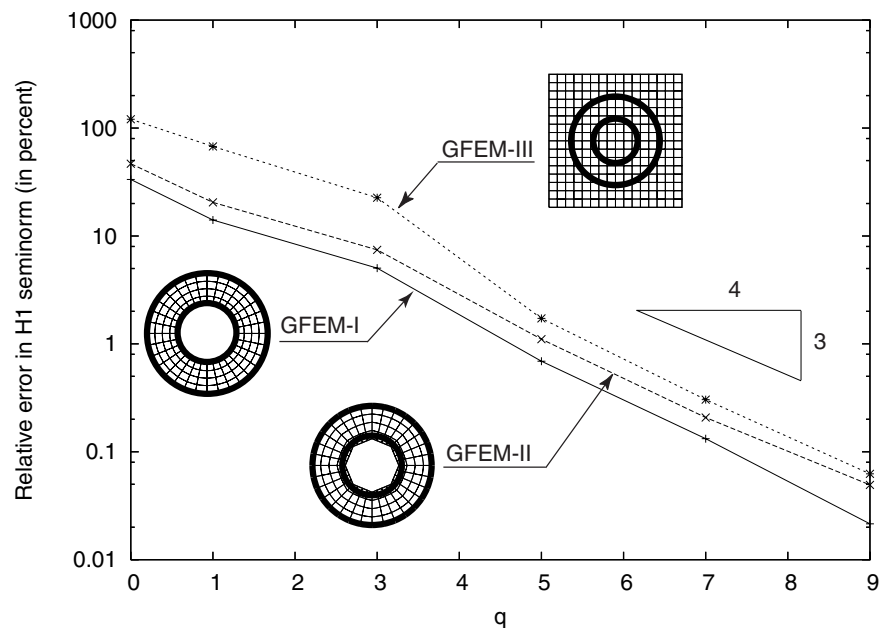
Figure 2.25. *q*-convergence of Model Problem I for $k = 20$ using $p = 3$ and various meshes depicted on Figure 2.24. Note that the GFEM converges exponentially for all three meshes.

CHAPTER III

ANALYSIS OF PLANE-WAVE AND WAVE-BAND HANDBOOK FUNCTIONS IN RECTANGULAR DOMAIN USING PARTITION OF UNITY METHOD*

3.1 Introduction

In this Chapter we will apply the (pure) PUM for solving the Helmholtz equation. Recall the Partition of Unity Space:

$$W_{\Delta_h}^{k;q} = \left\{ v = \sum_{i=1}^{\text{nnodes}} \phi_i^{\Delta_h} \, v_i \quad \Bigg| \quad v_i \in W_{\text{loc}}^{k;q}(\omega_i^{\Delta_h}) \right\} \tag{3.1}$$

where $W_{\text{loc}}^{k;q}$ is the local space of:

a) Plane-wave basis functions:

$$W_{\text{loc}}^{k;q} = \text{span} \left\{ \exp\left(ik\left(x \cos \frac{2\pi n}{q} + y \sin \frac{2\pi n}{q} \right) \right), n = 0, ..., q-1 \right\}, \tag{3.2}$$

which includes all linear combinations of plane waves traveling in the directions $\left(\cos \frac{2\pi n}{q}, \sin \frac{2\pi n}{q} \right)$, $n = 0, ..., q-1$.

b) Wave-band basis functions:

$$W_{\text{loc}}^{k;q} = \text{span} \left\{ \int_{\theta_n}^{\theta_{n+1}} e^{(ik(x \cos \theta + y \sin \theta))} d\theta \quad \Big| \quad n = 0, ..., q-1, \quad \theta_n = \frac{2\pi n - \pi}{q} \right\}, \tag{3.3}$$

which includes all linear combinations of wave bands obtained by superposition of all the plane waves traveling in the directions $(\cos \theta_n, \sin \theta_n)$ to $(\cos \theta_{n+1}, \sin \theta_{n+1})$, $n = 0, ..., q-1$, $\theta_n = (2\pi n - \pi)/q$.

Example of both basis functions are given in Figure 3.1.
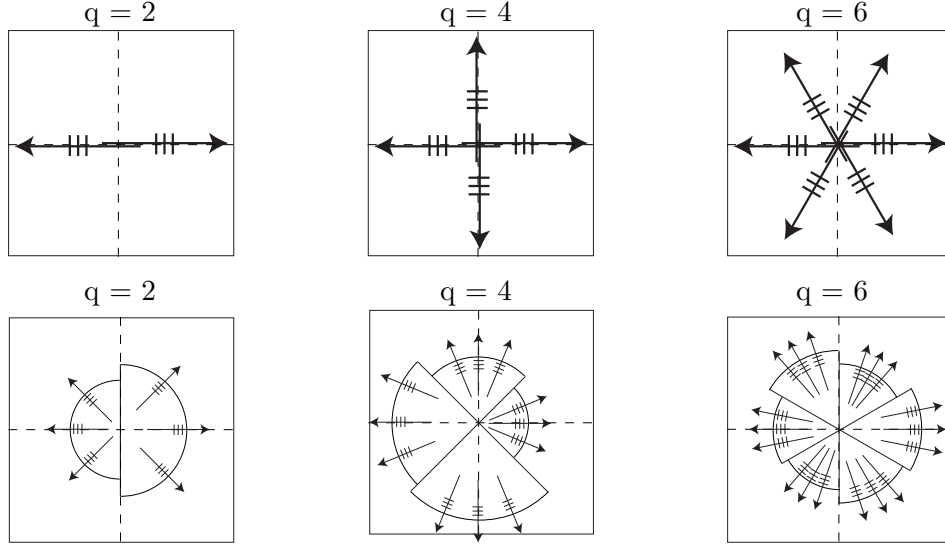
Figure 3.1. Examples of the employed local basis functions. The top row depicts the plane-wave basis, while the bottom row depicts the wave-band basis, for $q = 2,4$, and 6, respectively.

The main objective of this chapter is to introduce the wave-band handbook functions. Both the plane-wave and wave-band functions are similar in terms of the availability of a semi-analytical integration method for the evaluation of the stiffness matrix in the Partition of Unity settings. We will also show the behavior of the pollution in this setting.

3.2 Numerical integration

In Chapter II we used Gauss Legendre numerical integration to evaluate all integrals. Here, in the case of plane waves we will employ a semi-analytical scheme which follows from [22, 46].

Noting that a plane-wave function $W_j^{(m)}(\mathbf{x}) = \exp(ik\mathbf{x} \cdot \mathbf{e}_j)$ satisfies:

$$\nabla W_m^{(j)} = ik\mathbf{e}_m W_m^{(j)} \tag{3.4}$$

we write the typical element of the stiffness matrix:

$$\int_\tau \nabla \left(\phi_r^{\Delta h} W_m^{(r)} \right) \cdot \nabla \left(\phi_s^{\Delta h} W_n^{(s)} \right) - k^2 \left(\phi_r^{\Delta h} W_m^{(r)} \right) \left(\phi_s^{\Delta h} W_s^{(s)} \right) d\tau \tag{3.5}$$

into the form:

$$\int_\tau \exp(ik(\mathbf{e}_m + \mathbf{e}_n)\cdot\mathbf{x})\left[\left(\nabla\phi_r^{\Delta h} + ik\mathbf{e}_m\phi_r^{\Delta h}\right)\cdot\left(\nabla\phi_s^{\Delta h} + ik\mathbf{e}_n\phi_s^{\Delta h}\right) - k^2\phi_r^{\Delta h}\phi_s^{\Delta h}d\tau\right] \quad (3.6)$$

Next we employ the Filon integration rule (see page 151 of [54]) to evaluate (3.6). Recall that Filon's rule is used to integrate highly-oscillatory integrals in the form:

$$\int_a^b f(t)\cos kt\ dt \quad \text{and} \quad \int_a^b f(t)\sin kt\ dt \quad (3.7)$$

by subdividing the interval $[a, b]$ into 2N subintervals of equal length and approximating $f(t)$ by a parabola obtained by interpolating $f(t)$ at mesh points. For rectangular element τ, the integral (3.6) can be written as iterated integral in the x and y directions. Further $\phi_r^{\Delta h}(x, y) = \phi_r^{\Delta h}(x)\phi_r^{\Delta h}(y)$ and thus (3.6) can be split into two 1-D integrals. For example, we have

$$\frac{\partial}{\partial x}\phi_r^{\Delta h}(x, y)\frac{\partial}{\partial x}\phi_s^{\Delta h}(x, y) = \frac{\partial}{\partial x}\phi_r^{\Delta h}(x)\frac{\partial}{\partial x}\phi_s^{\Delta h}(x)\phi_r^{\Delta h}(y)\phi_s^{\Delta h}(y) = F(x)G(y) \quad (3.8)$$

which, after multiplication with $\exp(ik(\mathbf{e}_m + \mathbf{e}_n)\cdot\mathbf{x})$ can be written as:

$$\int_I \cos(\omega_1 x)F(x)dx \int_J \cos(\omega_2 y)G(y)dy - \int_I \sin(\omega_1 x)F(x)dx \int_J \sin(\omega_2 y)G(y)dy$$

$$+i\int_I \sin(\omega_1 x)F(x)dx \int_J \cos(\omega_2 y)G(y)dy + i\int_I \cos(\omega_1 x)F(x)dx \int_J \sin(\omega_2 y)G(y)dy \quad (3.9)$$

with $\omega_1 = k(\cos\theta_m + \cos\theta_n)$ and $\omega_2 = k(\sin\theta_m + \sin\theta_n)$, and each one of the 1-D integrals can be evaluated by Filon's rule.

We performed some computational experiments with $\tau = (0, 1) \times (0, 1)$ and $k = 20$, and computed the stiffness matrix using 40×40 Gauss Legendre Quadrature and Filon's rule with 2 subintervals on x and y coordinate. Analyzing the results for $q = 2, 4, 6, ..., 40$ we found that for $k = 20$ both quadratures give identical results up to the roundoff error, while Filon's rule is always more economical as shown in Figure 3.2.

In the case of wave-band functions, we use $(40 \times 40)^2$ Gauss integration rule; more precisely we use the 40×40 Gauss rule over τ and the 40 point Gauss rule in each band,
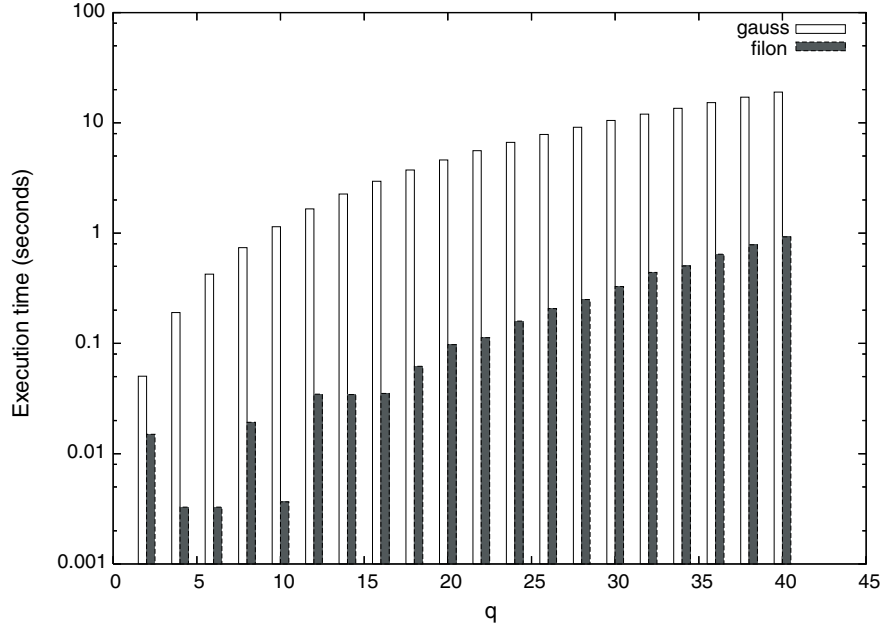
Figure 3.2. Comparison of execution time for computation of stiffness matrices between Gauss Legendre integration and Filon integration.

for example:

$$\int_{\tau} k^2 \left(\phi_r^{\Delta h} \int_{\theta_{r_1}}^{\theta_{r_2}} e^{ik(x \cos \theta + y \sin \theta)} d\theta \right) \left(\phi_s^{\Delta h} \int_{\theta_{s_1}}^{\theta_{s_2}} e^{ik(x \cos \theta + y \sin \theta)} d\theta \right) d\tau \qquad (3.10)$$

is computed by:

$$\sum_{i=1}^{40} \sum_{j=1}^{40} k^2 \left(\hat{\phi}_r^{\Delta h}(\xi_i, \xi_j) \left(\sum_{m=1}^{40} \exp(ik(x(\xi_i) \cos \theta(\xi_m) + y(\xi_j) \sin \theta(\xi_m))) \frac{1}{2} (\theta_{r_2} - \theta_{r_1}) w_m \right) \right)$$
$$\left(\hat{\phi}_s^{\Delta h}(\xi_i, \xi_j) \left(\sum_{n=1}^{40} \exp(ik(x(\xi_i) \cos \theta(\xi_n) + y(\xi_j) \sin \theta(\xi_n))) \frac{1}{2} (\theta_{s_2} - \theta_{s_1}) w_n \right) \right) |J| w_i w_j$$
$$(3.11)$$

where ξ_i and w_i are the Gauss Legendre points and weights respectively, and $\hat{\phi}_s^{\Delta h}$ is the piecewise bilinear "hat" function in the master domain $(1, 1) \times (-1, 1)$. A more economical semi-analytical approach for evaluating the integrals in the case of wave-band functions has been proposed by Ladevèze and Rouch [47].

3.3 Discussion of the computed results

3.3.1 Plane wave on rectangular domain

As our first example, we took the Helmholtz equation on the unit square $\Omega = (0,1) \times (0,1)$ with Robin boundary conditions:

$$-\Delta u + k^2 u \;\; = \;\; 0 \qquad \text{in } \Omega \tag{3.12a}$$

$$\frac{\partial u}{\partial n} + iku \;\; = \;\; g \qquad \text{on } \partial\Omega \tag{3.12b}$$

where we chose g such that the exact solution is the plane wave

$$u(x,y) = e^{ik(x\cos\theta + y\sin\theta)}, \qquad \theta = \frac{\pi}{16} \tag{3.13}$$

Here we let $k = 20$ and we employed uniform N $\times$ N meshes of squares for N = 1, 2, 4, and 8 denoted respectively as mesh A, mesh B, Mesh C, and mesh D. Table 3.1 summarizes the data for the employed meshes: their mesh size h and the respective Number of Waves Per Element (NWPE): $h/\lambda = hk/2\pi$.

Table 3.1. Meshes utilized in the analysis: N is the number of elements in the x and y direction, h is the uniform mesh size, and NWPE is the Number of Waves Per Element.

	N	h	NWPE
Mesh A	1	1.0	3.18
Mesh B	2	0.5	1.59
Mesh C	4	0.25	0.80
Mesh D	8	0.125	0.40

Figure 3.3 plots the percent relative error in the H^1-seminorm with respect to the square root of the total number of degrees of freedom $\sqrt{NDOF}$ in the horizontal axis. Here we can see that asymptotically in both cases we obtain exponential convergence:

$$\|\nabla(u - u_h^q)\| \approx \mathcal{C} \; e^{-\gamma\sqrt{NDOF}} \tag{3.14}$$

where $\mathcal{C}$ depends on h. It is noteworthy that in the pre-asymptotic range the PUM with plane-wave functions delivers much better accuracy than the PUM with wave-band functions, especially as the mesh is refined.
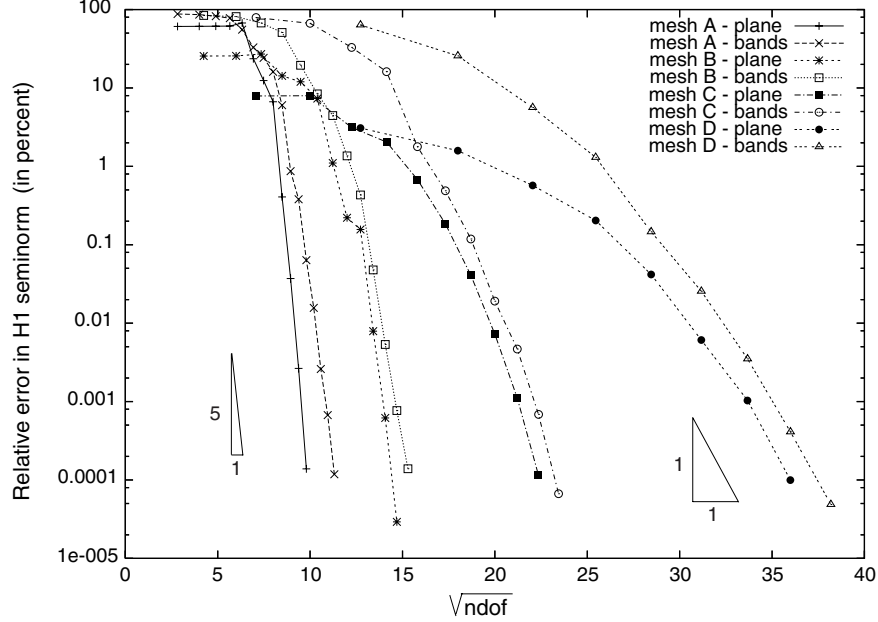
Figure 3.3. q-convergence of the PUM using plane-wave and wave-band functions for Mesh A, B, C, and D.

Tables 3.2 and 3.3 give the values of the percent relative error in the best approximation: $\|\nabla(u - \mathcal{A}_h^q u)\|_{L^2(\Omega)} / \|\nabla u\|_{L^2(\Omega)} \times 100\%$, where $\mathcal{A}_h^q u \in S_h^q$ is such that:

$$\int_\Omega \nabla\left(\mathcal{A}_h^q u\right) \cdot \nabla\bar{v} \; d\Omega = \int_\Omega \nabla u \cdot \nabla\bar{v} \; d\Omega \qquad \forall \, v \in S_h^q \tag{3.15}$$

where u is the analytical solution given by (3.13). Tables 3.2 and 3.3 also give the value of the pollution ratio $\pi_{S_h^q}(u)$ in each case. The deviation of $\pi_{S_h^q}(u)$ from the value one is the measure of the pollution.

Table 3.2. The values of the percent relative error in the best approximation: $\|\nabla(u - \mathcal{A}_h^q u)\|_{L^2(\Omega)}/$ $\|\nabla u\|_{L^2(\Omega)} \times 100\%$ using the plane-wave and wave-band functions for Mesh A and Mesh B. The number inside the bracket is the pollution ratio $\pi_{S_h^q}(u)$, namely the ratio between the percent relative error of the PUM and the best approximation.

q	Mesh A		Mesh B	
	plane	bands	plane	bands
2	.4804E+2	.8673E+2	.1991E+2	.8047E+2
	(1.2656)	(1.0123)	(1.2848)	(1.0461)
4	.4804E+2	.8312E+2	.1982E+2	.7108E+2
	(1.2733)	(1.0367)	(1.2911)	(1.1456)
6	.4784E+2	.7096E+2	.1805E+2	.4562E+2
	(1.2837)	(1.1598)	(1.5014)	(1.4796)
8	.4625E+2	.5731E+2	.7638E+1	.3248E+2
	(1.3328)	(1.3551)	(1.8657)	(1.5727)
10	.3085E+2	.3296E+2	.4529E+1	.9547E+1
	(2.1812)	(1.6811)	(2.6496)	(2.0383)
12	.1435E+2	.2343E+2	.2794E+1	.3684E+1
	(1.6432)	(1.4063)	(2.6249)	(2.2801)
14	.5856E+1	.1316E+2	.7339E+0	.1618E+1
	(2.1209)	(1.8404)	(1.5043)	(2.7466)
16	.1770E+1	.5150E+1	.1674E+0	.8736E+0
	(3.7616)	(3.1204)	(1.3202)	(1.5545)
18	.3616E+0	.1392E+1	.3489E-1	.1903E+0
	(1.1258)	(4.3197)	(4.4855)	(2.2648)
20	.3653E-1	.3663E+0	.7387E-2	.3766E-1
	(1.0151)	(2.3713)	(1.0700)	(1.2690)
22	.2615E-2	.1123E+0	.5557E-3	.5128E-2
	(1.0134)	(3.3856)	(1.1110)	(1.0429)
24	.1375E-3	.3232E-1	.2834E-4	.7461E-3
	(1.0058)	(1.9706)	(1.0296)	(1.0288)
26		.1024E-1		.1354E-3
		(1.5303)		(1.0258)
28		.2311E-2		
		(1.1255)		
30		.6362E-3		
		(1.0544)		
32		.1157E-3		
		(1.0225)		

Table 3.3. The values of the percent relative error in the best approximation: $\|\nabla(u - \mathcal{A}_h^q u)\|_{L^2(\Omega)}/$ $\|\nabla u\|_{L^2(\Omega)} \times 100\%$ using the plane-wave and wave-band functions for Mesh C and Mesh D. The number inside the bracket is the pollution ratio $\pi_{S_h^q}(u)$, namely the ratio between the percent relative error of the PUM and the best approximation.

q	Mesh C		Mesh D	
	plane	bands	plane	bands
2	.6740E+1	.6768E+2	.2899E+1	.3725E+2
	(1.1723)	(1.1674)	(1.0617)	(1.7044)
4	.6499E+1	.4382E+2	.1530E+1	.1980E+2
	(1.2267)	(1.5224)	(1.0333)	(1.2924)
6	.2898E+1	.2084E+2	.5649E+0	.5031E+1
	(1.0849)	(1.5763)	(1.0110)	(1.1175)
8	.1963E+1	.7755E+1	.2036E+0	.1276E+1
	(1.0413)	(2.0812)	(1.0025)	(1.0219)
10	.6265E+0	.1680E+1	.4171E-1	.1460E+0
	(1.0817)	(1.0589)	(1.0012)	(1.0034)
12	.1832E+0	.4780E+0	.6085E-2	.2551E-1
	(1.0153)	(1.0201)	(1.0015)	(1.0027)
14	.4013E-1	.1173E+0	.1033E-2	.3496E-2
	(1.0125)	(1.0119)	(1.0010)	(1.0014)
16	.7176E-2	.1890E-1	.9904E-4	.4094E-3
	(1.0111)	(1.0064)	(1.0026)	(1.0007)
18	.1099E-2	.4635E-2		.4858E-4
	(1.0055)	(1.0080)		(1.0016)
20	.1132E-3	.6812E-3		
	(1.0133)	(1.0060)		
22		.6593E-4		
		(1.0102)		

Figure 3.4 (resp. Figure 3.5) shows the graph of the percent relative error in the PUM solution and the best approximation for plane-wave (resp. wave-bands) PUM space. We can see from both figures that for sufficiently high q depending on h, the solution converges

exponentially as:

$$\|\nabla(u - u_h^q)\| \approx \mathcal{C}_1 \; e^{-\beta q} \tag{3.16}$$

with the same rate $\beta \approx 1$. Note also that as the mesh is refined, the effect of the pollution is practically negligible almost starting from $q = 2$.
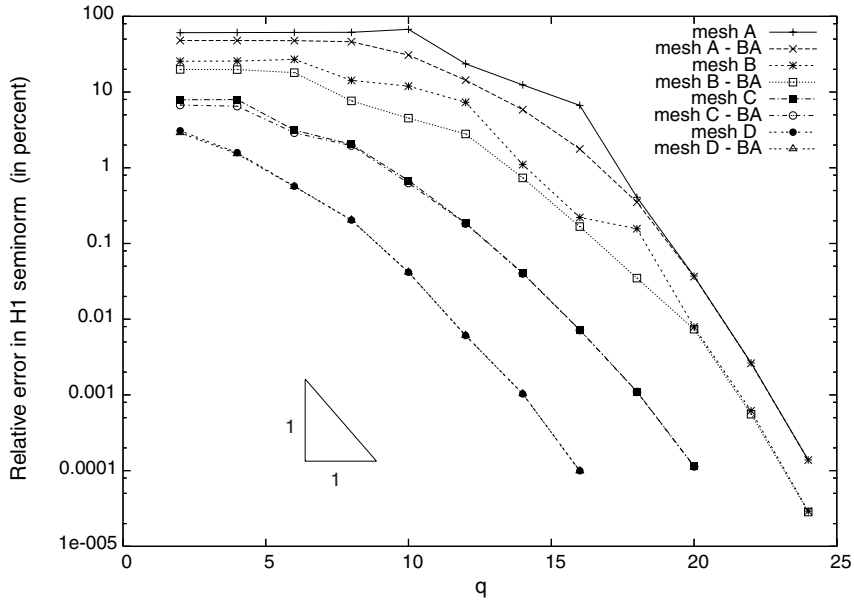
Figure 3.4. q-convergence of the PUM and best approximation for Mesh A, B, C, and D computed using plane-wave functions.

In summary, it seems that for the problem with the exact solution given by (3.13) the PUM using plane-wave functions performs better than the PUM using wave-band functions especially for small h and high q. For large h and low q the PUM using bands has smaller pollution ratio. The better performance of the PUM using plane-wave functions can be partially explained from the fact that the exact solution is also a plane wave.

3.3.2 Rigid scattering problem

We obtained our second example by employing the analytical solution of scattering of a plane wave by a rigid circular cylinder, which is depicted in Figure 3.6. Employing cylindrical
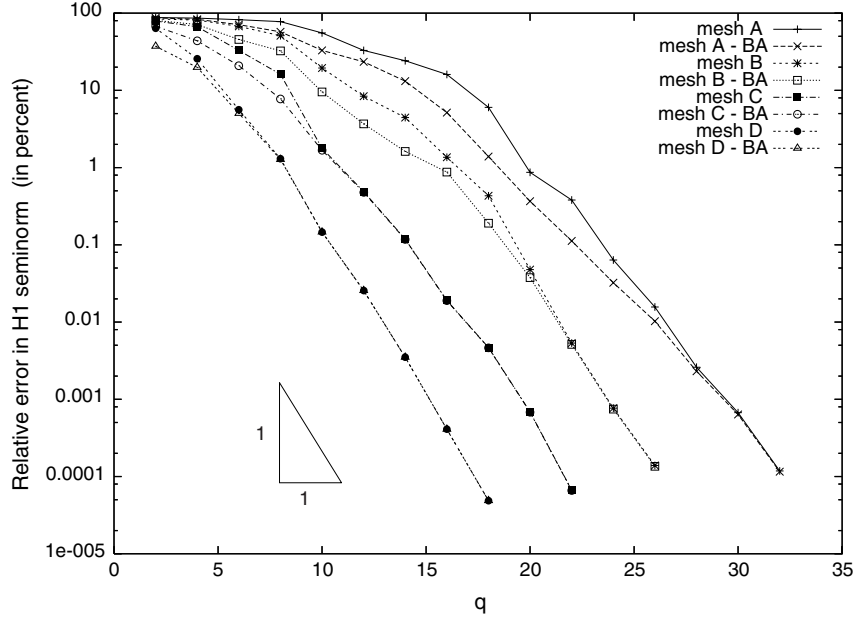
Figure 3.5. q-convergence of the PUM and best approximation for Mesh A, B, C, and D computed using wave-bands functions.

coordinates (r, θ), the boundary value problem for the scattered pressure $u(r, \theta)$ reads:

$$\nabla^2 u + k^2 u = 0, \qquad r > a \tag{3.17a}$$

$$\frac{\partial u}{\partial r} = -\frac{\partial}{\partial r}(u_{\text{inc}}), \qquad r = a \tag{3.17b}$$

$$\lim_{r \to \infty} \sqrt{r} \left(\frac{\partial u}{\partial r} - iku \right) = 0 \tag{3.17c}$$

where:

$$u_{\text{inc}}(r, \theta) = P_0 \, e^{ikr \cos \theta} \tag{3.18}$$

is the pressure field for the incident plane wave. Using separation of variables (see, e.g., p. 412 in Jones [52]) we obtain:

$$u(r, \theta) = -P_0 \sum_{n=0}^{\infty} \epsilon_n i^n \frac{J_n'(ka) H_n(kr)}{H_n'(ka)} \cos(n\theta) \tag{3.19}$$

where $\epsilon_0 = 1, \epsilon_n = 2, n \neq 0$, $H_n(z)$ is the cylindrical Hankel function of the first kind, and $J_n(z)$ is the cylindrical Bessel function of the first kind. We set our example problem in square domains $\Omega_i, i = 1, 2$, adjacent to the scatterer and employed (3.19) to obtain g on $\partial \Omega_i$.
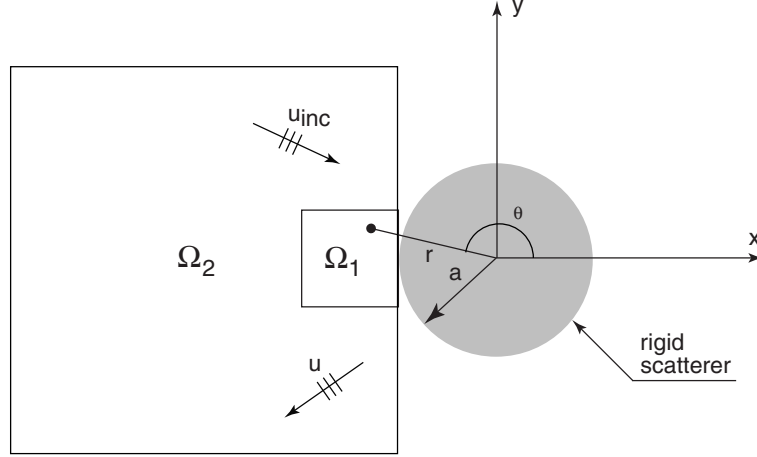
Figure 3.6. Notations used in the definition of the model example of scattering of a plane wave by a rigid circular scatterer and the problem domains Ω_i.

In our computations we employed $k = 20$, and the domains $\Omega_1 = (-2, -1) \times (-0.5, 0.5)$ and $\Omega_2 = (-5, -1) \times (-2, 2)$. As in the previous example, we employed uniform meshes of squares obtained from nested refinements of the domains Ω_i. We report the values of the percent relative error in the best approximation and the value of the pollution ratio $\pi_{S_h^q}(u)$ in Tables 3.4 and 3.5 for computations performed on Ω_1.

Figure 3.7 reports the convergence of the H^1-seminorm of the error with increasing q using domain Ω_1. Note that for this example the PUM with wave-band functions gives better accuracy in the pre-asymptotic range as compared with the PUM with plane-wave functions. Asymptotically, both choices give almost identical accuracies converging exponentially with respect to $\sqrt{NDOF}$.

Table 3.4. The values of the percent relative error in the best approximation: $\|\nabla(u - \mathcal{A}_h^q u)\|_{L^2(\Omega)}/$ $\|\nabla u\|_{L^2(\Omega)} \times 100\%$ using the plane-wave and wave-band functions for domain Ω_1 on Mesh A and Mesh B. The number inside the bracket is the pollution ratio $\pi_{S_h^q}(u)$, namely the ratio between the percent relative error of the PUM and the best approximation.

q	Mesh A		Mesh B	
	plane	bands	plane	bands
2	.7258E+2	.3489E+2	.4037E+2	.1520E+2
	(1.1730)	(1.0957)	(1.2527)	(1.0579)
4	.7246E+2	.2851E+2	.3968E+2	.1198E+2
	(1.1736)	(1.2936)	(1.2679)	(1.4349)
6	.7114E+2	.1110E+2	.2613E+2	.5189E+1
	(1.2003)	(1.3802)	(1.9644)	(2.6768)
8	.6081E+2	.8525E+1	.7795E+1	.5413E+1
	(1.2263)	(1.9132)	(1.3765)	(1.9656)
10	.3556E+2	.8341E+1	.4654E+1	.4028E+1
	(2.3332)	(1.7995)	(1.0765)	(1.8841)
12	.1477E+2	.6529E+1	.2303E+1	.1845E+1
	(1.7258)	(1.5944)	(2.1806)	(8.0000)
14	.3811E+1	.3451E+1	.5460E+0	.3458E+0
	(1.9234)	(2.8708)	(2.0751)	(1.5058)
16	.1175E+1	.1771E+1	.1805E+0	.1500E+0
	(3.9566)	(2.4032)	(1.0820)	(1.4767)
18	.5348E+0	.6593E+0	.5723E-1	.4223E-1
	(1.1887)	(4.6519)	(10.666)	(1.0992)
20	.8084E-1	.1250E+0	.1443E-1	.9467E-2
	(1.0143)	(3.4384)	(1.0804)	(1.1049)
22	.2748E-1	.2894E-1	.4479E-2	.2362E-2
	(1.0124)	(1.5463)	(1.0554)	(1.0868)
24	.7721E-2	.2005E-1	.1527E-2	.9474E-3
	(1.0060)	(1.1546)	(1.0308)	(1.0278)
26	.2357E-2	.9657E-2	.5843E-3	.3069E-3
	(1.0076)	(1.3410)	(1.0199)	(1.0713)
28	.7026E-3	.4007E-2	.2269E-3	
	(1.0080)	(1.0177)	(1.0220)	
30	.3876E-3	.1582E-2		
	(0.5575)	(1.0076)		

Table 3.5. The values of the percent relative error in the best approximation: $\|\nabla(u - \mathcal{A}_h^q u)\|_{L^2(\Omega)}/$ $\|\nabla u\|_{L^2(\Omega)} \times 100\%$ using the plane-wave and wave-band functions for domain Ω_1 on Mesh C and Mesh D. The number inside the bracket is the pollution ratio $\pi_{S_h^q}(u)$, namely the ratio between the percent relative error of the PUM and the best approximation.

q	Mesh C		Mesh D	
	plane	bands	plane	bands
2	.2386E+2	.1101E+2	.1146E+2	.8322E+1
	(1.2871)	(1.0836)	(1.1536)	(1.4215)
4	.2123E+2	.5751E+1	.4728E+1	.3786E+1
	(1.4932)	(1.7736)	(1.0992)	(1.6302)
6	.5917E+1	.2284E+1	.1185E+1	.6250E+0
	(1.1256)	(1.5639)	(1.0118)	(1.1162)
8	.1913E+1	.1836E+1	.2475E+0	.2463E+0
	(1.0538)	(14.336)	(1.0016)	(1.0154)
10	.5796E+0	.6442E+0	.3747E-1	.5907E-1
	(1.0851)	(1.1956)	(1.0011)	(1.0242)
12	.1561E+0	.1067E+0	.5026E-2	.7836E-2
	(1.0167)	(1.0309)	(1.0012)	(1.0046)
14	.2860E-1	.2460E-1	.7434E-3	.7177E-3
	(1.0157)	(1.0171)	(1.0019)	(1.0022)
16	.5533E-2	.7578E-2	.7716E-4	.1250E-3
	(1.0074)	(1.0227)	(0.9999)	(1.0008)
18	.1418E-2	.1072E-2		
	(1.0085)	(1.0075)		
20	.2430E-3	.1942E-3		
	(1.0325)	(1.0051)		

Figure 3.8 (resp. Figure 3.9) plots the percent relative error in the PUM solution versus the corresponding error in the best approximation for the plane-wave basis (resp. wave-band basis) using domain Ω_1. Once more we see that we get exponential convergence with respect to q, for sufficiently high q depending on h with rate $\beta \approx 1$.
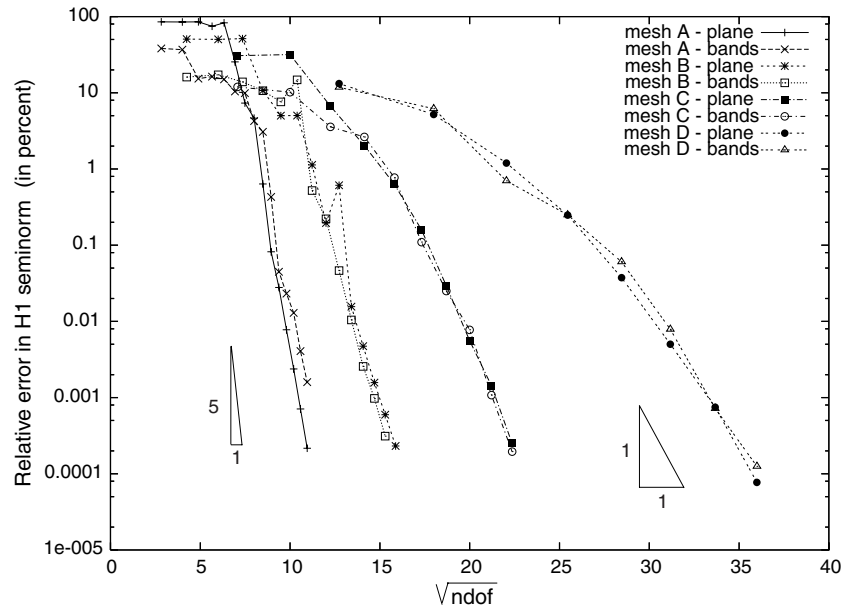
Figure 3.7. *q*-convergence of the PUM using plane-wave and wave-band functions for domain Ω_1 using Mesh A, B, C, and D.
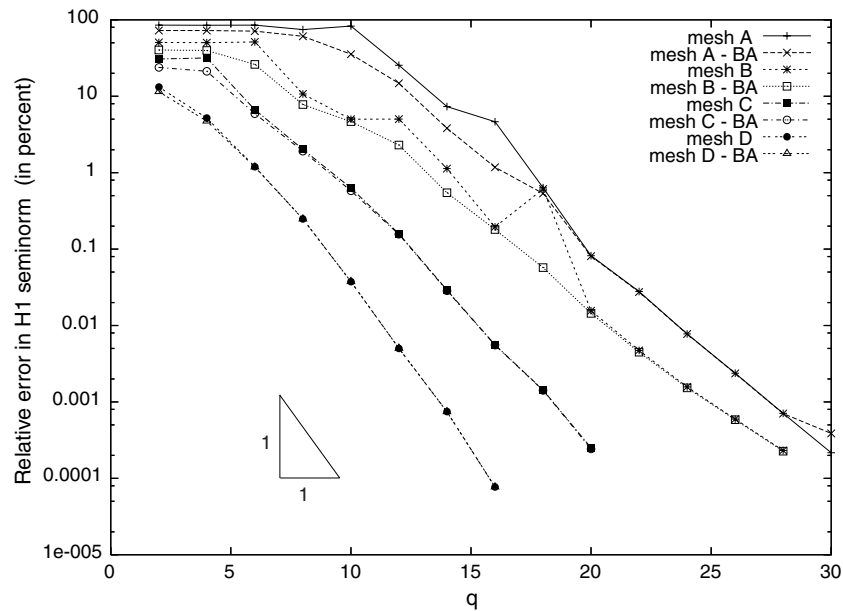
Figure 3.8. *q*-convergence of the PUM and best approximation for domain Ω_1 using Mesh A, B, C, and D computed using plane-wave functions.
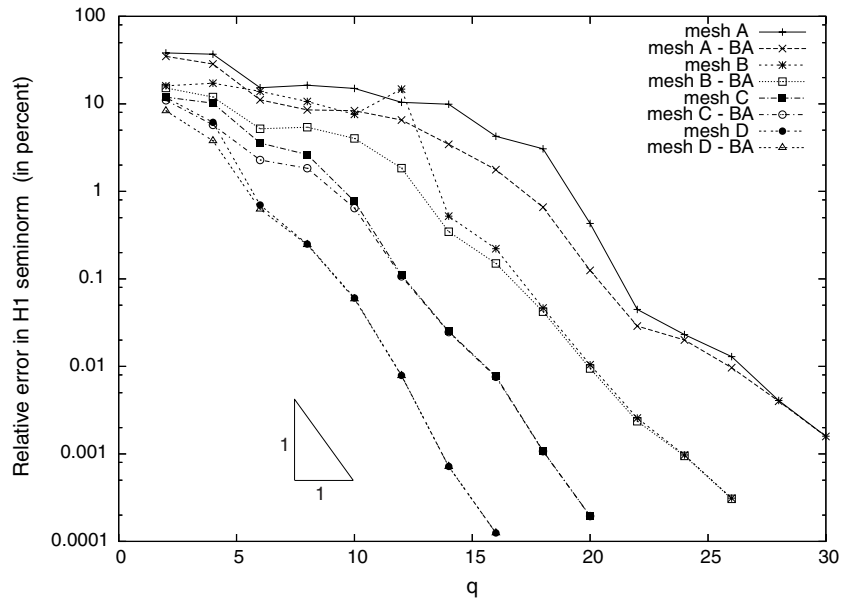
Figure 3.9. q-convergence of the PUM and best approximation for domain Ω_1 using Mesh A, B, C, and D computed using wave-bands functions.
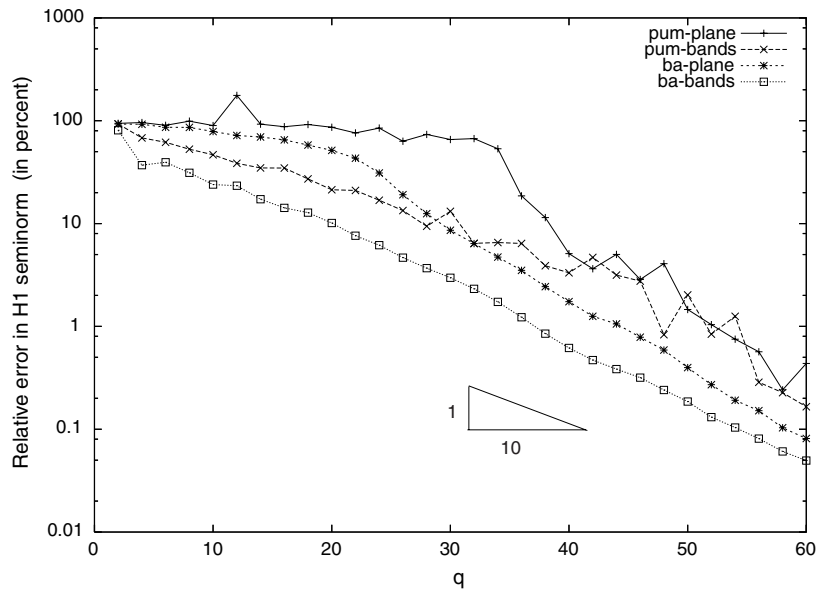
Figure 3.10. q-convergence of the PUM and best approximation for domain Ω_2 using uniform 2×2 mesh computed using plane-wave and wave-bands functions.
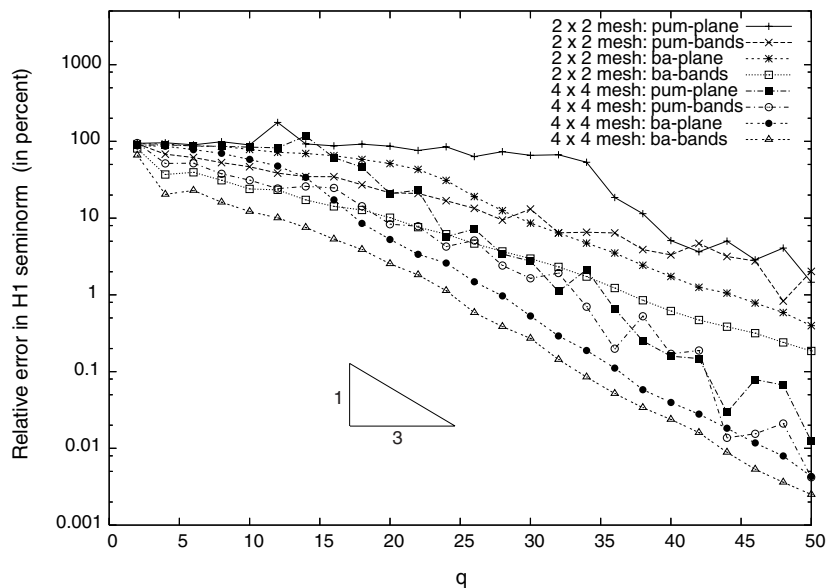
Figure 3.11. q-convergence of the PUM and best approximation for domain Ω_2 using uniform 2×2 and 4×4 mesh computed using plane-wave and wave-bands functions.

In Figure 3.10 we plot the result of computation on the domain Ω_2 using uniform 2×2 mesh, such that the number of waves per element NWPE ≈ 6.37, while in Figure 3.11 we also include the results for the 4×4 mesh for which NWPE ≈ 3.18. Note that the pollution is significant for both bases and for almost the entire range of q for both meshes, and that the rate of exponential convergence improves as the mesh is refined.

From the above results we see that for "smooth" solutions, the PUM with wave-band functions perform better than plane-wave functions while stability is the same for both bases. Theoretical understanding is not available although the smoothness of the solution obviously plays a role. The problem relates to the approximation properties of the basis functions employed on the circle of the Fourier symbol of the equation.

3.3.3 A posteriori error estimation by q-extrapolation

The exponential rate of convergence of the PUM solution with respect to q enables us to use a simple a posteriori error estimation by extrapolation as outlined in [49]. Another approach for a posteriori estimation of PUM can be found in [55].

Assuming that the quantity of interest converges exponentially exactly like (3.16) we have:

$$\log \frac{\mathcal{F}(u) - \mathcal{F}(u_h^q)}{\mathcal{F}(u) - \mathcal{F}(u_h^{q-2})} \approx \log \frac{e^{-\beta q}}{e^{-\beta(q-2)}} = -2\beta \tag{3.20}$$

which gives us the capability to estimate the exact quantity of interest $\mathcal{F}(u)$ by solving the linear equation :

$$\frac{\widetilde{\mathcal{F}}(u) - \mathcal{F}(u_h^q)}{\widetilde{\mathcal{F}}(u) - \mathcal{F}(u_h^{q-2})} = \frac{\widetilde{\mathcal{F}}(u) - \mathcal{F}(u_h^{q-2})}{\widetilde{\mathcal{F}}(u) - \mathcal{F}(u_h^{q-4})} \tag{3.21}$$

and hence

$$\widetilde{\mathcal{F}}(u) = \frac{-\mathcal{F}^2(u_h^{q-2}) + \mathcal{F}(u_h^q)\mathcal{F}(u_h^{q-4})}{\mathcal{F}(u_h^q) + \mathcal{F}(u_h^{q-4}) - 2\mathcal{F}(u_h^{q-2})} \tag{3.22}$$

where $\widetilde{\mathcal{F}}(u)$ is the q-extrapolated estimate for $\mathcal{F}(u)$.

Table 3.6. The extrapolated estimate $\widetilde{\mathcal{F}}(u)$ for Mesh A, B, C, and D using both the plane-wave and wave-band basis functions.

Mesh	plane-wave basis	wave-band basis
A	1.088107	1.088061
B	1.088040	1.088040
C	1.088040	1.088044
D	1.088040	1.088039

As an example, consider the rigid scattering problem and let us employ the modulus of the solution on the surface of the scatterer coinciding with the domain boundary as the quantity of interest, namely $\mathcal{F}(u) = |u(-a, 0)|$. Table 3.6 gives the extrapolated estimate

$\widetilde{\mathcal{F}}(u)$ computed using the plane-wave and wave-band basis functions following the formula given in (3.22).
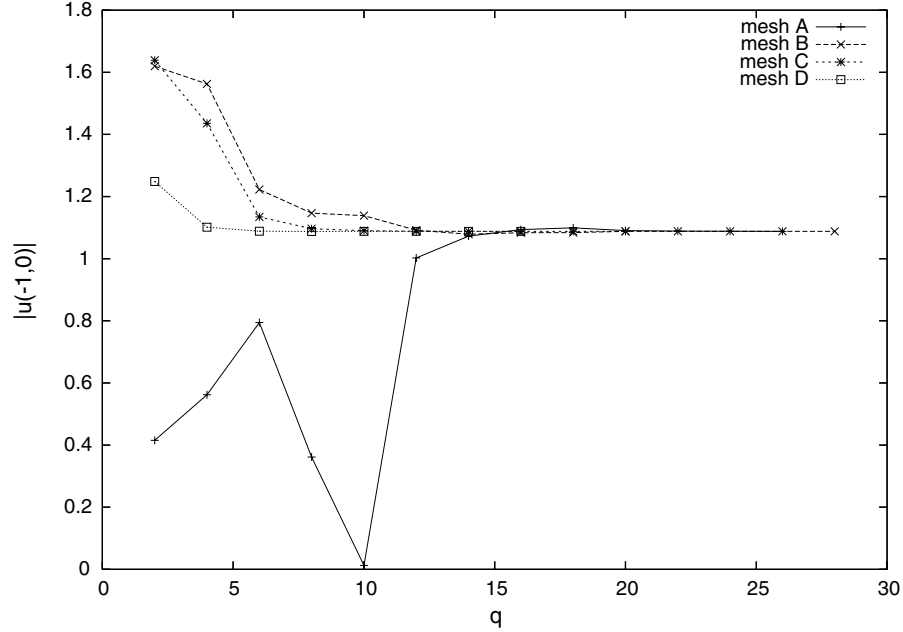
Figure 3.12. Graph of the output $\mathcal{F}(u_h^q) = |u_h^q(-a,0)|$ on Mesh A, B, C, and D using plane-wave basis functions.

Figure 3.12 (resp. Figure 3.13) graphs of the output $\mathcal{F}(u_h^q)$ for the plane-wave (resp. wave-bands) PUM basis versus q. From both figures we can see that the finer mesh reach the asymptotic range faster than the coarser one.

Using the same values of q as in Figures 3.12 and 3.13, we report the exact and estimated quantity of interest for $\mathcal{F}(u_h^{q-4})$ in Table 3.7. We can see that we get very good effectivity indices for all the meshes and for both types of basis functions.
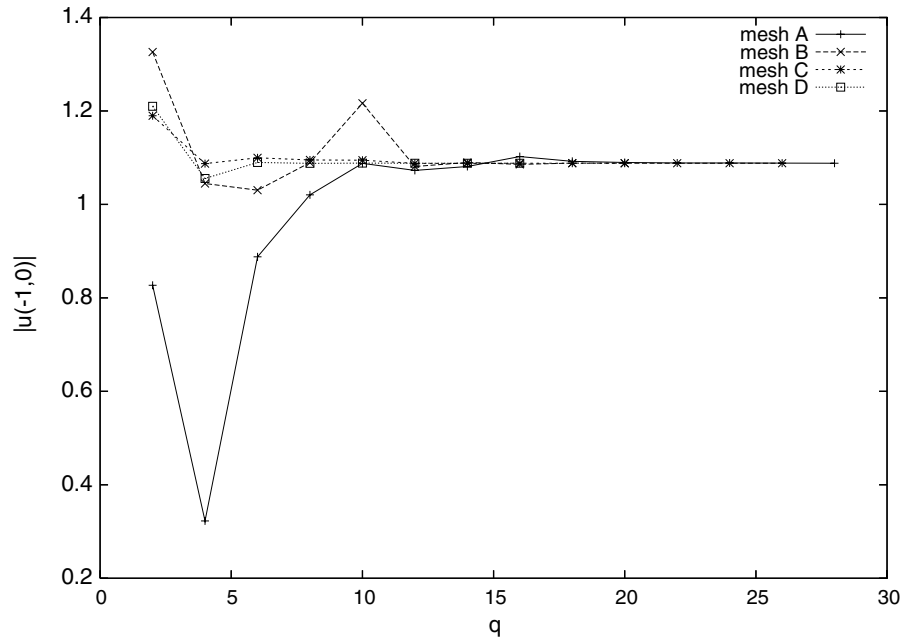
Figure 3.13. Graph of the output $\mathcal{F}(u_h^q) = |u_h^q(-a, 0)|$ on Mesh A, B, C, and D using wave-band basis functions.

Table 3.7. Exact and estimated value of the quantity of interest and its effectivity index for Mesh A, B, C, and D computed using PUM with the plane-wave and wave-band functions.

Mesh	special function	$\dfrac{|\mathcal{F}(u) - \mathcal{F}(u_h^{q-4})|}{\mathcal{F}(u)}$	$\dfrac{|\widetilde{\mathcal{F}}(u) - \mathcal{F}(u_h^{q-4})|}{\widetilde{\mathcal{F}}(u)}$	θ
A	plane-waves	0.0669 %	0.0607 %	0.9073
	wave-bands	0.0493 %	0.0473 %	0.9594
B	plane-waves	0.0014 %	0.0014 %	1.0000
	wave-bands	0.0031 %	0.0083 %	2.6774
C	plane-waves	0.0051 %	0.0051 %	1.0000
	wave-bands	0.0004 %	0.0007 %	1.7500
D	plane-waves	0.0009 %	0.0009 %	1.0000
	wave-bands	0.0027 %	0.0026 %	0.9630

CHAPTER IV

APPLICATIONS OF THE GENERALIZED FINITE ELEMENT METHOD TO THE MULTIPLE SCATTERING PROBLEM

In this section, we will generalize the model problem with one scatterer to the multiple-scattering problem as follows:

Helmholtz problem with Robin boundary condition

$$-\Delta u - k^2 u = 0 \qquad \text{in } \Omega \tag{4.1a}$$

$$\frac{\partial u}{\partial n} = -\frac{\partial u_{inc}}{\partial n} \qquad \text{on } \Gamma_j, \ j = 1, ..., \text{nsca} \tag{4.1b}$$

$$\frac{\partial u}{\partial n} - iku = g_2 \qquad \text{on } \Gamma_0 \tag{4.1c}$$

Here Ω is the domain enclosed by Γ_0, minus the domain enclosed by $\Gamma_j, j = 1, ..., \text{nsca}$; Γ_0 is the exterior boundary and $\Gamma_j, j = 1, 2, ...$ are the boundaries of the scatterers as shown in Figure 4.1, u_{inc} is an analytical expression for the incident wave field, and g_2 a given function. Here g_2 is determined from a known analytical solution of scattering of u_{inc} by one or several circular scatterers.

In this chapter, the main objective is to illustrate the robust exponential convergence characteristics of the GFEM which are also visible for more complex geometries and for various choices of handbook functions as expected by the theory.
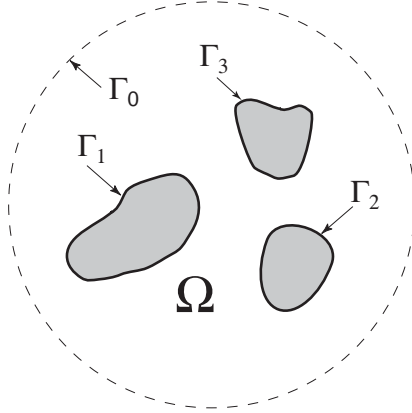
Figure 4.1. Example of a domain Ω that includes three scatterers with boundaries Γ_1, Γ_2, Γ_3, enclosed by an artificial boundary Γ_0.

4.1 Families of handbook functions for Helmholtz equation

The Generalized Finite Element Method offers a high flexibility in the selection of the handbook functions employed in the approximation. For example, for the Helmholtz problem we may employ various families of functions which can be used to obtain a convergent series expansion of homogeneous solutions of the Helmholtz equation in the interior of the domain or near the boundary:

4.1.1 Interior handbook functions

Examples of interior handbook functions are:

1. Plane-wave functions:

$$W_{\text{loc}}^{k;q} = \text{span}\left\{ \exp\left(ik\left(\bar{x}\cos\frac{2\pi n}{q} + \bar{y}\sin\frac{2\pi n}{q} \right) \right), n = 0, ..., q-1 \right\} \qquad (4.2)$$

which is the span of plane waves traveling in the directions $\left(\cos\frac{2\pi n}{q}, \sin\frac{2\pi n}{q} \right)$, $n = 0, ..., q-1$, where $\bar{x} = x - x_i$, $\bar{y} = y - y_i$. We plot the countour of the real part of plane-wave handbook functions with $k = 20$ on a patch $\omega_i^{\Delta h} = (-0.5, 0.5) \times (-0.5, 0.5)$ for $q = 3$ in Figure 4.2.
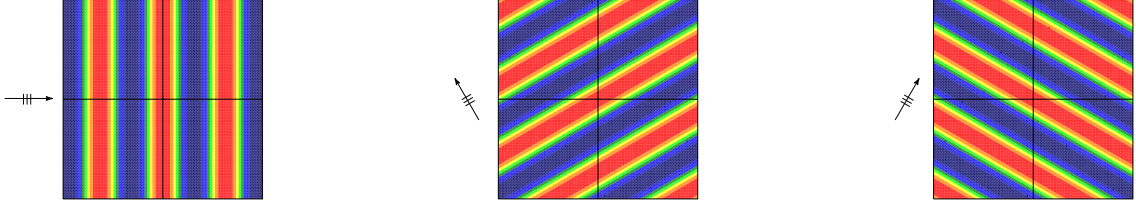
Figure 4.2. Contour plot of the real part of plane-wave handbook functions with $k = 20$ on a patch $\omega_i^{\Delta h} = (-0.5, 0.5) \times (-0.5, 0.5)$ for $q = 3$.

2. Wave-band functions:

$$W_{\text{loc}}^{k;q} = \text{span}\left\{ \int_{\theta_n}^{\theta_{n+1}} e^{(ik(\bar{x}\cos\theta + \bar{y}\sin\theta))} d\theta \quad, n = 0, ..., q - 1, \quad \theta_n = \frac{2\pi n - \pi}{q} \right\} \quad (4.3)$$

which includes all linear combinations of wave bands obtained by superposition of all the plane waves traveling in the directions $(\cos\theta_n, \sin\theta_n)$ to $(\cos\theta_{n+1}, \sin\theta_{n+1})$, $n = 0, ..., q - 1$, $\theta_n = \frac{2\pi n - \pi}{q}$. We plot the countour of the real part of wave-bands handbook functions with $k = 20$ on a patch $\omega_i^{\Delta h} = (-0.5, 0.5) \times (-0.5, 0.5)$ for $q = 3$ in Figure 4.3.
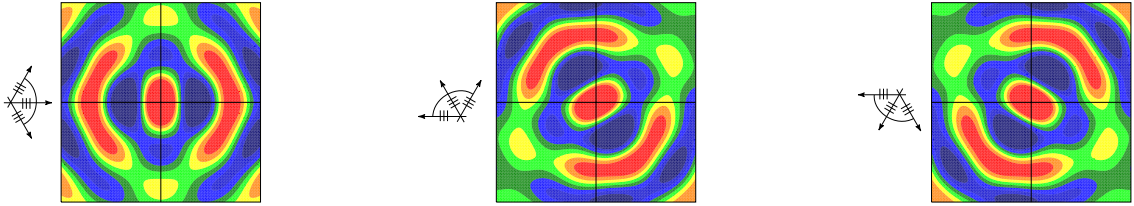
Figure 4.3. Contour plot of the real part of wave-bands handbook functions with $k = 20$ on a patch $\omega_i^{\Delta h} = (-0.5, 0.5) \times (-0.5, 0.5)$ for $q = 3$.

3. Vekua functions:

$$W_{\text{loc}}^{k;q} = \text{span}\left\{ e^{in\psi} J_n(kr) \,, n = 0, ..., q \right\} \quad (4.4)$$

where $r = \sqrt{\bar{x}^2 + \bar{y}^2}$ and $\psi = \tan^{-1}(\bar{y}/\bar{x})$. We plot the countour of the real part of Vekua functions with $k = 20$ on a patch $\omega_i^{\Delta h} = (-0.5, 0.5) \times (-0.5, 0.5)$ for $q = 3$ in

Figure 4.4.
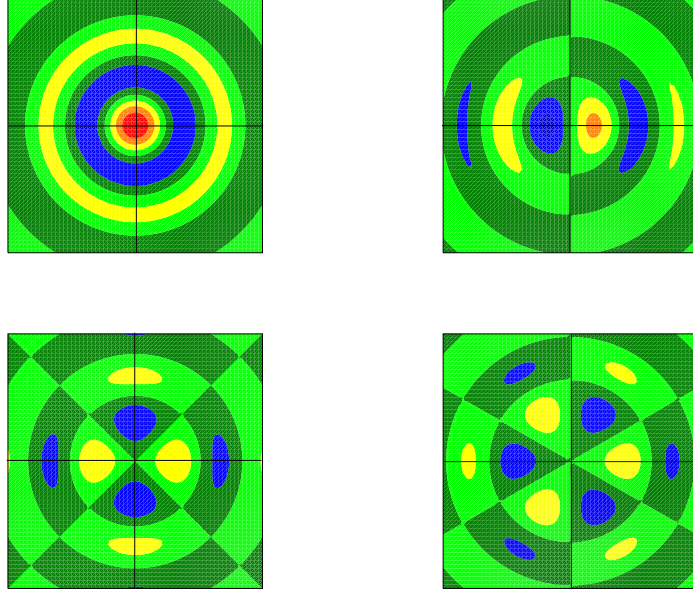
Figure 4.4. Contour plot of the real part of Vekua handbook functions with $k = 20$ on a patch $\omega_i^{\Delta h} = (-0.5, 0.5) \times (-0.5, 0.5)$ for $q = 3$.

4.1.2 Boundary handbook functions

Near the boundary we can employ families of handbook functions which take into account the geometry of the boundary and the imposed boundary condition. For example, for the circular scatterer, the separation of variable in the polar coordinates gives:

$$u(r,\theta) = \sum_{n=0}^{\infty} H_n(kr)(A_n \cos(n\theta) + B_n \sin(n\theta)) \tag{4.5}$$

where $r = \sqrt{x_s^2 + y_s^2}$ and $\psi = \tan^{-1}(y_s/x_s)$, and (x_s, y_s) is the center of the scatterer, and hence we may employ as the handbook functions:

$$W_{\text{loc}}^{k;q} = \text{span}\Big\{H_n(kr)\cos(n\theta)\ , n = 0, ..., q-1\Big\} \oplus \Big\{H_n(kr)\sin(n\theta)\ , n = 1, ..., q-1\Big\} \tag{4.6}$$

which we plotted in Figure 4.5 for the functions around the largest circular scatterer.

In the case of an elliptical scatterer with major axis $2a$ and minor axis $2b$ we have (see
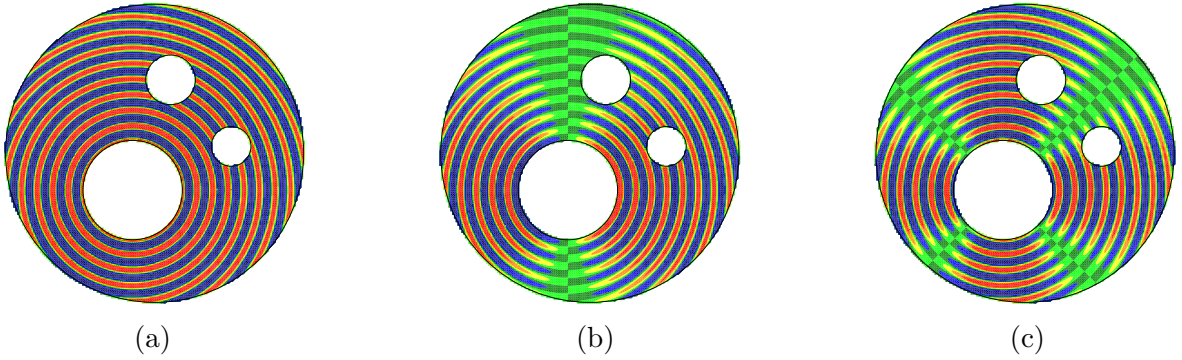
Figure 4.5. Contours of the real part of the circular scatterer functions: a) $H_0(kr)$, b) $H_1(kr)\cos(\theta)$, and c) $H_2(kr)\cos(2\theta)$ for a polar coordinate system around the largest circular scatterer.

Jones [52]):

$$u(s,t) = -2\sum_{n=0}^{\infty}(-i)^n b_n ce_n(t,h)ce_n(\psi,h)Mc_n^{(4)}(s,h)$$

$$-2\sum_{n=1}^{\infty}(-i)^n c_n se_n(t,h)se_n(\psi,h)Ms_n^{(4)}(s,h) \tag{4.7}$$

where (s,t) are the elliptic cylinder coordinates with $x = l\,\cosh s\cos t$, $y = l\,\sinh s\sin t$, $l^2 = s^2 + t^2$, and $h = \frac{1}{4}k^2 l^2$. ψ is the angle of the incident plane wave, and the solution is described using Mathieu functions, where ce_n and se_n are the n-th Mathieu function of the first kind, and Mc_n and Ms_n are the n-th modified Mathieu function of the first kind, and here

$$W_{\text{loc}}^{k;q} = \text{span}\Big\{ce_n(t,h)Mc_n^{(4)}(s,h)\ ,n = 0,...,q\Big\} \oplus \Big\{se_n(t,h)Ms_n^{(4)}(s,h)\ ,n = 1,...,q\Big\} \tag{4.8}$$

Curvilinear scatterers with more general geometry may be approximated locally as circular or elliptical and the above handbook functions can be used in the neighborhood of the approximation of the boundary.

4.2 Application to problem with three circular scatterers

Let us analyze the effect of the choice of handbook functions by comparing their performance in an example of scattering of a plane wave by three circular scatterers with wave number $k = 20$, the incident wave $u_{\text{inc}} = e^{ikx}$, a plane wave in the x-direction, and the truncation radius $R = 2.5$. We will refer to this example as Model Problem II.

REAL PART OF SCATTERED WAVE

Min = -.208E+01 ; Max = 0.204E+01

IMAGINARY PART OF SCATTERED WAVE

Min = -.183E+01 ; Max = 0.205E+01
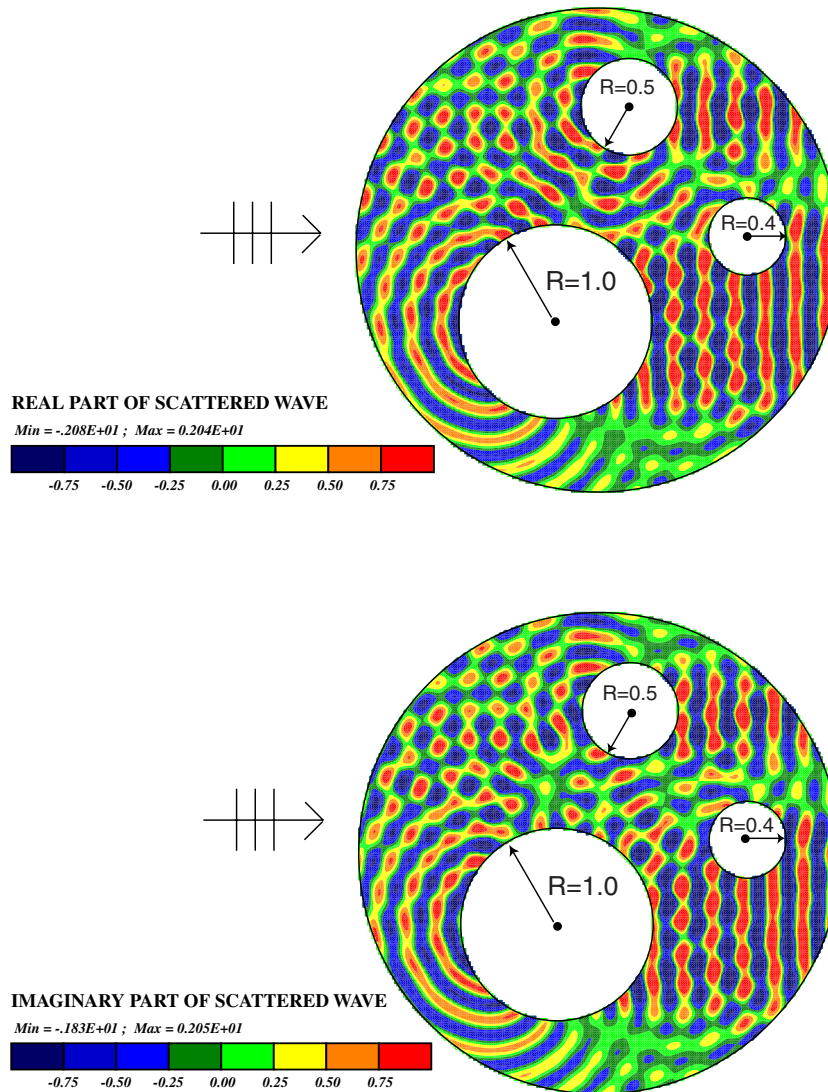
Figure 4.6. Contours of the real and imaginary parts of the scattered field of Model Problem II for $k = 20$ and truncation radius $R = 2.5$.

Once more we will employ the Helmholtz problem with Robin boundary condition exactly as it was used in Chapter II. Following [56] we determined an analytical solution for this problem by employing a collocation method using a large number of terms to achieve very high accuracy. We start by expanding the scattered wave for cylinder j:

$$u_j^{\text{sca}} = \sum_{n=-\infty}^{\infty} B_n^j \ H_n(k|\mathbf{x} - \mathbf{x}_j|) \ e^{in\theta_j} \tag{4.9}$$

and the exciting wave field for scatterer j, which is the wave fields near scatterer j if that particular scatterer is not present:

$$u_j^{\text{exc}} = u_{\text{inc}} + \sum_{m=1, m\neq j}^{\text{nscat}} u_m^{\text{sca}} = \sum_{n=-\infty}^{\infty} A_n^j \ J_n(k|\mathbf{x} - \mathbf{x}_j|) \ e^{in\theta_j} \tag{4.10}$$

By applying the rigid boundary conditions on each scatterer:

$$\frac{\partial}{\partial n} \ u_j^{\text{exc}} = -\frac{\partial}{\partial n} \ u_j^{\text{sca}} \tag{4.11}$$

on (4.10) we can write down the coefficients A_n^j in terms of B_n^j. Using collocation points on the surface of the scatterers, we can solve for the coefficients B_n^j necessary to describe the unknown scattered field. Using this solution, we computed the function g_2 in the Robin boundary condition (4.1c) as in the single scatterer case.

Mesh A   Mesh B   Mesh C

(a)   (b)   (c)
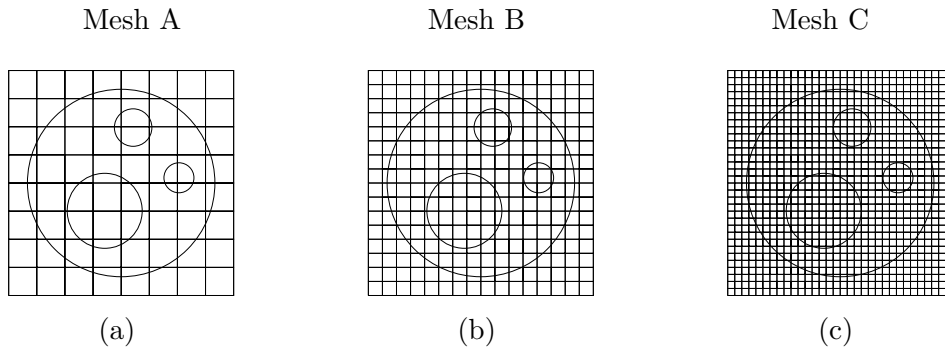
Figure 4.7. Cartesian meshes used in the computation of Model Problem II: (a) Mesh A, $h = 0.75$ (b) Mesh B, $h = 0.375$ (c) Mesh C, $h = 0.1875$.

We employed the GFEM for solving Model Problem II using, once more, $k = 20$. The contour plots of the real and imaginary parts are given in Figure 4.6 and we use the meshes

depicted in Figure 4.7 along with the plane-wave handbook functions to enrich the approximation space. Tables 4.1 to 4.3 and Figures 4.8 to 4.10 report the relative error in the GFEM solution: $\|\nabla(u - u_h^{p,q})\|_{L^2(\Omega)}/\ \|\nabla u\|_{L^2(\Omega)}$ x 100%.

Table 4.1. The values of the percent relative error in the GFEM solution: $\|\nabla(u - u_h^{p,q})\|_{L^2(\Omega)}/\|\nabla u\|_{L^2(\Omega)} \times 100\%$ for Mesh A. The number between parentheses is the number of degrees-of-freedom.

p	$q = 0$	$q = 1$	$q = 3$	$q = 5$	$q = 7$	$q = 9$	$q = 11$	$q = 13$	$q = 15$
1	100.9069	89.9330	83.6337	72.6151	48.7010	43.6616	24.2990	58.6649	11.5272
	(69)	(207)	(483)	(759)	(1035)	(1311)	(1587)	(1863)	(2139)
2	123.0157	93.7137	79.2374	76.9477	46.1729	37.0732	16.1596	12.8196	5.3477
	(238)	(376)	(652)	(928)	(1204)	(1480)	(1756)	(2032)	(2308)
3	117.7788	85.1494	84.7698	70.2853	37.1585	26.3079	6.8508	4.6243	3.3525
	(507)	(645)	(921)	(1197)	(1473)	(1749)	(2025)	(2301)	(2577)
4	134.5831	96.9113	79.1913	66.3792	17.7999	6.8464	4.8491	3.6131	2.7103
	(876)	(1014)	(1290)	(1566)	(1842)	(2118)	(2394)	(2670)	(2946)
5	167.0997	86.1170	70.2640	45.3099	9.1474	4.9322	3.6698	2.7621	2.1531
	(1345)	(1483)	(1759)	(2035)	(2311)	(2587)	(2863)	(3139)	(3145)

We can see that similarly as in Model Problem I (the scattering of plane wave by circular rigid scatterer in Section 2.3), we have the exponential q-convergence for all the meshes and for various p. We note that for Mesh A for $p = 1$ and $p = 2$, the asymptotic rate for q-convergence has not been reached (see Figure 4.8) which signals that the pollution effect still dominates the results, while for $p = 3$ to $p = 5$ the exponential rate of convergence is observed with $\alpha \approx 1/6$. The behavior for $p = 1$ and $p = 2$ was also observed on Model Problem I and it shows that the mesh size h is not sufficiently small and the employed qs are not high enough to eliminate the pollution effect.

The q-convergence are also observed for Mesh B and Mesh C, where we have for Mesh B the rate $\alpha \approx 1/3$ and for Mesh C the rate is $\alpha \approx 2/3$. Note that α increases as the mesh is refined because the solution becomes smoother relative to the mesh. From Figure 4.10

Table 4.2. The values of the percent relative error in the GFEM solution: $\|\nabla(u - u_h^{p,q})\|_{L^2(\Omega)}/\|\nabla u\|_{L^2(\Omega)} \times 100\%$ for Mesh B. The number between parentheses is the number of degrees-of-freedom.

p	$q = 0$	$q = 1$	$q = 3$	$q = 5$	$q = 7$	$q = 9$	$q = 11$	$q = 13$	$q = 15$
1	100.4822	93.4730	63.1929	8.1342	1.9420	1.1004	0.5914	0.2730	0.1385
	(188)	(564)	(1316)	(2068)	(2820)	(3572)	(4324)	(5076)	(5828)
2	176.9614	93.9628	54.3340	5.6670	1.5557	0.9529	0.5318	0.2417	0.1187
	(679)	(1055)	(1807)	(2559)	(3311)	(4063)	(4815)	(5567)	(6319)
3	163.4074	79.0044	38.7852	2.8590	1.0096	0.6615	0.3995	0.1959	0.0983
	(1472)	(1848)	(2600)	(3352)	(4104)	(4856)	(5608)	(6360)	(7112)
4	64.8655	39.5697	12.1532	1.2631	0.5669	0.3808	0.2513	0.1420	0.0760
	(2567)	(2943)	(3695)	(4447)	(5199)	(5951)	(6703)	(7455)	(8207)
5	15.6809	8.3114	2.7103	0.5096	0.3031	0.1941	0.1355	0.0889	0.0537
	(3964)	(4340)	(5092)	(5844)	(6596)	(7348)	(8100)	(8854)	(9604)

Table 4.3. The values of the percent relative error in the GFEM solution: $\|\nabla(u - u_h^{p,q})\|_{L^2(\Omega)}/\|\nabla u\|_{L^2(\Omega)} \times 100\%$ for Mesh C. The number between parentheses is the number of degrees-of-freedom.

p	$q = 0$	$q = 1$	$q = 3$	$q = 5$	$q = 7$	$q = 9$	$q = 11$
1	149.3867	92.9073	12.7460	0.4005	0.0588	0.0120	0.0034
	(605)	(1815)	(4235)	(6655)	(9075)	(11495)	(13915)
2	131.6172	67.8087	2.8034	0.2093	0.0394	0.0092	0.0027
	(2248)	(3548)	(5878)	(8298)	(10718)	(13138)	(15558)
3	20.1521	10.8710	0.6482	0.1135	0.0193	0.0059	0.0017
	(4927)	(6137)	(8557)	(10977)	(13397)	(15817)	(18237)
4	2.9177	1.3949	0.1402	0.0245	0.0092	0.0029	0.0009
	(8642)	(9852)	(12272)	(14692)	(17112)	(19532)	(21952)
5	0.5246	0.2420	0.0262	0.0058	0.0028	0.0012	0.0009
	(13393)	(14603)	(17023)	(19443)	(21863)	(24283)	(26702))

we can see that for $p = 5$ between $q = 9$ and $q = 11$ the asymptotic rate of convergence could not be sustained. This is most likely due to the roundoff errors.

Let us also report corresponding results computed using the wave-band handbook func-

Figure 4.8. q-convergence of the relative error of the GFEM solution $u_h^{p,q}$ for Mesh A versus q, for $p = 1, ..., 5$ using plane-wave handbook functions. Note that for this mesh the pollution is clearly visible for $p = 1$ and 2.

Figure 4.9. q-convergence of the relative error of the GFEM solution $u_h^{p,q}$ for Mesh B versus q, for $p = 1, ..., 5$ using plane-wave handbook functions.
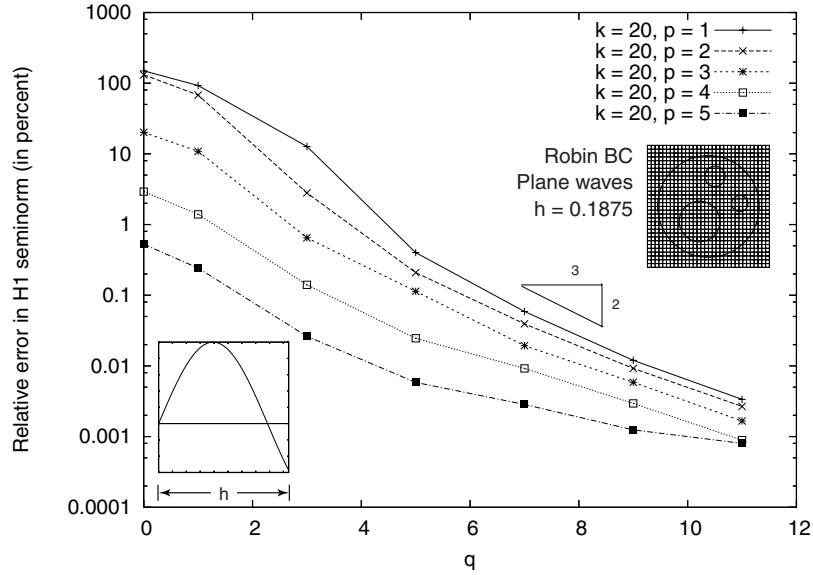
Figure 4.10. q-convergence of the relative error of the GFEM solution $u_h^{p,q}$ for Mesh C versus q, for $p = 1, ..., 5$ using plane-wave handbook functions.

tions given in (4.3). Here we report the computations on Mesh B using $p = 1, .., 5$ and various q and we tabulate the results in Table 4.4.

Table 4.4. The values of the percent relative error in the GFEM solution: $\|\nabla(u - u_h^{p,q})\|_{L^2(\Omega)} / \|\nabla u\|_{L^2(\Omega)} \times 100\%$ for Mesh B using wave-bands handbook functions. The number between parentheses is the number of degrees-of-freedom.

p	$q = 0$	$q = 1$	$q = 3$	$q = 5$	$q = 7$	$q = 9$	$q = 11$	$q = 13$	$q = 15$
1	100.4822	108.1900	183.4246	16.4246	3.4544	1.2504	0.6922	0.3253	0.1623
	(188)	(564)	(1316)	(2068)	(2820)	(3572)	(4324)	(5076)	(5828)
2	176.9614	188.1957	149.0925	9.8767	2.4494	1.0440	0.6104	0.2933	0.1329
	(679)	(1055)	(1807)	(2559)	(3311)	(4063)	(4815)	(5567)	(6319)
3	163.4074	154.4796	75.6858	6.2727	1.5354	0.7402	0.4543	0.2362	0.1117
	(1472)	(1848)	(2600)	(3352)	(4104)	(4856)	(5608)	(6360)	(7112)
4	64.8655	47.4905	15.2265	2.2152	0.7400	0.4177	0.2822	0.1640	0.0886
	(2567)	(2943)	(3695)	(4447)	(5199)	(5951)	(6703)	(7455)	(8207)
5	15.6809	13.5976	4.7863	0.9758	0.3393	0.2128	0.1478	0.1002	0.0604
	(3964)	(4340)	(5092)	(5844)	(6596)	(7348)	(8100)	(8854)	(9604)

Figure 4.11. q-convergence of the relative error of the GFEM solution $u_h^{p,q}$ for Mesh B versus q, for $p = 1, ..., 5$ using wave-bands handbook functions.

Figure 4.11 plots the q-convergence of relative error of the GFEM solution for Mesh B using the wave-band handbook functions for $p = 1, ..., 5$. Once more the rate of convergence $\alpha \approx 1/3$ is achieved, similarly with the computations performed using plane-wave handbook functions. This can be seen clearly in Figure 4.12 where we plot q-convergence for both choices of handbook functions; notice that for after the pollution has ended for high enough q, the graphs practically overlap.

Finally we repeat the computations on Mesh B using the Vekua handbook functions defined in (4.4), and we tabulate the results in Table 4.5. Figure 4.13 shows the q-convergence, and once more we observe that the rate of convergence is $\alpha \approx 1/3$ From Figure 4.14 we can see that, after the pollution has ended, the convergence curves using Vekua and plane-wave handbook functions are almost indistinguishable.

These results clearly show that the GFEM using various interior handbook functions have similar convergence and accuracy. It follows that the selection should be dictated by
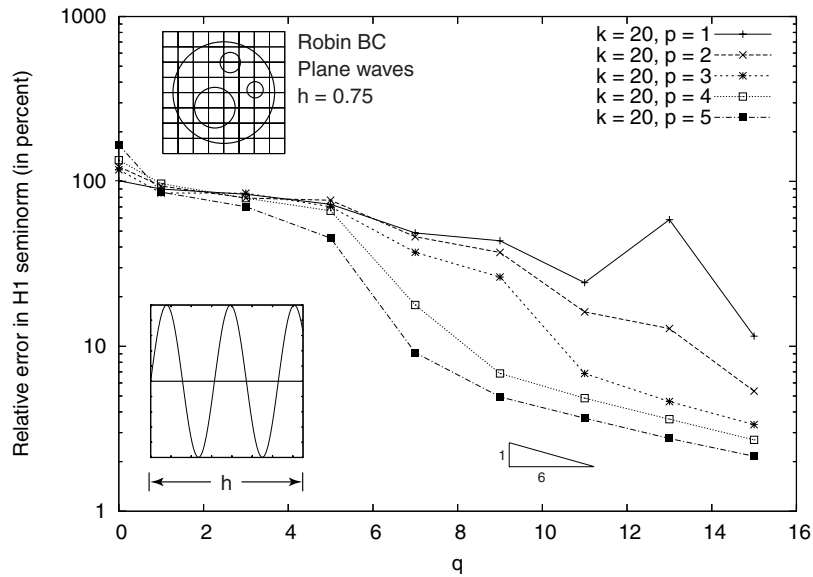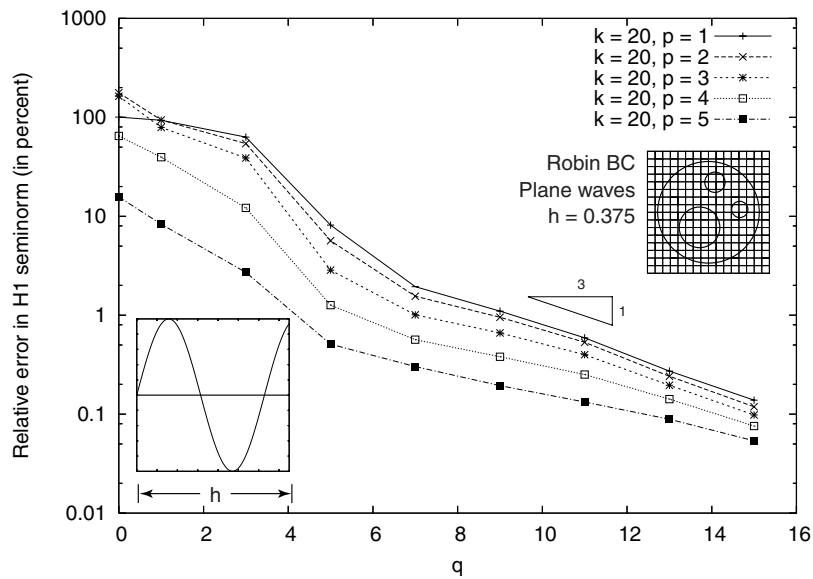
Figure 4.12. q-convergence of the relative error of the GFEM solution $u_h^{p,q}$ for Mesh B versus q, for $p = 1, ..., 5$; comparison of plane-wave and wave-bands handbook functions. Note that after the pollution has ended the asymptotic behavior of the error is very similar for the two choices of handbook functions.

Table 4.5. The values of the percent relative error in the GFEM solution: $\|\nabla(u - u_h^{p,q})\|_{L^2(\Omega)}/\|\nabla u\|_{L^2(\Omega)} \times 100\%$ for Mesh B using Vekua handbook functions. The number between parentheses is the number of degrees-of-freedom.

p	$q = 0$	$q = 1$	$q = 3$	$q = 5$	$q = 7$	$q = 9$	$q = 11$	$q = 13$	$q = 15$
1	100.4822	224.1210	140.5306	5.9537	1.7802	0.9159	0.4661	0.2138	0.1110
	(188)	(752)	(1504)	(2256)	(3008)	(3760)	(4512)	(5264)	(6016)
2	176.9614	189.6900	56.4671	4.9769	1.4127	0.7948	0.4175	0.1861	0.0952
	(679)	(1243)	(1995)	(2747)	(3499)	(4251)	(5003)	(5755)	(6507)
3	163.4074	123.9561	22.8366	3.3877	0.9320	0.5769	0.3264	0.1557	0.0780
	(1472)	(2036)	(2788)	(3540)	(4292)	(5044)	(5796)	(6548)	(7300)
4	64.8655	35.0798	3.9431	1.0781	0.5196	0.3472	0.2206	0.1174	0.0584
	(2567)	(3131)	(3883)	(4635)	(5387)	(6139)	(3894)	(7673)	(5395)
5	15.6809	6.5875	1.4530	0.4584	0.2597	0.1786	0.1208	0.0760	0.0438
	(3964)	(4528)	(5280)	(6032)	(6784)	(7536)	(8288)	(9040)	(9792)

Figure 4.13. q-convergence of the relative error of the GFEM solution $u_h^{p,q}$ for Mesh B versus q, for $p = 1, ..., 5$ using Vekua handbook functions.

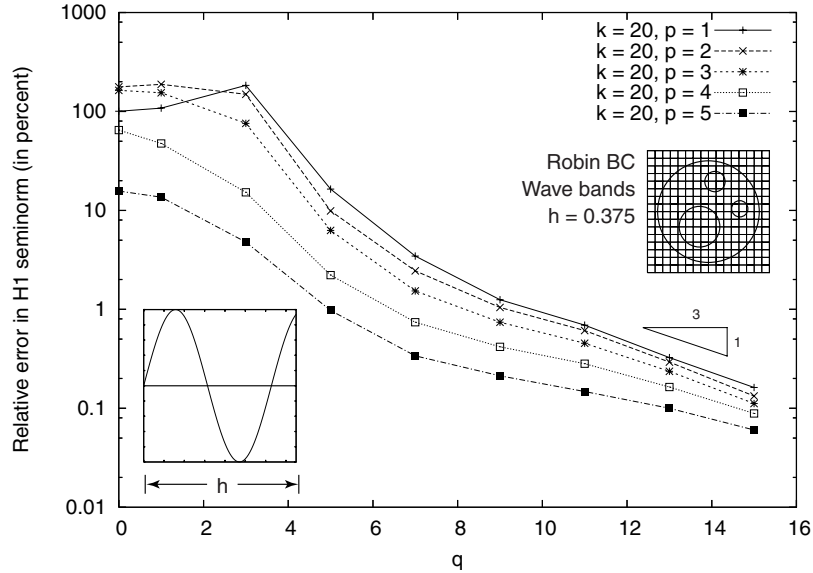factors other than accuracy such as the ease of implementation, and the computational cost. For example, the computation of stiffness matrices for the GFEM using the wave-band handbook functions requires the evaluation of 4-dimensional integrals by numerical integration, which is very costly. Although several semi-analytical integration methods are proposed, e.g. by Ladevèze, Rouch, and Riou [25–27], they require the use of rectangular integration domain and hence are not applicable in the more general setting of the method considered here.

Figure 4.15 compares the computational cost of the plane-wave and the Vekua handbook functions using Mesh B and $p = 3$. The figure plots the total time taken to integrate, assemble and solve the stiffness matrix for various q, using a Dell computer with Intel Xeon 3.2 GHz and 3.0 GB RAM. We can see that the plane-wave and Vekua handbook functions take an almost identical processing time, while the wave-band handbook functions perform poorly in this category. However, we note that the computation of Bessel functions in Vekua
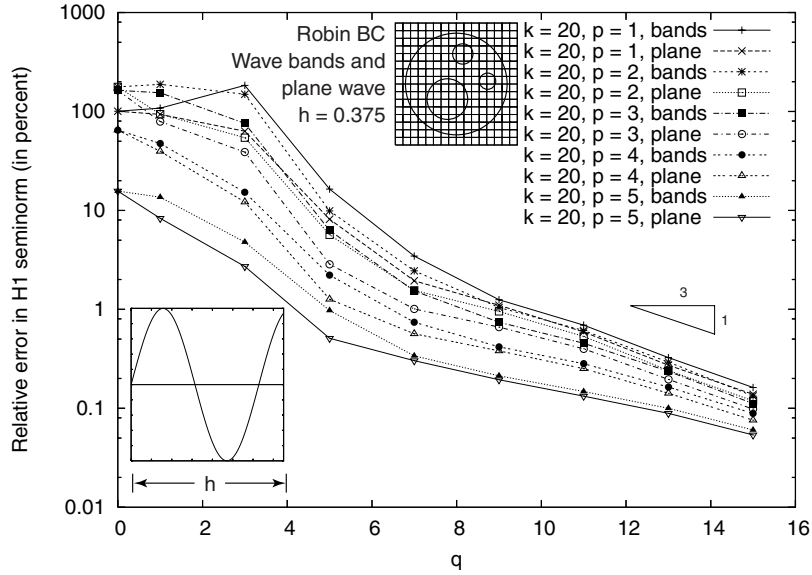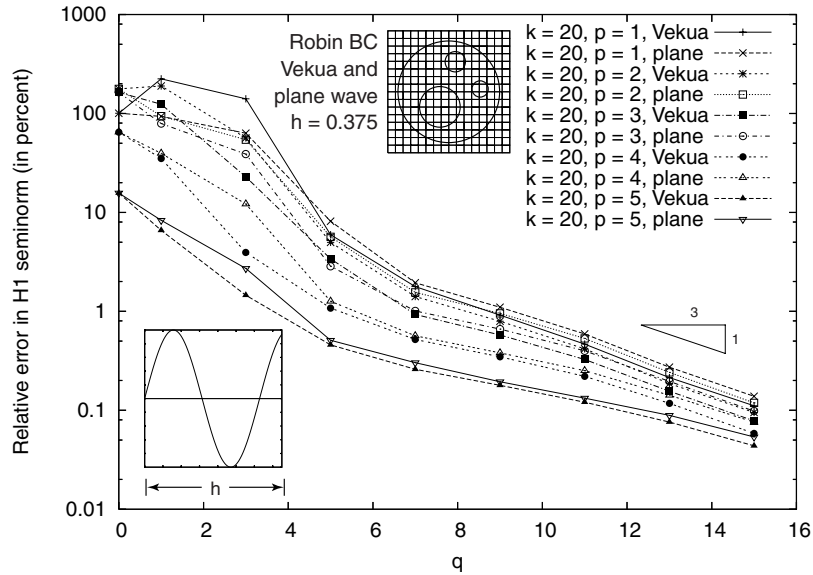
Figure 4.14. q-convergence of the relative error of the GFEM solution $u_h^{p,q}$ for Mesh B versus q, for $p = 1, ..., 5$; comparison of plane-wave and Vekua handbook functions. Note that the main differences of the convergence results for the plane-wave and Vekua functions are in the pre-asymptotic range.
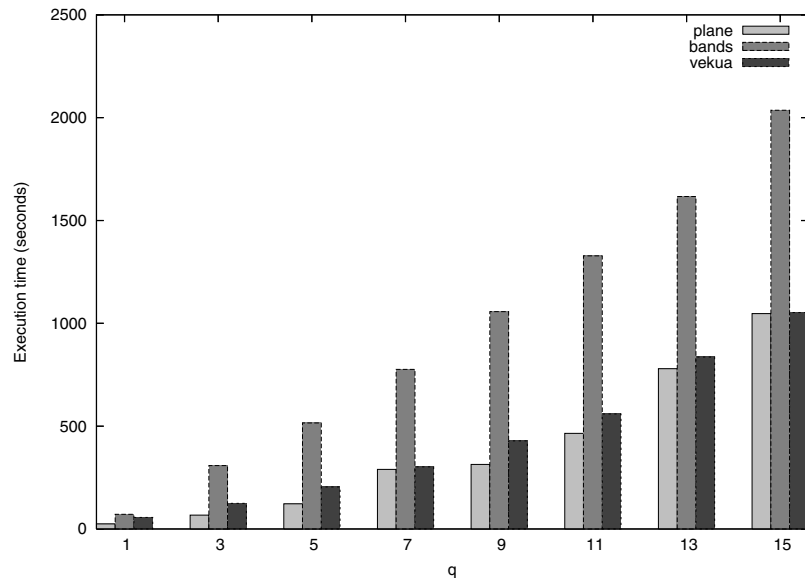
Figure 4.15. Comparison of total time required to integrate, assemble and solve stiffness matrix for plane-wave, wave-band and Vekua handbook functions for various q. Here we use Mesh B and $p = 3$.

handbook function is slightly more expensive than the computation of the trigonometric function for the plane waves and it is not as readily available. Hence, among the three families of interior handbook functions addressed here, the plane-wave handbook functions are preferable.

Remark 10: To underline the flexibility of the GFEM with respect to the mesh type we report computations for Model Problem II performed on the series of meshes that conform to one of the scatterers, as shown in Figure 4.16.

Mesh A   Mesh B   Mesh C

(a)   (b)   (c)
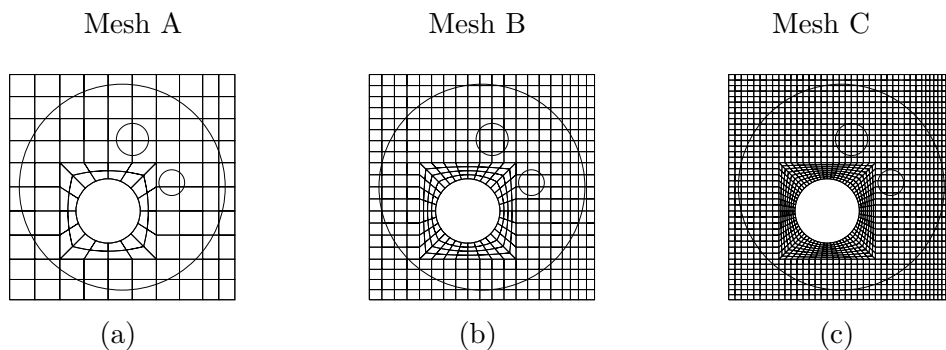
Figure 4.16. The semi-conforming meshes used in Model Problem II computations to highlight the GFEM flexibility with respect to mesh types.

Figure 4.17 depicts the q-convergence graphs for $p = 1, 2$. One more we see convergence characteristics of the method reported earlier, namely for Mesh A, the asymptotic rate of convergence has not been reached for $q \leq 17$, and the rate of convergence improves as the mesh is refined.
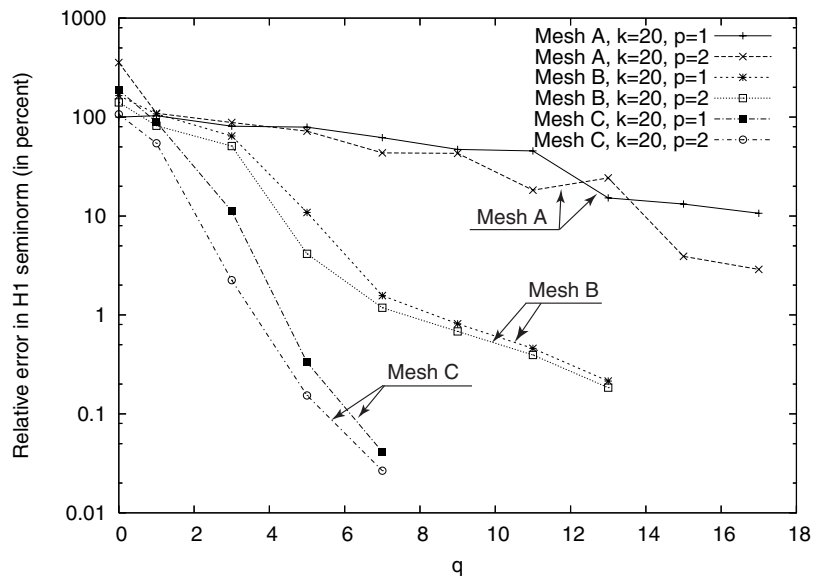
Figure 4.17. q-convergence of the relative error of the GFEM solution $u_h^{p,q}$ for Mesh A, B, and C shown in Figure 4.16 versus q, for $p = 1, 2$.

CHAPTER V

ANALYSIS OF SOMMERFELD AND BAYLISS-TURKEL BOUNDARY CONDITIONS

5.1 Formulation of the absorbing boundary conditions

In Chapters II, III, and IV we employed the Helmholtz problem with the Robin condition:

$$\frac{\partial u}{\partial n} - iku = g_2 \qquad \text{on } \Gamma_0 \tag{5.1}$$

where Γ_0 is the outer boundary of Ω, and g_2 is obtained by evaluating the left-hand side for a known exact solution. The objective was to analyze the error coming from the GFEM approximation of u over the finite domain Ω without having to address the error due to an artificial truncation boundary condition. We will now address the more realistic case where the GFEM computation is done using an artificial truncation boundary condition on Γ_0. Below we will always assume that $\Gamma_0 = \{\mathbf{x} \in \mathbb{R}^2 \,\big|\, |\mathbf{x} - \mathbf{x}_0| = R\}$ is a circle of radius R with R sufficiently big to encompass the scatterers of interest.

The simplest possible artificial truncation boundary is obtained by letting $g_2 = 0$ to obtain the Sommerfeld boundary condition on Γ_0. Other truncation boundary conditions may be obtained in various ways; see e.g. Keller and Givoli [8] and Grote and Keller [9]. Here we will employ the boundary conditions proposed by Bayliss, Gunzburger, and Turkel [6, 7] which are often used in practice.

We have:

1. Sommerfeld condition applied at truncation boundary (SOM):

$$\frac{\partial u}{\partial r} - iku = 0 \qquad \text{on } \Gamma_0 \tag{5.2}$$

2. Bayliss-Turkel 1 (BT1):

$$\frac{\partial u}{\partial r} - \left(ik - \frac{1}{2R}\right)u = 0 \qquad \text{on } \Gamma_0 \tag{5.3}$$

3. Bayliss-Turkel 2 (BT2):

$$\frac{\partial u}{\partial r} - \frac{1}{2\left(ik - 1/R\right)}\left(-2k^2 - \frac{3ik}{R} + \frac{3}{4R^2} + \frac{1}{R^2}\frac{\partial}{\partial \theta^2}\right)u = 0 \qquad \text{on } \Gamma_0 \tag{5.4}$$

The artificial truncation boundary introduces additional error in the computation, which depends on: 1) Its formulation; 2) Radius of the truncation boundary; 3) Wave number k. We will first analyze the error due to the three types of boundary conditions for Model Problem I, for which we can obtain exact solution of the Helmholtz problem with boundary condition (5.2), (5.3), or (5.4). Using separation of variables, we have:

$$u_{EX}^{R,BC}(r,\theta) = \sum_{n=0}^{\infty} \left(H_n^{(1)}(kr) + F_n H_n^{(2)}(kr)\right)A_n\cos(n\theta) \tag{5.5}$$

where $u_{EX}^{R,BC}$ denotes the exact solution of the Helmholtz Model Problem I with truncation radius R and (4.1c) replaced by BC = SOM, BT1, or BT2. The coefficients F_n, A_n are given in Table 5.1.

The error due to the artificial boundary condition in the quantity $\mathcal{F}(u)$ is measured by:

$$e_{\mathcal{F}} = \frac{\left|\left|\left|\mathcal{F}\left(u_{EX}^{\infty} - u_{EX}^{R,BC}\right)\right|\right|\right|}{\left|\left|\left|\mathcal{F}\left(u_{EX}^{\infty}\right)\right|\right|\right|} \tag{5.6}$$

where u_{EX}^{∞} denotes the exact solution for the problem set in the infinite domain, and $|||\cdot|||$ is the norm employed to measure the error. Figures 5.1 - 5.3 show the convergence of $e_{\mathcal{F}}$ in the case that $\mathcal{F}(u) = u(-1,0)$, and $|||\cdot|||$ is the modulus, namely:

$$e_{u(-1.0)} = \frac{\left|\left(u_{EX}^{\infty} - u_{EX}^{R,BC}\right)(-1,0)\right|}{\left|u_{EX}^{\infty}(-1,0)\right|} \times 100\% \tag{5.7}$$

versus R for the Sommerfeld, Bayliss-Turkel 1, and Bayliss-Turkel 2 boundary conditions for $k = 10, 20$, and 30. It can be clearly seen that asymptotically we have algebraic convergence,

Table 5.1. Analytical expression of F_n and A_n corresponding to boundary condition BC on Γ_0.

BC	Condition on $r = R$	F_n
SOM	$\dfrac{\partial u}{\partial r} - iku = 0$	$-\dfrac{H_n^{(1)'}(kR) - iH_n^{(1)}(kR)}{H_n^{(2)'}(kR) - iH_n^{(2)}(kR)}$
BT1	$\dfrac{\partial u}{\partial r} - \left(ik - \dfrac{1}{2R} \right) u = 0$	$-\dfrac{kH_n^{(1)'}(kR) - (ik - \frac{1}{2R})H_n^{(1)}(kR)}{kH_n^{(2)'}(kR) - (ik - \frac{1}{2R})H_n^{(2)}(kR)}$
BT2	$\dfrac{\partial u}{\partial r} - \mathcal{C}_1 \left(\mathcal{C}_2 + \dfrac{1}{R^2}\dfrac{\partial}{\partial \theta^2} \right) u = 0$	$-\dfrac{kH_n^{(1)'}(kR) - \mathcal{C}_1(\mathcal{C}_2 + \frac{n^2}{R^2})H_n^{(1)}(kR)}{kH_n^{(2)'}(kR) - \mathcal{C}_1(\mathcal{C}_2 + \frac{n^2}{R^2})H_n^{(2)}(kR)}$
	with $\mathcal{C}_1 = \dfrac{1}{2\left(ik - 1/R \right)}$;	$A_n = -\epsilon_n i^n \dfrac{J_n'(ka)}{H_n^{(1)'}(ka) + F_n H_n^{(2)'}(ka)}$
	$\mathcal{C}_2 = -2k^2 - \dfrac{3ik}{R} + \dfrac{3}{4R^2}$	

namely

$$|e_{u(-1.0)}| \approx \mathcal{C}R^\beta \tag{5.8}$$

where $\beta = 2$ for Sommerfeld and Bayliss-Turkel 1, and $\beta = 4$ for Bayliss-Turkel 2, nevertheless the asymptotic behavior may be reached for $R > \bar{R}(k)$, where $\bar{R}(k)$ can be rather big for the Sommerfeld and Bayliss-Turkel 1 boundary conditions.

Let us introduce an estimator for $e_{\mathcal{F}}$, namely:

$$\mathcal{E}_\mathcal{F}(d) = \frac{\left|\left|\left| \mathcal{F}\left(u_{\text{EX}}^{R+d,BT2} - u_{\text{EX}}^{R,BC} \right) \right|\right|\right|}{\left|\left|\left| \mathcal{F}\left(u_{\text{EX}}^{R+d,BT2} \right) \right|\right|\right|} \tag{5.9}$$

where $u_{\text{EX}}^{R+d,BT2}$ is the exact solution for an extended domain where Γ_0 is replaced by $\bar{\Gamma}_0 = \{\mathbf{x} \in \mathbb{R}^2 \big| |\mathbf{x} - \mathbf{x}_0| = R + d\}$ computed using Bayliss-Turkel 2 boundary condition. Let
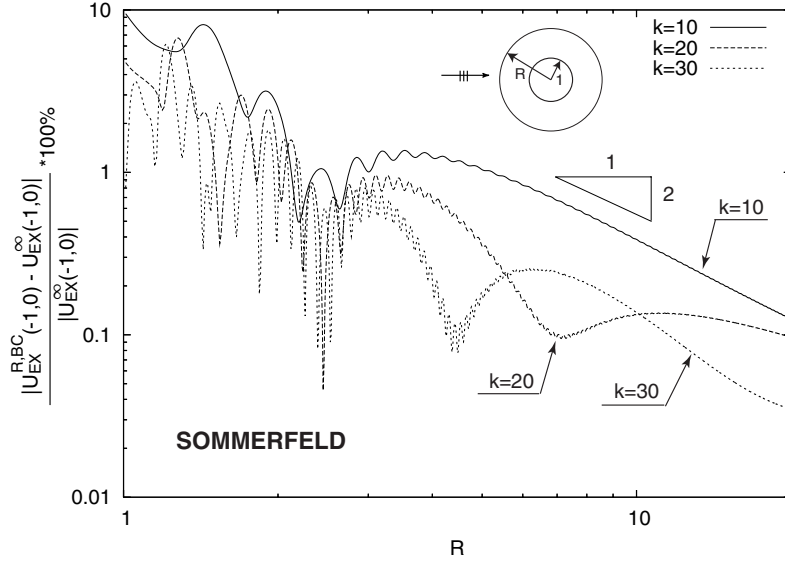
Figure 5.1. Plot of $e_{u(-1.0)}$ for $k = 10, 20, 30$ using the Sommerfeld boundary condition on Γ_0.

Figure 5.2. Plot of $e_{u(-1.0)}$ for $k = 10, 20, 30$ using Bayliss-Turkel 1 boundary condition on Γ_0.

us now analyze the effectivity of this estimator for $\mathcal{F}(u) = u(-1, 0)$. In this case we have:

$$\mathcal{E}_{u(-1,0)}(d) = \frac{\left| \left(u_{\text{EX}}^{R+d,BT2} - u_{\text{EX}}^{R,BC} \right)(-1,0) \right|}{\left| u_{\text{EX}}^{R+d,BT2}(-1,0) \right|} \times 100\% \qquad (5.10)$$
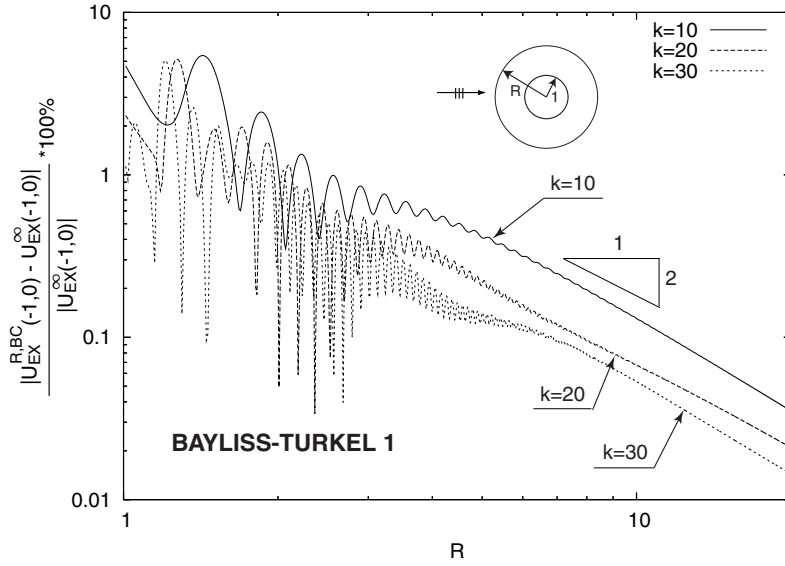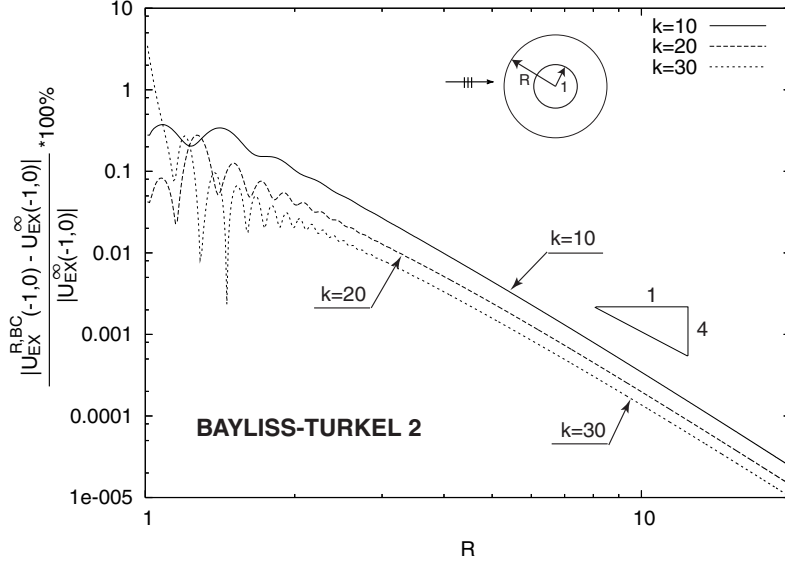
Figure 5.3. Plot of $e_{u(-1.0)}$ for $k = 10, 20, 30$ using Bayliss-Turkel 2 boundary condition on Γ_0.

and in Figures 5.4-5.6 we plotted the effectivity index

$$\theta^{\text{EX}}_{u(-1,0)} = \frac{\mathcal{E}_{u(-1,0)}(d)}{e_{u(-1,0)}} = \frac{\left|\left(u^{R+d,BT2}_{\text{EX}} - u^{R,BC}_{\text{EX}}\right)(-1,0)\right| \Big/ \left|u^{R+d,BT2}_{\text{EX}}(-1,0)\right|}{\left|\left(u^{\infty}_{\text{EX}} - u^{R,BC}_{\text{EX}}\right)(-1,0)\right| \Big/ \left|u^{\infty}_{\text{EX}}(-1,0)\right|} \tag{5.11}$$

respectively for BC = SOM, BT1, BT2 versus d/R using $k = 20$. We see that the effectivity index is close to one in all the cases and converges to one as d/R is increased.

In practice we have to employ a computed approximation of $u^{R,BC}_{\text{EX}}$, namely $u^{R,BC}_{h;p,q}$ and we will denote by $e^{h;p,q}_{\mathcal{F}}, \mathcal{E}^{h;p,q}_{\mathcal{F}}(d), \theta^{h;p,q}_{\mathcal{F}}$ the corresponding relative error, its estimator and its effectivity index. Hence for the case $\mathcal{F}(u) = u(-1,0)$ we have:

$$\theta^{h;p,q}_{u(-1,0)} = \frac{\mathcal{E}_{u(-1,0)}(d)}{e_{u(-1,0)}} = \frac{\left|\left(u^{R+d,BT2}_{h;p,q} - u^{R,BC}_{h;p,q}\right)(-1,0)\right| \Big/ \left|u^{R+d,BT2}_{h;p,q}(-1,0)\right|}{\left|\left(u^{\infty}_{\text{EX}} - u^{R,BC}_{h;p,q}\right)(-1,0)\right| \Big/ \left|u^{\infty}_{\text{EX}}(-1,0)\right|} \tag{5.12}$$

Table 5.2 compares the effectivity indices $\theta^{\text{EX}}_{u(-1,0)}$ and $\theta^{h;p,q}_{u(-1,0)}$ corresponding to $u^{R,BC}_{\text{EX}}$ and $u^{R,BC}_{h;p,q}$ respectively for $d/R = 1.00, 1.25$ and $R = 1.5, 2.5$ with BC = SOM, BT1, BT2. The computations for $u^{R,BC}_{h;p,q}$ use $p = 3$, plane-wave handbook functions with $q = 13$, $h = 0.3125$ for $R = 1.5$ and $h = 0.375$ for $R = 2.5$. The $(h; p, q)$ parameters for computations
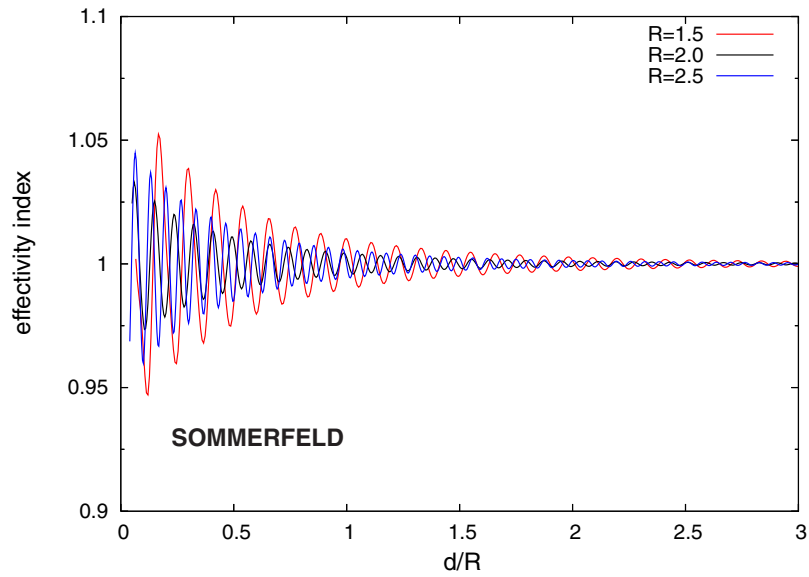
Figure 5.4. Effectivity index $\theta^{\text{EX}}_{u(-1,0)}$ for $k = 20$ using Sommerfeld boundary condition on Γ_0 with $R = 1.5, 2.0, 2.5$.
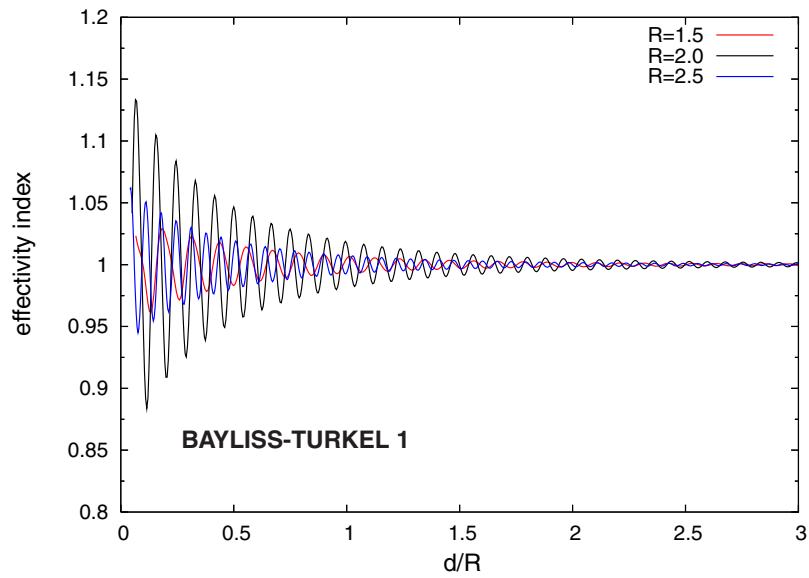
Figure 5.5. Effectivity index $\theta^{\text{EX}}_{u(-1,0)}$ for $k = 20$ using Bayliss-Turkel 1 boundary condition on Γ_0 with $R = 1.5, 2.0, 2.5$.
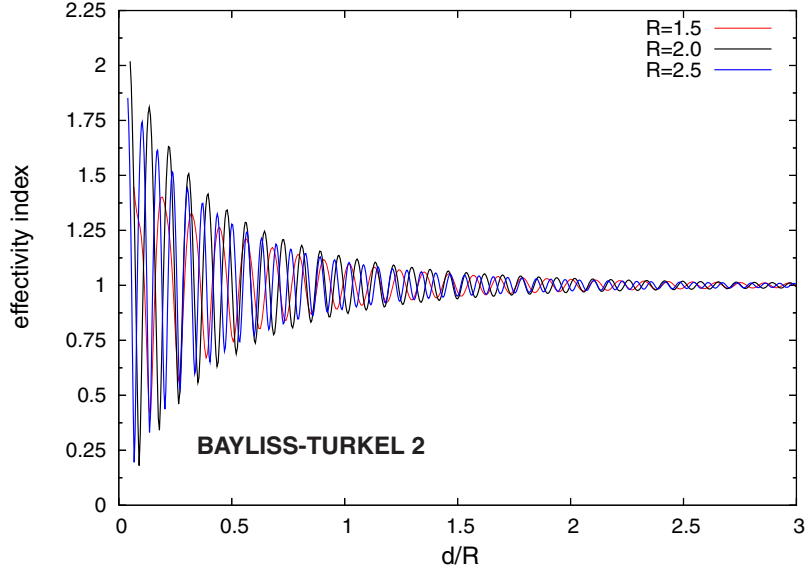
Figure 5.6. Effectivity index $\theta^{\text{EX}}_{u(-1,0)}$ for $k = 20$ using Bayliss-Turkel 2 boundary condition on Γ_0 with $R = 1.5, 2.0, 2.5$.

of $u^{R+d,BT2}_{h;p,q}$ is reported on Table 5.2 where again we use the plane-wave handbook functions. We see that with the exception of one case for which the error is very small at the right lowest corner of the table, the other numbers are rather close. The implicit assumption in the above approach is that the error to the $(h; p, q)$ GFEM approximation is negligible relative to the error due to the employed artificial boundary condition. When this assumption is satisfied we expect to get a reliable estimator for the error in the artificial truncation boundary condition.

Figures 5.7 and 5.8 compare the q-convergence graphs for the errors $e^{h;p,q}_{u(-1,0)}$ and its estimate $\mathcal{E}^{h;p,q}_{u(-1,0)}(d)$ (denoted by BC Error and BC Estimator respectively in the Figures) for $R = 1.5$ and $R = 2.5$ respectively using $p = 3$ and $q = 1, 3, ..., 11$. To obtain the estimated error, we use the extended domain computed solution $u^{R+d,BT2}_{h;p,q}$ where $d/R = 1$, $p = 3$, and $q = 13$ and 9 for $R = 1.5$ and 2.5 respectively. As a reference we also plotted the q-convergence of the error $e^{h;p,q}_{u(-1,0)}$ computed using the Robin boundary condition (5.1)

Table 5.2. Comparison of $\theta^{\mathrm{EX}}_{u(-1,0)}$ (first and fourth lines), $\theta^{h;p,q}_{u(-1,0)}$ (second and fifth lines), and the $(h;p,q)$ parameters used in the computation of $u^{R+d,BT2}_{h;p,q}$ (third and sixth lines) for $R = 1.5, 2.5$ and $d/R = 1, 1.25$. For $u^{R+d,BT2}_{h;p,q}$ we employed $p = 3$, $q = 13$, and $h = 0.3125$ and 0.375 for $R = 1.5$ and 2.5. All GFEM computation uses plane-wave handbook functions.

		$R = 1.5$			$R = 2.5$		
		SOM	BT1	BT2	SOM	BT1	BT2
$\dfrac{d}{R} = 1.00$	$\theta^{\mathrm{EX}}_{u(-1,0)}$	1.01018	1.00506	1.04581	0.99971	0.99348	0.96981
	$\theta^{h;p,q}_{u(-1,0)}$	1.00357	1.00934	1.16091	1.01345	1.00628	0.92590
	$(h;p,q)$	$(h = 0.4375;\ p = 3,\ q = 13)$			$(h = 0.34375;\ p = 3,\ q = 9)$		
$\dfrac{d}{R} = 1.25$	$\theta^{\mathrm{EX}}_{u(-1,0)}$	0.99910	1.00305	1.06435	1.00207	0.99506	0.94266
	$\theta^{h;p,q}_{u(-1,0)}$	0.99290	1.00880	1.21631	0.87082	1.15106	3.46019
	$(h;p,q)$	$(h = 0.4375;\ p = 3,\ q = 13)$			$(h = 0.40625;\ p = 3,\ q = 9)$		

with g_2 obtained from u^{∞}_{EX}. From Figure 5.7 we can see that the exponential convergence of the GFEM, which is visible in the curve labeled Robin, is not achieved when SOM, BT1, or BT2 is employed. This is because the error coming from the truncation boundary condition dominates asymptotically. We also see that the BT2 gives the smallest error among the three artificial truncation boundary conditions employed. By using a larger truncation radius, as shown in Figure 5.8, the error due to the BT2 boundary condition becomes negligible and we can obtain the exponential convergence of the error for the entire range of q employed. From both Figures we can observe that the error and its estimator are very close and this can be confirmed from Table 5.3 which reports the effectivity index $\theta^{h;p,q} = \mathcal{E}^{h;p,q}_{u(-1,0)}(d)/e^{h;p,q}_{u(-1,0)}$ for $R = 1.5$ and 2.5.

5.2   Application to multiple scattering problem

Let us show that the above estimator $\mathcal{E}^{h;p,q}_{\mathcal{F}}(d)$ for the error $e^{h;p,q}_{\mathcal{F}}$ in the artificial boundary condition is also effective when used in more complex model problems. Let us first address the problem of three circular scatterers for which we have available u^{∞}_{EX} by employing the collocation method discussed earlier and hence we can also set up the computations using

Figure 5.7. q-convergence of the relative error in the quantity of interest $e_{u(-1,0)}^{h;p,q}$ and its estimator $\mathcal{E}_{u(-1,0)}^{h;p,q}(d)$ computed using $d/R = 1$, with the truncation radius $R = 1.5$. The difference between the curve for the Robin and the curves for the SOM, BT1, BT2 boundary conditions is the error due to the artificial boundary condition.

Table 5.3. Table of the effectivity index $\theta^{h;p,q} = \mathcal{E}_{u(-1,0)}^{h;p,q}(d)/e_{u(-1,0)}^{h;p,q}$ for $R = 1.5$ and $R = 2.5$ for $q = 1, ..., 11$.

q	$R = 1.5$			$R = 2.5$		
	SOM	BT1	BT2	SOM	BT1	BT2
1	0.9993	1.0464	0.9994	0.9999	0.9999	0.9999
3	0.9883	1.0178	0.9831	0.9999	0.9999	0.9999
5	0.9978	1.0099	0.9487	1.0005	1.0005	1.0003
7	1.0034	1.0093	1.1779	1.0069	1.0417	1.0032
9	1.0036	1.0093	1.1568	1.0122	1.0100	1.2059
11	1.0036	1.0093	1.1619	1.0133	1.0388	1.1042

the Robin boundary condition (5.1).

Figures 5.10-5.12 show the convergence of the relative errors $\mathcal{F}(u)$ at the points A, B, and C shown in Figure 5.9 for the Sommerfeld, Bayliss-Turkel 1, Bayliss-Turkel 2, and Robin boundary conditions, where $\mathcal{F}(u) = u(A), u(B),$ and $u(C)$ respectively. We can see that on
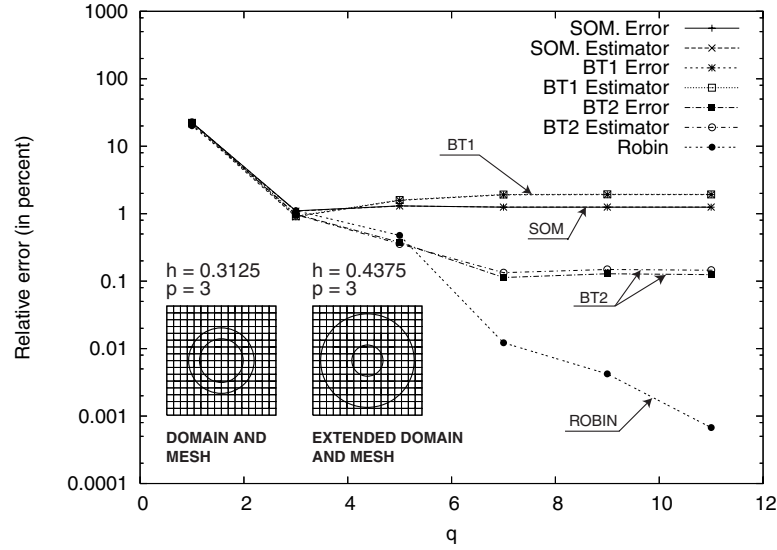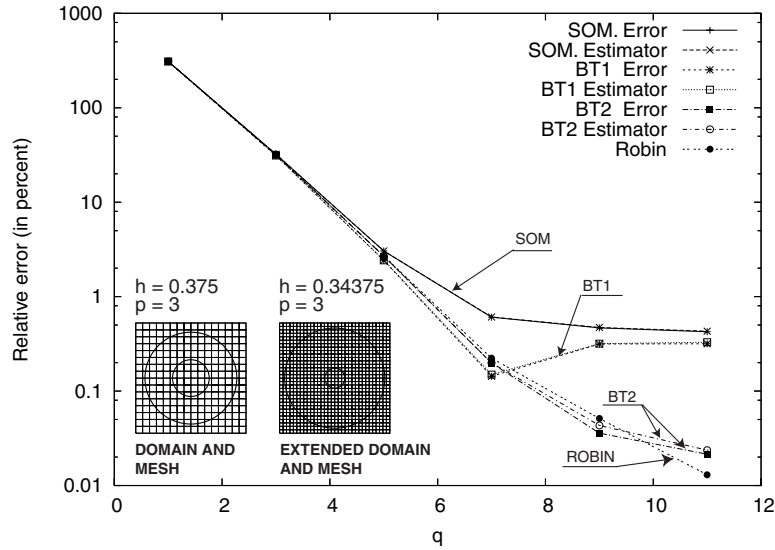
Figure 5.8. q-convergence of the relative error in the quantity of interest $e^{h;p,q}_{u(-1,0)}$ and its estimator $\mathcal{E}^{h;p,q}_{u(-1,0)}(d)$ computed using $d/R = 1$ with the truncation radius $R = 2.5$. Note that here, the GFEM using BT2 gives practically the same results as the ones obtained using the Robin boundary condition.
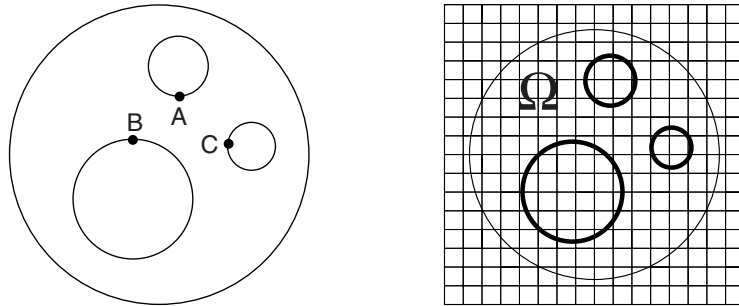
Figure 5.9. Location of output points, the domain Ω with truncation radius $R = 2.5$ and the employed mesh.

point A (Figure 5.10), error due to the Bayliss-Turkel 2 boundary condition is negligible up to $q = 13$ which is sufficient to compute $u(A)$ with relative error 0.4 %. For $q \geq 15$ the error due to the BT2 condition stops the exponential convergence however this does not matter because high accuracy has already been achieved. This is not the case with SOM and BT1 boundary conditions which completely destroy the exponential convergence and

Figure 5.10. q-convergence of $e_{u(A)}^{h;p,q}$ using Sommerfeld, Bayliss-Turkel 1, Bayliss-Turkel 2 and Robin boundary conditions. Note that the results for Bayliss-Turkel 2 and the Robin condition practically coincide for q up to 13.

high accuracy of the GFEM.
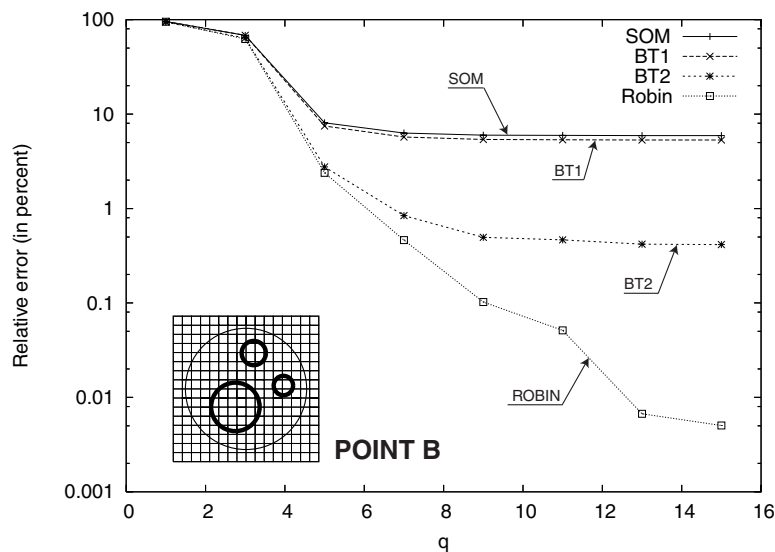
Figure 5.11. q-convergence of $e_{u(B)}^{h;p,q}$ using Sommerfeld, Bayliss-Turkel 1, Bayliss-Turkel 2 and Robin boundary conditions. The error coming from the truncation boundary condition dominates the solution.

From Figure 5.11 we can see that for point B the error due to the artificial boundary condition is the dominant part of the error for all three boundary conditions employed and that by using BT2 we can reach 0.4 % accuracy before it stops converging.

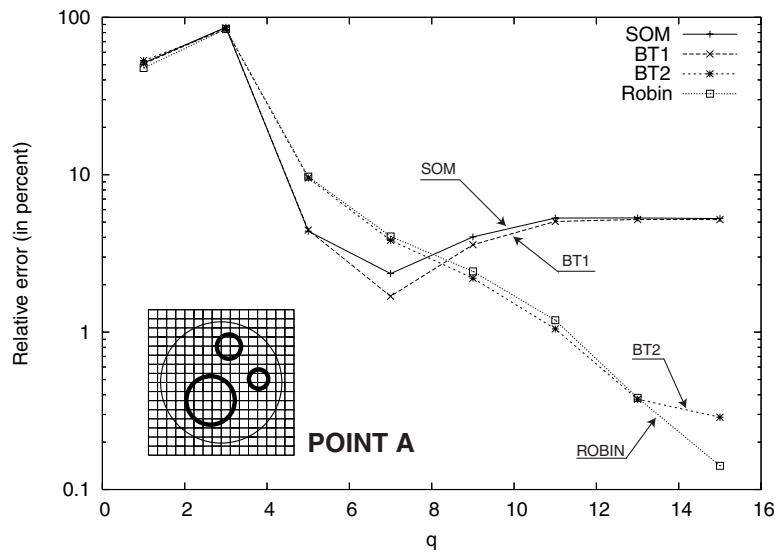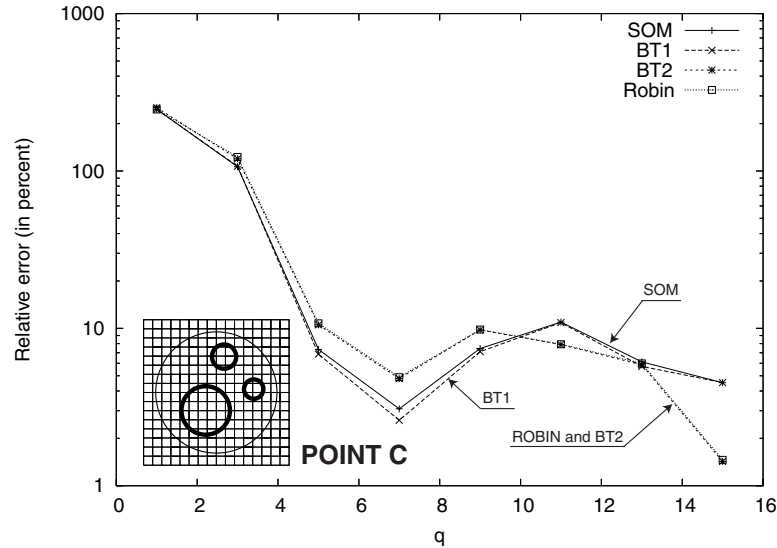Figure 5.12. q-convergence of $e_{u(C)}^{h;p,q}$ using Sommerfeld, Bayliss-Turkel 1, Bayliss-Turkel 2 and Robin boundary conditions. Here we can see that the q-convergence has not reached its asymptotic range, and the error curves for BT2 and Robin practically coincide.

From Figure 5.12 we conclude that on point C the asymptotic range of GFEM has not been reached and the error from the GFEM approximation in Ω dominates. This explain why the error obtained using all four boundary conditions, SOM, BT1, BT2 and Robin are rather close. The results for BT2 coincide with those for Robin and only 1.5 % is achieved for $q = 15$.

Figures 5.13, 5.14, and 5.15 compare the q-convergence graphs for the errors $e_{u(x)}^{h;p,q}$ and its estimate $\mathcal{E}_{u(x)}^{h;p,q}(d)$ for $R = 1.5$ respectively for $x = A, B, C$ using $p = 3$ and $q = 1, 3, ..., 15$. To obtain the estimated error, we use $u_{h;p,q}^{R+d,BT2}$ where $d/R = 1$, $p = 3$, and $q = 9$. Again we can see that the estimator follows closely the error with the exception of the case where

$\mathcal{F} = u(A)$ using Bayliss-Turkel 2. Here the estimator diverges asymptotically from the error; most likely because the estimated error is rather small. These results are confirmed in Table 5.4 which reports the effectivity index $\theta_{\mathcal{F}}^{h;p,q}$ for the points A, B, and C using SOM, BT1 and BT2.

Figure 5.13. q-convergence of the error $e_{u(A)}^{h;p,q}$ and its estimator $\mathcal{E}_{u(A)}^{h;p,q}(d)$ computed using $d/R = 1$, with the truncation radius $R = 2.5$.

Table 5.4. Table of the effectivity index $\theta^{h;p,q}$ on points A, B, and C.

q	A			B			C		
	SOM	BT1	BT2	SOM	BT1	BT2	SOM	BT1	BT2
1	0.9854	0.9852	0.9874	0.9998	0.9997	0.9997	0.9779	0.9779	0.9780
3	0.9808	0.9825	0.9831	1.0003	1.0003	1.0003	0.9905	0.9904	0.9876
5	0.8836	0.9427	0.9487	1.0075	1.0078	1.0226	1.0581	1.0886	1.1043
7	0.8510	1.1448	0.7648	1.0088	1.0090	1.0401	0.7609	0.8862	1.1699
9	0.9960	1.0855	0.4207	1.0097	1.0101	1.1087	1.0945	1.1249	1.1096
11	1.0503	1.0991	0.7722	1.0097	1.0100	1.0976	0.6939	0.7027	0.5563
13	1.0927	1.1359	4.0522	1.0100	1.0104	1.1568	0.4318	0.3830	0.7318
15	1.1067	1.1483	5.9860	1.0100	1.0105	1.1560	0.6149	1.4423	1.6660

Figure 5.14. q-convergence of the error $e_{u(B)}^{h;p,q}$ and its estimator $\mathcal{E}_{u(B)}^{h;p,q}(d)$ computed using $d/R = 1$, with the truncation radius $R = 2.5$.
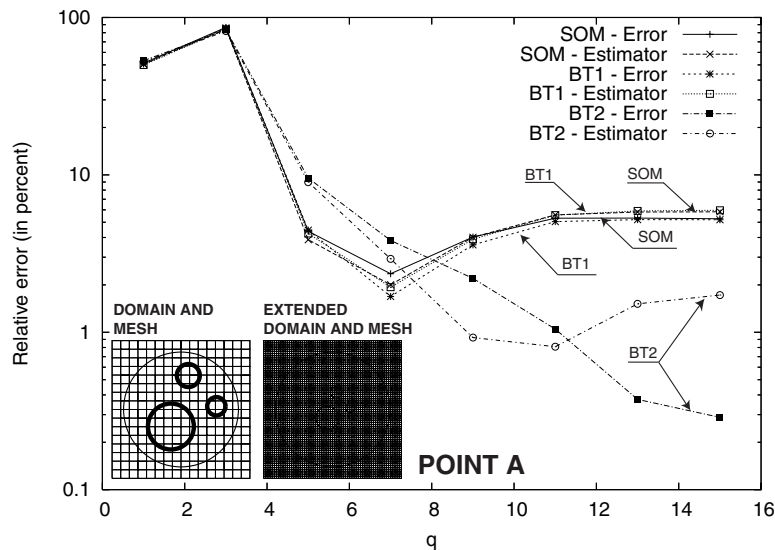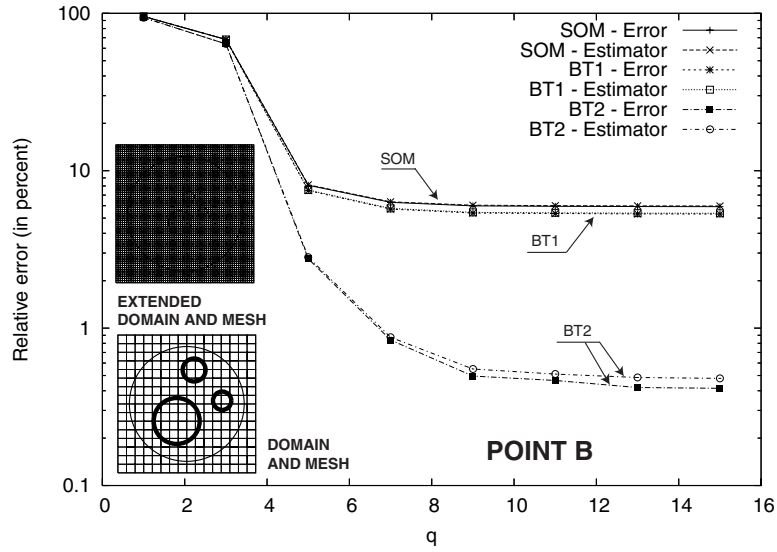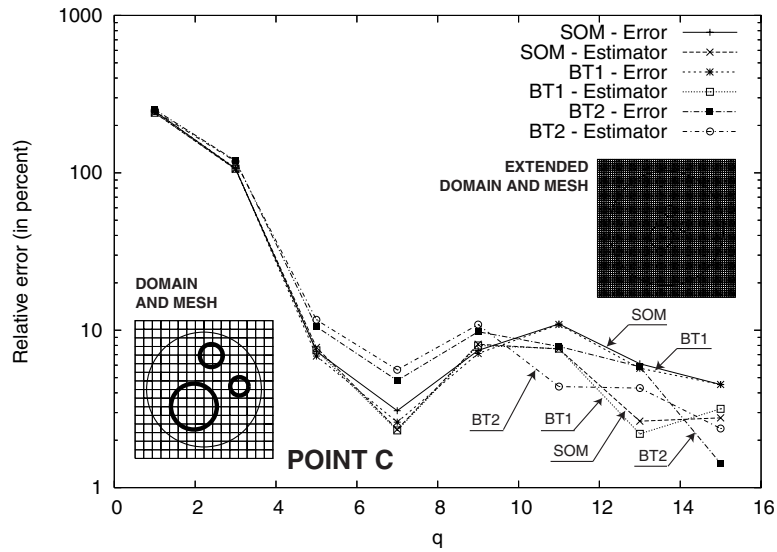

Figure 5.15. q-convergence of the error $e_{u(C)}^{h;p,q}$ and its estimator $\mathcal{E}_{u(C)}^{h;p,q}(d)$ computed using $d/R = 1$, with the truncation radius $R = 2.5$.

Finally, let us illustrate the analogous computations for Model Problem III which is obtained from Model Problem II by replacing the circular scatterers by squares. Although

we do not have a proof of exponential convergence in this case we conjectured that for a high k, e.g. $k = 20$ employed here the reentrant corners do not influence the convergence and we expect similar results as in the case of circular scatterers.

Figure 5.16 gives an example of the solution computed using $p = 3$ and $q = 9$ on the domain and mesh shown in Figure 5.17.

REAL PART OF SCATTERED WAVE

Min = -.193E+01 ; Max = 0.196E+01

-0.75 -0.50 -0.25 0.00 0.25 0.50 0.75

IMAGINARY PART OF SCATTERED WAVE

Min = -.196E+01 ; Max = 0.216E+01

-0.75 -0.50 -0.25 0.00 0.25 0.50 0.75
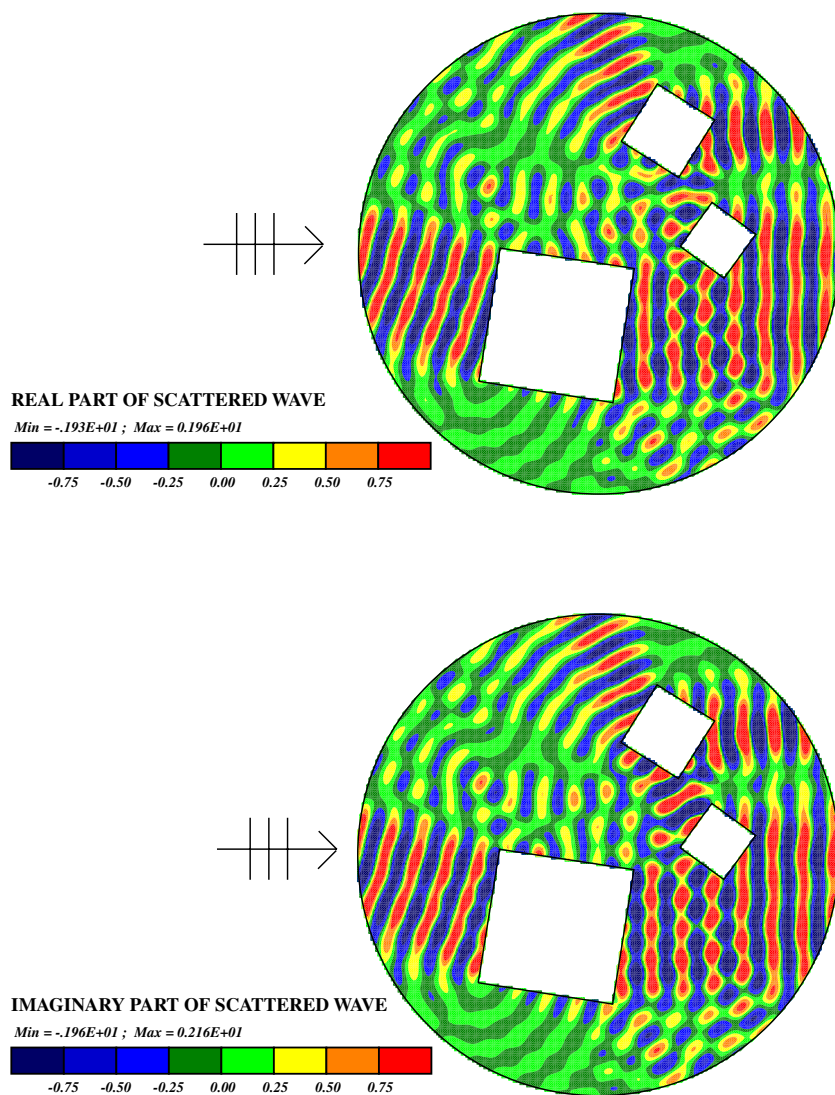
Figure 5.16. Contours of the real and imaginary parts of the scattered field of Model Problem III for $k = 20$, computed using the domain and mesh pictured in 5.17 with $p = 3$ and $q = 9$.

In this case we are lacking an exact solution and we show only the convergence of the
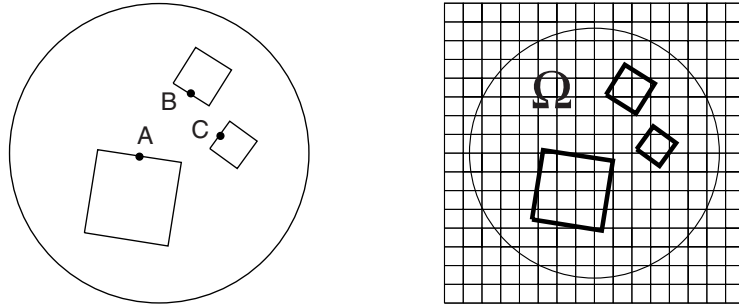
Figure 5.17. Location of output points,the domain Ω with truncation radius $R = 2.5$ and the employed mesh.

estimated error $\mathcal{E}_{u(x)}^{h;p,q}(d)$ for $x = A, B, C$ in Figures 5.18, 5.19, and 5.20. Our estimator predicts that using the GFEM with BT2, acceptable accuracy is reached for all points.
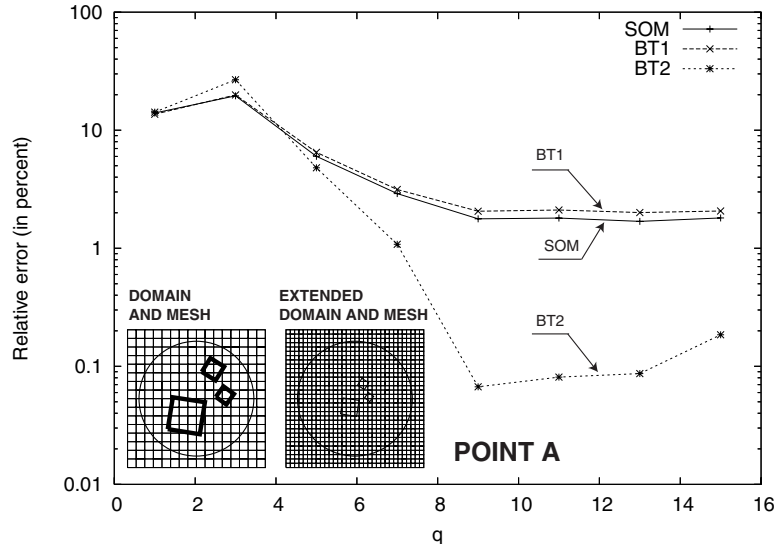
Figure 5.18. q-convergence of the estimator $\mathcal{E}_{u(A)}^{h;p,q}(d)$ computed using $d/R = 1$, with the truncation radius $R = 2.5$.

Figures 5.21 plots the contours of the real part of approximate solution computed using $h = 0.375$, $q = 9$ and $p = 3$ with truncation radius $R = 2.5$ for Sommerfeld, Bayliss-Turkel 1, and Bayliss-Turkel 2 boundary conditions along with the real part of approximate solution computed using $h = 0.34375$, $q = 9$ and $p = 3$ with truncation radius $R = 5.0$ and
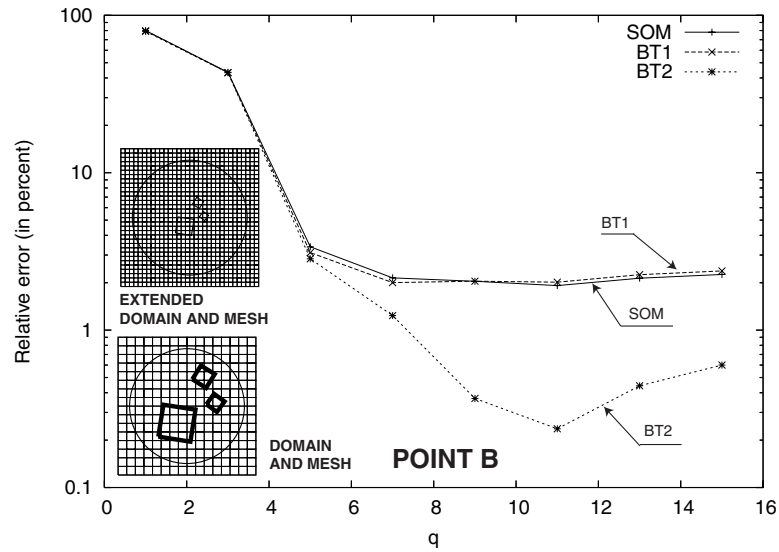
Figure 5.19. q-convergence of the estimator $\mathcal{E}^{h;p,q}_{u(B)}(d)$ computed using $d/R = 1$, with the truncation radius $R = 2.5$.
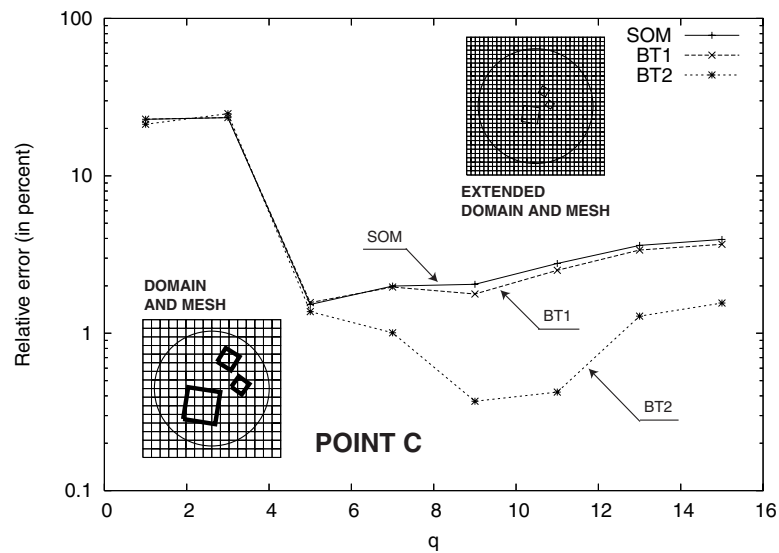
Figure 5.20. q-convergence of the estimator $\mathcal{E}^{h;p,q}_{u(C)}(d)$ computed using $d/R = 1$, with the truncation radius $R = 2.5$.

Bayliss-Turkel 2 boundary condition. We can observe that the contours of Bayliss-Turkel 2 with $R = 2.5$ and $R = 5.0$ are identical and while the contours of Sommerfeld and Bayliss-

Turkel 1 are identical to each other, their difference with the Bayliss-Turkel 2 contours can be seen. Based on this observation we can conclude using BT2 with truncation radius $R = 2.5$ is sufficient to ensure that the error from truncation boundary condition does not dominate.
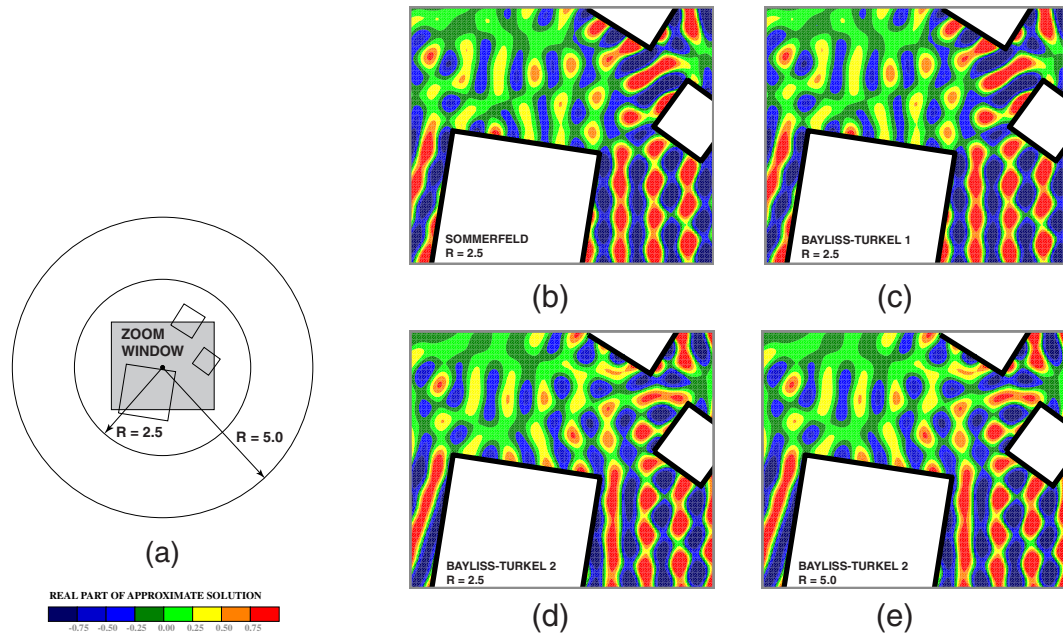
Figure 5.21. (a) The zoom window; Contour plots of the real part of approximate solution computed using $h = 0.375$, $q = 9$ and $p = 3$ with truncation radius $R = 2.5$ for (b) Sommerfeld, (c) Bayliss-Turkel 1, (d) Bayliss-Turkel 2 boundary conditions; and (e) the real part of approximate solution computed using $h = 0.34375$, $q = 9$ and $p = 3$ with truncation radius $R = 5.0$ and Bayliss-Turkel 2 boundary condition.

CHAPTER VI

CONCLUSION AND OPEN PROBLEMS

We can summarize the conclusions, which are based on theoretical understanding and on computations complementing what is possible to say by the theory, as follows:

1. The pollution effect for the Helmholtz equation cannot be avoided. It is increasing with k and decreasing with increasing p and q. We can, however, detect the pollution by using an a posteriori error estimation.

2. We have exponential rate of convergence with respect to wave directions. This is predicted by the theory and holds in a large range of practical accuracy, as it can be seen from our numerical experiments.

3. The numerical integrations influence the accuracy of the solution. Integration error can be detected by a posteriori estimation.

4. Round-off error must be analyzed together with the numerical integration error because both errors have similar character. To analyze the influence of round-off error only by the condition number is not correct.

5. The various interior handbook functions give an almost identical performance in solving the Helmholtz equation. The selection of the local bases is thus determined by other factors such as the ease of the implementation or the computational cost.

6. Currently the handbook function with the simplest implementation is the plane-wave handbook functions; the wave-band handbook functions require the integration on θ-direction which can be very expensive, while the Vekua functions require the computa-

tion of Bessel function which is more costly than the computation of the trigonometric function.

7. The error from the truncation absorbing boundary condition is coupled with the error from interior approximation. By introducing an additional computation using an extended domain we can get a reliable estimator of the error due to the artificial boundary condition.

We would also like to mention some of the open problems:

1. Characterization of the pollution effect. The theory that we have is valid only for sufficiently small h.

2. Theoretical analysis of the influence of the integration error is not available, as well as determination of largest tolerance in the adaptive integration leading to the goal of the analysis.

3. The round-off analysis, along with theory and practice of the construction of the shape function which lead to the good conditioning number, and possibly for preconditioning and effective iterative solver are open.

4. Investigation of various partition of unity function. For this work we are using a standard hat-function as our partition of unity function. We can for example use smoother functions as proposed by Oden, Duarte, and Zienkiewicz [57].

5. Analysis of optimal combinations between interior handbook functions and the functions from boundary.

6. Formulation and implementation of infinite elements on the truncation boundary which can be attractive due to the capability of using p-adaptivity. Here we would

like to mention the work of Safjan and Newman which proposes the use of infinite element using basis function with local support to obtain artificial truncation boundary conditions with very small error [58, 59].

REFERENCES

[1] F. Ihlenburg, Finite Element Analysis of Acoustic Scattering, Springer, New York, 1998.

[2] I. Babuška, F. Ihlenburg, T. Strouboulis and S.K. Gangaraj, A posteriori error estimation for finite element solutions of Helmholtz' equation. Part I: The quality of local indicators and estimators, Int. J. Numer. Meth. Engrg. 40 (1997) 3443–3462.

[3] I. Babuška, F. Ihlenburg, T. Strouboulis and S.K. Gangaraj, A posteriori error estimation for finite element solutions of Helmholtz' equation. Part II: Estimation of the pollution error, Int. J. Numer. Meth. Engrg. 40 (1997) 3883–3900.

[4] A. Deraemaeker, I. Babuška and P. Bouillard, Dispersion and pollution of the FEM solution for the Helmholtz equation in one, two and three dimensions, Int. J. Numer. Meth. Engrg. 46 (4) (1999) 471–499.

[5] I. Babuška and S. Sauter, Is the pollution effect of the FEM avoidable for the Helmholtz equation considering high wave numbers ? SIAM J. Numer. Anal. 34 (6) (1997) 2392–2423.

[6] A. Bayliss and E. Turkel, Radiation boundary conditions for wave-like equations, Comm. Pure Appl. Math. 33 (1980) 707–725.

[7] A. Bayliss, M. Gunzburger, and E. Turkel, Boundary conditions for the numerical solution of elliptic equations in exterior domains, SIAM J. Appl. Math. 42 (1982) 430–451.

[8] J.B. Keller and D. Givoli, Exact non-reflecting boundary conditions, J. Comput. Phys. 82 (1989) 172–192.

[9] M.J. Grote and J.B. Keller, On nonreflecting boundary conditions, J. Comput. Phys. 122 (1995) 231–243.

[10] D. Burnett, A 3-D acoustic infinite element based on generalized multipole expansion, J. Acoust. Soc. Am. 96 (1994) 2798–2816.

[11] R.J. Astley, Infinite elements for wave problems: A review of current formulations and an assessment of accuracy, IJNME 49 (2000) 951–976.

[12] K. Gerdes, Conjugated versus the unconjugated infinite element method for the Helmholtz equation in exterior domains, CMAME 152 (1998) 125–145.

[13] J.P. Berenger, A perfectly matched layer for the absorption of electromagnetic waves, J. Comput. Phys. 136 (1997) 68–82.

[14] I. Babuška, G. Caloz and J.E. Osborn, Special finite element methods for a class of second order elliptic problems with rough coefficients, SIAM J. Numer. Anal. 31 (4) (1994) 945–981.

[15] J. M. Melenk, Finite element methods with harmonic shape functions for solving Laplace's equation, M.S. thesis, University of Maryland, College Park, MD, 1992.

[16] J. M. Melenk, On generalized finite element methods, Ph.D. dissertation, University of Maryland, College Park, MD, 1995.

[17] I. Babuška and J. M. Melenk, The partition of unity finite element method: Basic theory and applications, Comput. Methods Appl. Mech. Engrg. 139 (1996) 289–314.

[18] I. Babuška and J. M. Melenk, The partition of unity method, Int. J. Numer. Meth. Engrg. 40 (1997) 727–758.

[19] J.M. Melenk and I. Babuška, Approximation with harmonic and generalized harmonic polynomials in the partition of unity method, Comput. Assist. Mech. Engrg. Sci. 4 (1997) 607–632.

[20] O. Laghrouche and P. Bettess, Solving short wave problems using special finite elements - towards an adaptive approach, in: J. Whiteman (Ed.), The Mathematics of Finite Elements and Applications X, Elsevier, New York, 1999, pp. 181–194.

[21] O. Laghrouche, P. Bettess, E. Perrey-Debain and J. Trevelyan, Wave interpolation finite elements for Helmholtz problems with jumps in the wave speed, Comput. Methods Appl. Mech. Engrg. 194 (2005) 367–381.

[22] P. Bettess, J. Shirron, O. Laghrouche, B. Peseux, R. Sugimoto, and J. Trevelyan, A numerical integration scheme for special finite elements for the Helmholtz equation, Int. J. Numer. Meth. Engrg. 56 (2003) 531–552.

[23] C. Farhat, I. Harari, and L.P. Franca, The discontinuous enrichment method, Comput. Methods Appl. Mech. Engrg. 190 (2001) 6455–6479.

[24] C. Farhat, I. Harari, and U. Hetmaniuk, A discontinuous Galerkin method with Lagrange multipliers for the solution of Helmholtz problems in the mid-frequency regime, Comput. Methods Appl. Mech. Engrg. 192 (2003) 1389–1419.

[25] P. Rouch and P. Ladevèze, The variational theory of complex rays: A predictive tool for medium-frequency vibrations, Comput. Methods Appl. Mech. Engrg. 192 (2003) 3301–3315.

[26] H. Riou, P. Ladevèze, and P. Rouch, Extension of the variational theory of complex rays to shells for medium-freqency vibrations, J. Sound Vib. 272 (2004) 341–360.

[27] H. Riou, Sur le calcul des vibrations moyennes et hautes fréquences par la théorie variationnelle des rayon complexes, Ph.D. dissertation, ENS de Cachan, 2004.

[28] A. Duarte, The *hp* cloud method, Ph.D. dissertation, University of Texas at Austin, Austin, TX, 1996.

[29] C.A. Duarte and J.T. Oden, An *hp* adaptive method using clouds, Comput. Methods Appl. Mech. Engrg. 139 (1996) 237–262.

[30] I. Babuška, T. Strouboulis and K. Copps, The design and analysis of the generalized finite element method, Comput. Methods Appl. Mech. Engrg. 181 (1) (2000) 43–69.

[31] T. Strouboulis, I. Babuška and K. Copps, The generalized finite element method: An example of its implementation and illustration of its performance, Int. J. Numer. Meth. Engrg. 47 (2000) 1401–1417.

[32] K. Copps, The design and implementation of the generalized finite element method, Ph.D. dissertation, Texas A&M University, College Station, TX, 2000.

[33] T. Strouboulis, K. Copps and I. Babuška, The generalized finite element method, Comput. Methods Appl. Mech. Engrg. 190 (2001) 4081–4193.

[34] L. Zhang, Generalized finite element method for multiscale analysis, Ph.D. dissertation, Texas A&M University, College Station, TX, 2003.

[35] T. Strouboulis, L. Zhang and I. Babuška, Generalized finite element method using mesh-based handbooks: Application to problem in domains with many voids, Comput. Methods Appl. Mech. Engrg. 192 (2003) 3109–3161.

[36] T. Strouboulis, L. Zhang and I. Babuška, *p*-version of the Generalized FEM using mesh-based handbooks with applications to multiscale problems, Int. J. Numer. Meth. Engrg. 60 (2004) 1639–1672.

[37] I. Babuška, U. Banerjee and J.E. Osborn, On principles for the selection of shape functions for the generalized finite element method, Comput. Methods Appl. Mech. Engrg. 191 (2002) 5595–5629.

[38] I. Babuška, U. Banerjee and J.E. Osborn, Survey of meshless and generalized finite element methods: A unified approach, Acta Numerica 12 (2003) 1–125.

[39] I. Babuška, U. Banerjee and J.E. Osborn, Generalized finite element methods – Main ideas, results and perspective, International Journal of Computational Methods 1 (1) (2004) 67–103.

[40] J. Dolbow, N. Moës and T. Belytschko, Discontinuous enrichment in finite elements with a partition of unity method, Finite Elements in Analysis and Design 36 (2000) 235–260.

[41] N. Sukumar, D.L. Chopp, N. Moës, and T. Belytschko, Modeling holes and inclusions by level sets in the extended finite-element method, Comput. Methods Appl. Mech. Engrg. 190 (2001) 6183–6200.

[42] C.A. Duarte, I. Babuška, and J.T. Oden, Generalized finite element methods for three-dimensional structural mechanics problems, Computers & Structures 177 (2000) 215–232.

[43] P. Ortiz, Finite elements using a plane-wave basis for scattering of surface water waves, Phil. Trans. R. Soc. Lond. A 362 (2004) 525–540.

[44] R.J. Astley and P. Gamallo, Special short wave elements for flow acoustics, Comput. Methods Appl. Mech. Engrg. 194 (2005) 341–353.

[45] E. Perrey-Debain, O. Laghrouche, P. Bettess, and J. Trevelyan, Plane-wave basis finite elements and boundary elements for three-dimensional wave scattering, Phil. Trans. R. Soc. Lond. A 362 (2004) 561–577.

[46] R. Sugimoto, P. Bettess, and J. Trevelyan, A numerical integration scheme for special quadilateral finite elements for the Helmholtz equation, Commun. Numer. Meth. Engng. 19 (2003) 233–245.

[47] P. Ladevèze and H. Riou, Calculation of medium-frequency vibrations over a wide frequency range, Comput. Methods Appl. Mech. Engrg. 194 (2005) 3167–3191.

[48] C.A. Duarte and J.T. Oden, An *hp* adaptive method using clouds, Comput. Methods Appl. Mech. Engrg. 139 (1996) 237–262.

[49] B. A. Szabó and I. Babuška, Finite Element Analysis, John Wiley & Sons, Inc., New York, 1991.

[50] F. Ihlenburg and I. Babuška, Finite element solution to the Helmholtz equation with high wave number - part II: The *hp*-version of the FEM, SIAM J. Numer. Anal. 34 (1) (1997) 315–358.

[51] F. Ihlenburg and I. Babuška, Dispersion analysis and error estimation of Galerkin finite element methods for the Helmholtz equation, Int. J. Numer. Meth. Engrg. 38 (1995) 3745–3774.

[52] D. S. Jones, Acoustic and Electromagnetic Waves, Oxford University Press, New York, 1986.

[53] O. Laghrouche, P. Bettess, and R.J. Astley, Modelling of short wave diffraction problems using approximating systems of plane waves, Int. J. Numer. Meth. Engrg. 54 (2002) 1501–1533.

[54] P. J. Davis and P. Rabinowitz, Methods of Numerical Integration, Academic Press, Inc., San Diego, 1984.

[55] T. Strouboulis, L. Zhang, D. Wang and I. Babuška, A posteriori error estimation for generalized finite element methods, Comput. Methods Appl. Mech. Engrg. 195 (2006) 852–879.

[56] S. Biwa, S. Yamamoto, F. Kobayashi and N. Ohno, Computational multiple scattering analysis for shear wave propagation in unidirectional composites, Inter. Journal of Solids and Structures 41 (2004) 435–458.

[57] J. T. Oden, C. A. Duarte, and O. C. Zienkiewicz, A new cloud-based hp finite element method, Comput. Methods Appl. Mech. Engrg. 153 (1998) 117–126.

[58] A. Safjan and M. Newman, On two-dimensional infinite elements utilizing basis functions with compact support, Comput. Methods Appl. Mech. Engrg. 190 (2001) 6399–6424.

[59] A. Safjan and M. Newman, Three-dimensional infinite elements utilizing basis functions with compact support, Comput. Math. Appl. 43 (2002) 981–1002.

VITA

Realino Hidajat was born in 1974 in Jakarta, Indonesia. After graduating from Parahyangan Catholic University in Bandung, Jawa Barat in 1997 with a B.S. degree in civil engineering he joined a professional structural design firm as a structural engineer. In 1999 he went to the University of Nebraska - Lincoln and obtained his M.S. degree in engineering mechanics in 2001 under the supervision of Dr. Andrzej Safjan. Afterwards he enrolled in the Department of Aerospace Engineering, Texas A&M University and received his Ph.D. in Aerospace Engineering in 2007 under the guidance of Dr. Theofanis Strouboulis. His permanent address is Jalan Kebon Raya VII/34. Jakarta 11510. Indonesia.